



Deutsches Zentrum
für Luft- und Raumfahrt
German Aerospace Center

Technical University of Munich
School of Engineering and Design
Chair for Astronomic and Physical Geodesy
Univ.-Prof.Dr.techn Mag.rer.nat Roland Pail

German Aerospace Center

Development and Test of a Automatic Gain Controller for a Lidar-Detector Based on Airborne Measurements of Cirrus Clouds

Paul Figueroa Cotorogea

Thesis submitted
within the Master's Program
ESPACE - Earth Oriented Space Science and Technology

Supervisor: Dr. Patrick Vrancken
German Aerospace Center
Examiner: Dr. Christoph Kiemle
German Aerospace Center
Technical University Munich

March 22, 2024

Erklärung zur Bachelorarbeit/Masterarbeit

Hiermit versichere ich, dass die vorliegende Arbeit von mir selbstständig verfasst wurde und dass keine anderen als die angegebenen Quellen und Hilfsmittel benutzt wurden.

Diese Erklärung erstreckt sich auch auf in der Arbeit enthaltene Graphiken, Zeichnungen, Kartenskizzen und bildliche Darstellungen.

Bachelor's/Master's thesis statement of originality

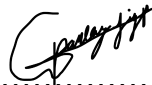
I hereby confirm that I have written the accompanying thesis by myself, without contributions from any sources other than those cited in the text and acknowledgements.

This applies also to all graphics, drawings, maps and images included in the thesis.

München, 15.12.2023

Ort und Datum

Place and date



Unterschrift

Signature

ABSTRACT

In commercial aviation, clear-air turbulence (CAT) represents a major risk of damage to the aircraft or injury to the passengers. Gust load alleviation (GLA) is one strategy to mitigate loads caused by CAT and has been under development for decades. More recent techniques involve the use of Doppler Wind Lidar (DWL) to measure wind fields ahead of the plane and provide information for a feed forward GLA controller. This thesis deals with the receiver subsystem of such a DWL, developed by the German Aerospace Center (Deutsches Zentrum für Luft- und Raumfahrt, DLR). During cruise flight, the measurement range may be occasionally contaminated by cirrus clouds, which due to stronger back-scatter will lead to over-saturation of the detector. The goal of this work is to design, implement and test an automatic gain controller (AGC) for the lidar detector that will keep the return signal level within a specified range around a setpoint, regardless of varying external conditions. In order to set up a representative validation experiment, a study of back-scattering dynamics using data from airborne lidar observations, and theoretical information is performed. This study yields characteristic variations both in magnitude and frequency of back-scattering on cirrus clouds. The AGC is based on a proportional-integrating (PI) controller architecture and is able to keep the detector output within 10 % of a specified setpoint at ~ 150 % input signal variability.

List of Figures

1.1	Typical altitudes at which different cloud types occur.	4
1.2	Workflow of the design approach of the automatic gain controller.	6
2.1	Directionality of scattering processes (Castellani et al. 2014).	8
2.2	The scattering regimes for a given wavelength and particle size (Caballero 2014)	8
2.3	Simplified synopsis of a co-axial lidar system.	10
2.4	Origin of overlap function. Laser light captured by receiver optics at three different ranges.	12
2.5	Concept of a lidar-based feed-forward gust alleviation system.	13
2.6	Solid line: combined molecular and aerosol back-scattering spectrum. Dashed line: combined spectrum Doppler shifted by Δf	14
2.7	Top: sinusoidal signals y_1 and y_2 with slightly different frequencies. Bottom: resulting beat from superposition of y_1 and y_2	15
2.8	Combined Rayleigh and Mie spectrum for different altitudes (Tenti S6 model, Herbst 2019). The spectra have large differences in their magnitude depending on the altitude and have been normalized here.	16
2.9	Schematics of the AEROLI direct-detection Doppler wind lidar, based on a field-widened fringe-imaging Michelson interferometer (<i>FWFIMI</i>). <i>Tel</i> : telescope, <i>L</i> : lens, <i>L_{cyl}</i> : cylindrical lens, <i>IF</i> : interference filter, <i>FC</i> : fiber coupler, <i>OF</i> : optical fiber, <i>PBSC</i> : polarizing beam splitter cube, <i>PMT_{1,2}</i> : photomultiplier, <i>W</i> : window (Vrancken and Herbst 2022).	17
2.11	Combined reference and attenuated backscatter signal from ground measurements (Linsmayer 2023).	18
2.13	Construction of a photomultiplier tube (Hamamatsu-Optics 2017)	21
2.14	Reduced representation of a transimpedance amplifier.	23
2.15	General feedback control problem.	24
2.16	Mass-damper-spring model.	25
2.17	Unit-step response of a first-order (PT1) and second-order system (PT2).	26
2.18	Block diagram of a PID controller.	26
2.20	Tracks flown during the Cirrus-HL campaign (DLR 2023b).	30
2.21	Scheme of collocation of DLR-HALO with AWI-Polar 5 and Polar 6 aircraft, as planned for HALO-AC3 (Leipzig 2023)	31
2.22	Tracks flown during the HALO-AC3 campaign (DLR 2023c)	32
3.1	Dashed line: overlap function of the AEROLI receiver, dotted line: $1/r^2$ factor, solid line: product of the overlap function and the $1/r^2$	34

List of Figures

3.2	Synthetic lidar signals from clear sky and cirrus return, computed with Equation 2.2	35
3.3	Data from the Cirrus-HL flight #18. Top: altitude-distance plot of the HSRL backscattering ratio in logarithmic scale. The red square marks the scene depicted in Figure 3.4. Bottom: flight track.	37
3.4	Selected scene from flight #18 of Cirrus-HL. Top: altitude-distance plot of the HSRL backscattering ratio in logarithmic scale. Bottom: horizontal profile of the HSRL backscatter ratio at 10 km altitude.	38
3.5	Distance travelled between successive location points ΔR along the flight trajectory sampled at 1 Hz. Exemplary data from flight #18 of the Cirrus-HL campaign.	40
3.6	Top: slice of backscattering ratio profile. Solid, black line: corresponding power spectrum averaged over all altitude levels. Dashed, red line: corresponding spectral slope.	41
3.7	Top: slice of backscattering ratio profile. Solid, black line: corresponding power spectrum averaged over all altitude levels. Dashed, red line: corresponding spectral slope.	42
3.8	Solid, black line: Power spectrum of the backscattering ratio averaged over all the measurement data. Dashed, red line: corresponding spectral slope.	42
3.9	Histogram of the scaling exponents from the individual data scenes.	43
3.10	Extraction of the peak return power $\hat{P}_{return}(trajectory)$ from synthetic attenuated backscatter signals $P_{return}(r)$ computed from observed values of α and β for three different windows (red, purple and green rectangles).	45
3.11	Histograms of $\Delta \hat{P}_{return}^n$ for $n = 1, 2, 3, 4, 5$. 3σ relates to $\Delta \hat{P}_{return}^{n=1}$	47
3.12	3σ of the peak return signal power variability vs Δr	47
4.1	Experimental set-up for characterization of the detector electronics and validation of AGC. $F_{1,2,3}$: neutral density filters, $BS_{1,2}$: polarizing beam splitters, BS_3 : non-polarizing beam splitter, $C_{1,2}$: fiber couplers, L_1 : collimating lens, L_2 : cylindrical lens.	49
4.2	2D voltage signal of a laser pulse's rising edge.	50
5.1	Reduced representation of the detector subsystem	51
5.2	32-channel linear photo-multiplier tube array (Hamamatsu H7260 Series) (Hamamatsu Optics 2023).	52
5.3	Rising edge of a laser pulse, measured with the set-up in Figure 4.1 and with the settings in Table 5.1. Solid line: average of ~ 1000 pulses. Grey area: noise envelope of the pulses.	53
5.4	Solid line: Non-linear curve-fitting of gain μ vs. supply voltage U_{HV} . Squares: data from the data sheet of the PMTA (H7260-200).	54

List of Figures

5.5	Illustration of the pre-processing steps for the response time analysis. Top left: first 10 s of the raw output voltage. The red box marks the zoom-in section shown in the top right plot. Top right: enlarged view of the raw data. The red stars indicate the median values of the individual pulse plateaus. Bottom left: down-sampled output data. Bottom right: mean value of all the periods from the down-sampled output data.	57
5.6	Rise times and settling times of the rising edges of the input steps listed in Table 5.2	58
5.7	Rise times and settling times of the falling edges of the input steps listed in Table 5.2	59
5.8	60
6.1	PID tuning procedure. The dotted lines are the output achieved by incrementing the proportional gain K_p until a sustained oscillation is achieved. The solid line represents the system output with the hypothetically optimal PID gains. . .	63
6.2	PI tuning procedure. The dotted lines are tuning attempts and the solid line represents the system output with the final gains.	63
6.3	Solid line: Filter transmission vs. filter position in degrees. Triangles: corresponding output signal level. Dashed line: linear fit of the transmission for angles between 100 and 150 degrees.	64
6.4	Upper plot: Measured laser intensity with the AGC disabled (dotted line), and with the AGC enabled (solid line). The grey area represents a tolerance margin of +/- 10 % of the setpoint of 0.3 V. Lower plot: Filter transmission (dotted line), and control voltage U_{gain} (solid line).	66
6.5	Analogous to Figure 6.4	67
6.6	Development of U_{gain} and U_{int} throughout <i>Test 2</i> . Dashed line: integrating component. Solid line: U_{gain}	68
7.1	Top: slice of backscattering ratio profile. Solid, black line: corresponding power spectrum averaged over all altitude levels. Dashed, red line: corresponding spectral slope.	70
7.2	Data acquisition and processing workflow.	83

List of Tables

2.1	Optimal gain settings following the Ziegler-Nichols method (<i>Ziegler–Nichols method 2023</i>).	27
3.1	Instrumental parameters of the AEROLI DWL (Vrancken and Herbst 2022.) . .	33
3.2	Top of table: Variables used to compute the synthetic lidar signals P_{mol} and P_{cirrus} . Bottom of table: Peak values of and the ratio of P_{mol} and P_{cirrus}	35
3.3	Data variables of backscattering ratio products.	36
3.4	Origin of data.	37
3.5	Origin of data.	38
5.1	Instrumental parameters of the AEROLI DWL (Vrancken and Herbst 2022). . .	52
5.2	Parameters of the input steps measured for the time response analysis. . . .	58
5.3	Parameters of the input steps measured for the time response analysis. . . .	59
7.2	Statistics of flight velocities of the HALO aircraft for the scenes j	85

Abbreviations

ACLAIM	Airborne Coherent Wind lidar for Advanced In-Flight Measurements
ADC	Analog-to-Digital-Converter
AEROLI	Aeronautics Lidar
AGC	Automatic Gain Controller
APD	Avalanche Photo Detector
ATTAS	Advanced Technologies Testing Aircraft
AVC	Automatic Volume Control
AWIATOR	Aircraft Wing with Advanced Technology Operation
BS	Beam Splitter
CALIPSO	Cloud-Aerosol lidar Infrared Pathfinder Satellite Observations
CAT	Clear Air Turbulence
CPL	Cloud Physics Lidar
DAQ	Digital Acquisition Card
DC	Direct Current
DD	Direct Detection
DFT	Discrete Fourier Transform
DLR	Deutsches Zentrum für Luft- und Raumfahrt
DWL	Doppler Wind Lidar
EMW	Electromagnetic Wave
EOM	Electro-Optical Modulator
FAA	Federal Aviation Association
FC	Fiber Coupler
FFT	Fast Fourier Transform
FoS	Factor of Safety
FOV	Field Of View
FWFIMI	Field Widened Fringe Imaging Michelson Interferometer
FWHM	Full Width Half Maximum
GLA	Gust Load Alleviation
HALO	High Altitude and Long Range Research Aircraft
HSRL	High Spectral Resolution Lidar
HV	High Voltage
IF	Interference Filter
LO	Local Oscillator
LOS	Line Of Sight
LTI	Linear Time-Invariant
NRMSE	Normalized Root Mean Squared Error

List of Tables

NTSB	National Safety Board
OF	Optical Fiber
OPA	Operational Amplifier
PBSC	Polarizing Beam Splitter Cube
PDF	Probability Density Function
PI	Proportional Integrating
PID	Proportional Integrating Derivative
PLL	Phase-Locked-Loop
PMTA	Photomultiplier Tube Array
PSD	Power Spectral Density
RMA	Reference Model for the Atmosphere
SNR	Signal-to-Noise Ratio
TF	Transfer Function
TIA	Transimpedance Amplifier
WALES	Water Vapour Lidar Experiment in Space

Symbols

α	Extinction coefficient [m^{-1}]
β	Backscattering coefficient [$\text{m}^{-1}\text{sr}^{-1}$]
R/BSR	Backscattering ratio
z	Altitude [m]
λ	Wavelength [nm], longitude [deg]
ϕ	Latitude [deg]
N	Particle density [m^{-3}]
F	King factor
p_s	Scattering phase function
Ω	Solid angle
τ	Optical depth
P	Power [W]
κ_T	Optical efficiency of the transmitter
κ_R	Optical efficiency of the receiver
G	Geometrical/Overlap function
A	Surface area [m^2]
r	Range [m]
Δr	Range resolution [m]
S	Lidar ratio [sr]
f	Frequency [Hz]
v	Velocity [m]
u	Radial velocity [m]
c	Speed of light in the vacuum: $3.00 \cdot 10^8 \text{ ms}^{-1}$
h	Planck's constant: $6.63 \cdot 10^{-34} \text{ Js}$
e	Electron charge: $1.60 \cdot 10^{-19} \text{ C}$
c	Speed of light in the vacuum: $3 \cdot 10^8 \text{ ms}^{-1}$
η	Quantum efficiency
S_k	Photocathode radiant sensitivity [A/W]
I_k	Photocurrent [A]
L_p	Radiant flux [W]
δ	Secondary emission ratio
E	Dynode interstage voltage [V]
n	Number of dynodes
a, k	Constants related to a PMT
α	Dynode collection efficiency
μ	Current amplification factor

List of Tables

U_{gain}	Control voltage of the Lidar Detector [V]
U_{out}	Output voltage of the Lidar Detector [V]
R_f	Feedback resistor of a TIA [Ω]
\mathcal{L}	Laplace transform
s	Complex variable
y	System output
Y	Laplace transform of y
u	System input/controlled variable
u	Laplace transform of u
H	Transfer function
K	System gain
e	System output error
r	Setpoint
τ	Time constant [s]
ω_0	Natural frequency [Hz]
k	Spring constant [Nm^{-1}]
c	Damping constant
ζ	Damping factor
K_p	Proportional controller gain
K_i	Integrating controller gain
K_d	Derivative controller gain
K_u	Ultimate proportional gain
T_u	Oscillating period
\mathcal{F}	Fourier transform
S	Power spectrum
C_k	Kolmogorov constant
ϵ	Energy dissipation rate
k	Wavenumber [m^{-1}]

Contents

List of Figures	i
List of Tables	iv
Abbreviations	v
Symbols	viii
1 Introduction	1
1.1 Context	1
1.2 Objective	3
1.3 Design Approach	5
2 Theoretical Background	7
2.1 Light Scattering at Small Particles	7
2.2 Lidar Basics	9
2.3 Lidar Signal Detection	20
2.4 Control Theory	23
2.5 Turbulence and Power-Law Scaling	27
2.6 Power Spectral Density PSD	28
2.7 WALES, Cirrus-HL and HALO-AC3	29
3 Horizontal Variability of Cirrus Clouds	33
3.1 Spectral Analysis	39
3.2 Magnitude of Backscattered Signal Power Variability	43
4 Experimental Set-Up	48
5 Characterization of the Detector Electronics	51
5.1 Mathematical Description of the Detector Chain	51
5.2 Time response - Experimental Derivation	55
5.3 Dark Current and Signal-to-Noise-Ratio	59
6 Automatic Gain Controller	61
6.1 Design and Implementation	61
6.2 Testing	64
7 Summary	69

Contents

Bibliography	73
Acknowledgements	79
Appendix	80

Chapter 1

Introduction

1.1 Context

CAT is defined as sudden severe turbulence occurring in cloudless regions that causes violent buffeting of aircraft. This term is commonly applied to higher altitude turbulence associated with wind shear. CAT is typically encountered outside of convective clouds, within and in the vicinity of mountain flow related, standing lenticular clouds and, in some cases, in clear air close to thunderstorms (FAA 2023). CAT also occurs due to breaks in laminar flow often encountered in the vicinity of jet streams and gravity waves. The local changes in wind speed and direction caused by turbulence are also called eddies, however there exists a large spectrum in the atmosphere in terms of spatial extent. The flight path of aircraft is only disturbed by a subset of the turbulence spectrum, associated with eddy sizes between 100 m and 1 km. This critical range of eddy sizes is called aviation-scale turbulence. Larger eddies only cause slow variations in the flight path that can be mitigated by the autopilot, while the effect of smaller eddies is hardly felt, as it is integrated over the surface of the aircraft (Sharman and Lane 2016). Aviation-scale turbulence can cause unexpected rolling moments, vertical acceleration, or abrupt changes in flight altitude. These sudden accelerations generate structural dynamic loads in the airframe, which may result in damage to the airplane or injury to the passengers (Sharman and Lane 2016, Tvaryanas 2003). In order to reduce fatigue and the risk of structural damage, airplanes are designed accordingly. However, that means that a higher structural mass has to be taken into account solely for turbulence protection. With the ongoing efforts to make commercial air transport more energy-efficient, mass reduction is an important strategy. The challenge is to make aircraft lighter, without compromising structural integrity and passenger safety. A common metric to characterize the resilience of a given structure in the face of an expected mechanical load is called Factor of Safety (FoS), see Equation 1.1. The federal aviation administration (FAA) specifies a FoS of 1.5 for airworthiness of the airframe of transport category airplanes (CFR 2023).

$$FoS = \frac{Yield\ Stress}{Working\ Stress} \quad (1.1)$$

Yield stress is the maximum stress a structure can undergo before plastic deformation sets in. Working stress, also called design load, is the maximum load the plane should ever see in service. A FoS of 1 will only just withstand the design load and no more (*Factor of safety* 2023). The airframe structure is designed in such a way that its yield stress matches the design load plus a reserve. The latter is derived from the parameters like maximum speed,

starting, landing, or maneuver accelerations, which are specific to the type of airplane and its intended range of operation. CAT is especially troublesome because it is often encountered unexpectedly and frequently without visual clues to warn pilots of the hazard. If not accounted for, the loads from these unexpected events may occasionally surpass the yield stress and cause damage and material fatigue over time. A safety factor of 1.5 represents a certain amount of reserve strength against the expected and unexpected loads acting on the flight vehicle.

As aforementioned, turbulence also poses a significant concern for passenger safety. According to various analyses of the U.S. national transport safety board (NTSB) and the FAA databases, 70 % of all reported weather-related accidents and incidents for commercial aircraft may be attributed to turbulence. From 2009 to 2022, 163 serious turbulence injuries for passengers and airline crew members have been reported. The FAA set guidelines in place to avoid turbulent conditions during flight and minimize the risk of injury if one should be encountered (FAA 2023). These include flying around regions where turbulence is predicted by weather models, or reducing the flight speed to decrease the impact of turbulence. These mitigation techniques, however, come at the cost of reduced efficiency and higher fuel consumption due to longer flying routes when circumventing turbulent areas.

When considering future climatological developments, vertical wind shear in the vicinity of atmospheric jet streams, which produce CAT, play a role. These fast-flowing air currents are sustained by the temperature difference between the cold poles and the warm tropics. With anthropogenic climate change, these conditions may be altered in a way that will affect the wind patterns of the prevailing jet streams. As a consequence, wind speeds of jet streams at cruising altitude and wind shear might increase, giving rise to more unstable conditions and a higher likelihood of CAT breaking out (Delcambre et al. 2013, Puempel and Paul D Williams 2019). Paul D. Williams 2017 used climate model simulations to analyse the CAT response to climate change and found that when doubling the carbon dioxide concentration, aviation-relevant light clear-air turbulence increases for all intensity categories from light to severe. In a more recent publication he presented a rigorous demonstration that confirmed the suitability of climate models for the task of producing future CAT projections (Paul D. Williams and Storer 2022). This being said, it is evident that the importance of effective methods for CAT mitigation will only increase with time.

One of these strategies contains the combination of on-board turbulence measurements and the aircraft's flight control actuators to enable a gust load alleviation system (GLA). The goal is to attenuate the effects of flying through a turbulent area by automatically redistributing the loads, minimizing the overall impact. This would allow for lighter aircraft without compromising the prescribed FoS of 1.5. Furthermore, a safer, more comfortable flight and a higher fuel efficiency could be achieved. Systems for GLA have been presented more than three decades in the past, with the earliest ones using accelerometers to measure gust loads. One example is an active control system for the Lockheed L-1011 aircraft, which was developed to reduce the loads at the wing tips, allowing for a larger wing span, and thus an improved fuel efficiency (Bendixen, O'Connell, and Siegert 1981). In the 80ies,

DLR designed and developed the Advanced Technologies Testing Aircraft System (ATTAS), as a new technology demonstrator. One of those new technologies included a nose boom to measure gusts and passing the measurements to a control system operating the wing flaps and elevators of the aircraft (Hahn and Koenig 1992). The performance of such a set-up is naturally limited due to a short leading time resulting from the time elapsed from the measurement at the nose boom, to the response of the actuators. To increase the leading time, the gust measurement must be done at a distance further ahead of the aircraft, giving the control systems and actuators more time to react. With this requirement, the need for remote-sensing techniques arises. In commercial aviation, it is common standard to use on-board weather radars to scout the conditions in front of the airplane. However, the use of current on-board weather radars is limited to situations where hydrometeors, like water droplets, are present, making them unfeasible for the detection of CAT. An obvious alternative, is using wind lidar technology, with which wind speed can be measured based on the relative motion of aerosols and air molecules. Robinson 1996, presented flight simulations for pitch control using feed-forward lidar measurements to alleviate turbulence-induced disturbances on aircraft. In the same year NASA published a paper describing the Airborne Coherent wind Lidar for Advanced In-flight Measurements (ACLAIM). The purpose of this program was to develop a prototype system to test the feasibility of GLA systems using a coherent wind lidar. Since then, many efforts have been undertaken by Airbus (AWIATOR) and DLR, among others, to develop a doppler wind lidar (DWL) for gust load alleviation. Different lidar designs were proposed, however newer insights drive the focus of DLR's research towards direct-detection Doppler wind lidar (DD-DWL). The reason is that as opposed to coherent DWL, which relies on the presence of aerosols for a reliable measurement, DD-DWL can operate solely with Rayleigh scattering at atmospheric molecules. This makes the DD-DWL more feasible for operation at cruising altitudes. The following concentrates on the GLA system proposed by Fezans, Joos, and Deiler 2019 and the most recent design of the DD-DWL developed by Vrancken and Herbst 2022.

1.2 Objective

This thesis deals with the development of an automatic gain control for the detector of DLR's DD-DWL, which shall ensure nominal operation regardless of variable lidar return-signal power caused by clouds. The typical cruising altitude for commercial aircraft typically lies between 9 to 11 km.

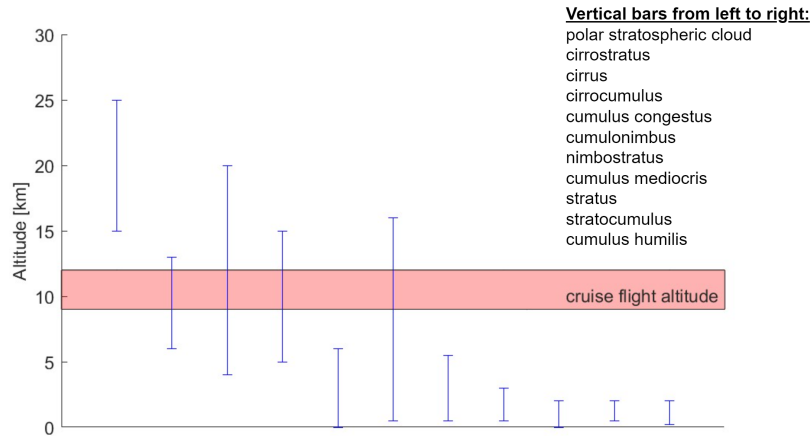


Figure 1.1: Typical altitudes at which different cloud types occur.

As seen in Figure 1.1 different types of cirrus clouds (ci) and cumulonimbus (Cb) form at those altitudes. The latter is usually avoided as storm clouds produce strong convection which is could harm the passengers. For this reason, Cb are set aside in the present study, but should be investigated in future works. Cirrus clouds are not a safety concern, but do have a strong influence on optical measurements. The return signal power of a DWL can go up several orders of magnitude when approaching a cirrus cloud, leading to over-saturation and possibly damage of parts of the detector chain. An easy solution would be to adapt the gain to the maximum signal level expected during flight. This however would have the consequence that signals from clear sky become so small that the ADC won't operate in optimum conditions, depending on the chosen hardware. Furthermore, while flying through the cloud, variations in the cloud optical density will also produce variations in the return signal, which is undesirable for digital signal processing. A more practical solution would be to dynamically adapt the gain of the detector in a way, that the return signal power level stays roughly constant at all times. In radio technology such a system is called Automatic Gain Control (AGC), also known as Automatic Volume Control (AVC), since it keeps the volume of the radio constant regardless of variations in the received signal power. The AGC was invented by Harold Alden Wheeler in 1925 and its use has been common practice ever since 1930 (Engineering 2001)¹. For the lidar system under discussion, an AGC shall be designed to meet the requirements posed by the conditions at cruising altitude, when approaching and flying through cirrus clouds. For this purpose, a study is conducted based on High Spectral Resolution Lidar (HSRL) observations from the WALES lidar on DLR's airborne scientific platform HALO. Results from this study are used to formulate the boundary conditions of a validation scheme for the AGC.

¹The interested reader is referred to Küpfmüller 1928 for more detail on automatic gain controllers

1.3 Design Approach

Previously, the potential of GLA systems for reducing the risk of injury to passengers and damage to the aircraft in the face of turbulence was mentioned. For such a system to be feasible, a nominal operation must be guaranteed throughout all flight phases. Especially in the vicinity of jetstreams at cruise flight altitudes, there is a high risk of CAT. For this reason, but also to limit the scope of this thesis, the topics discussed henceforth focused on the conditions at altitudes from 6 km to 11 km². At these altitudes it is common to encounter cirrus clouds. Even though, they pose no risk to the aircraft, they might inhibit the operation of a GLA system based on DWL measurements. The attenuated backscatter signal received by a lidar detector depends on the coefficients for extinction α and backscatter β , which are functions of the cloud's spatial structure. The fluctuations in the radiative properties may introduce large variations in the return signal level. If the lidar detector is adjusted for clear air measurements with a high gain, any cloud contamination will cause the measurements to saturate, potentially rendering them unusable for wind detection. On the other side, reducing the gain to a level which allows measurements at the highest expected backscattering conditions is not favourable for the SNR. To achieve a good SNR and avoid a loss of resolution, the detector gain should be set in a way that the measurement values cover as much of the dynamic range of the Analog-to-Digital-Converter (ADC) as possible. To achieve this, an Automatic Gain Controller (AGC) is designed to keep the output signal of the detector within a reasonable range around a set-point with a good SNR.

Assuming that wind speed is considerably lower than flight speed, the optical thickness of a cloud can be seen as stationary, limiting the variability to the spatial dimensions. Since aircraft move primarily horizontally through space during the cruising phase, only horizontal variability shall be considered in the following. Even though the clouds are assumed stationary, the fact that the aircraft is moving through it, causes the backscattering conditions at the instantaneous position along the flight path to vary. In order to estimate the typical magnitude and frequency of backscattering fluctuations inside cirrus clouds, horizontal profiles of airborne lidar observations are investigated in Chapter 3. The cirrus cloud study includes the use of two mathematical tools. Firstly, the power spectral density (PSD) is used to examine the spectral distribution of the horizontal backscattering variations. Secondly, expected changes in the magnitude of synthetic lidar signals are analysed by computing a probability density function (PDF) along the horizontal dimension. The synthetic lidar signals represent the attenuated backscattering measurements of an airborne, forward looking DWL. Backscattering ratio products computed from lidar measurements on DLR's High Altitude and Long Range Research Aircraft (HALO) are used to conduct the study. The results of the study serve the setup of the functional requirements of the AGC presented in Chapter 6.

The AGC shall be developed for an existing lidar system (AEROLI) (Vrancken and Herbst

²Cruise flight is typically between 9 km and 11 km, however data from lower altitude levels are included in the analysis.

2022), which means that the hardware restrictions need to be considered as well. Regarding the hardware requirements, a series of experiments are carried out in Chapter 5, in order to identify the input-output relationship and time response of the detector electronics, so that a suitable controller can be designed. The controller shall then be incorporated into existing software for data acquisition, which is implemented in MATLAB. Since the lidar system will not be flight tested within the time frame of this work, a laboratory experiment is set up to validate the AGC. For simplicity, only the detector of the Lidar system is used in the set-up portrayed in Chapter 4. Laser pulses are created using a CW laser and an electro-optical modulator (EOM) to imitate the pulsed operation of the AEROLI laser transmitter, and in particular the temporally longer backscatter signals. The variations of the backscattering are simulated using a rotating neutral density filter with gradual optical depth. The optical behaviour due to ice cloud contact is simulated with said filter by turning it left and right with a servomotor in a pseudo-arbitrary fashion and thus simulating the variability scales of the cloud as determined in Chapter 3. With this set-up, the controller parameters are manually optimized. Figure 1.2 illustrates the workflow of the design approach. Two separate branches, the cirrus study and the detector characterization, provide the input for the iterative validation test, with which the design parameters of the controller are optimized.

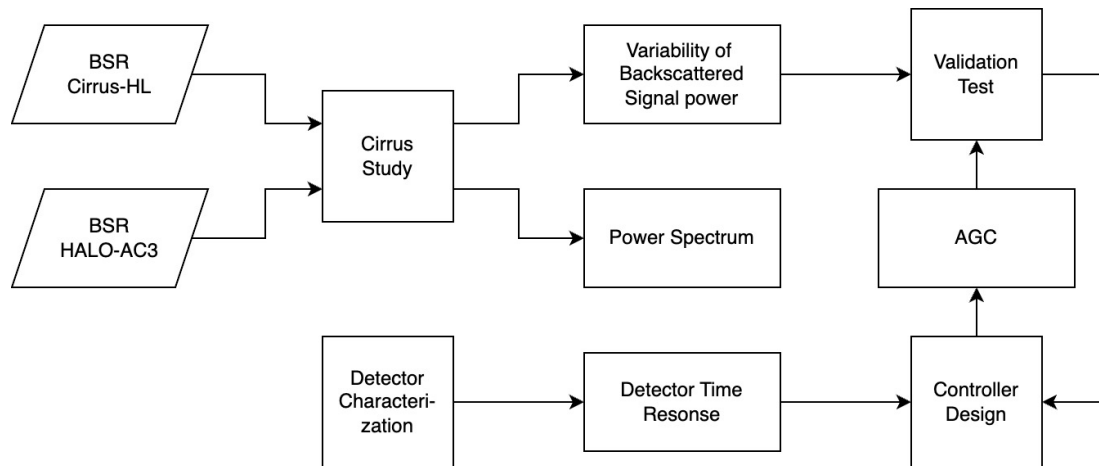


Figure 1.2: Workflow of the design approach of the automatic gain controller.

Chapter 2

Theoretical Background

2.1 Light Scattering at Small Particles

Light scattering is a phenomenon which occurs, when an incident electromagnetic wave (EMW) sets electric charges in a medium into oscillatory motion. These oscillating charges then emit a secondary wave, which is the scattered wave. The case for which the frequency of the scattered wave is identical to that of the incident one, is called elastic scattering. There are more complicated processes, which are accompanied with a change in the frequency of the EMW and are called inelastic scattering processes, however, these processes fall outside of the scope of this thesis.

In the atmosphere mainly three types of scattering mechanisms exists, namely Rayleigh scattering, Mie scattering and geometrical optics. The scattering regime governing a given light-particle interaction depends on the size of the scattering particle in relation to the wavelength of the incident light. Rayleigh scattering occurs when the scatterer's size is very small compared to the wavelength. In the atmosphere Rayleigh scattering happens when light interacts with air and is considered a consequence of the electric polarizability of the molecules which make up the air (Efremenko and Kokhanovsky 2021). The oscillating electromagnetic field of the incident light turns the molecule into a radiating dipole. The radiation emitted from the molecule is then regarded as the scattered light. Radiative processes are described by their scattering and extinction coefficients, which are related to the amount of light which is scattered or absorbed, respectively. The extinction coefficient is the sum of the scattering and absorption coefficient and corresponds to the amount of light that interacts at all with matter. The molecular scattering coefficient can be expressed analytically by (Bodhaine et al. 1999):

$$\beta_{mol}(z, \lambda) = \frac{24\pi^3(n^2 - 1)^2}{N(z)^2(n^2 + 2)^2} \frac{1}{\lambda^4} F(\lambda), \quad (2.1)$$

where λ is the wavelength of the incident light, n is the refractive index of air $N(z)$ is the molecular density as a function of altitude z and $F(\lambda)$ is the so-called King factor. The latter contains information about the depolarization ratio, which accounts for the anisotropy of air molecules (Efremenko and Kokhanovsky 2021) and is not further discussed here. β_{mol} is inversely proportional to the fourth power of the incident wavelength, which means that light at small wavelengths is scattered much stronger by molecules than light at large wavelengths. This explains the color of the blue sky at day and the red horizon at dusk and dawn. When the sun is high in the sky, more blue light reaches the eye of an observer on the ground, as it

is scattered stronger in the atmosphere. If the sun is low on the horizon, the sunlight travels a longer distance through the atmosphere so that much of the blue light is filtered due to scattering before it reaches the observer.

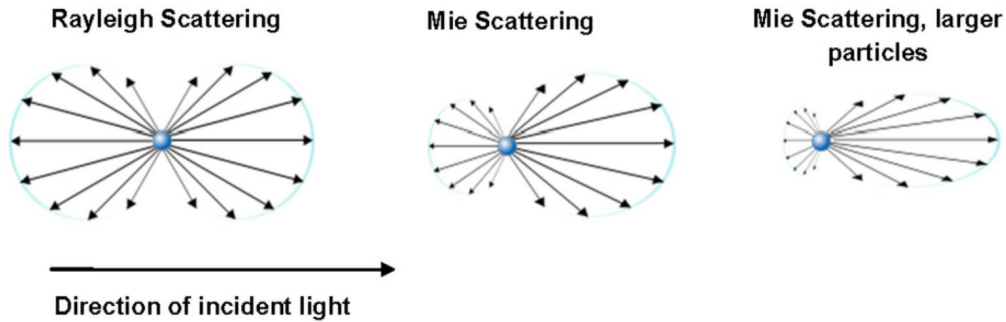


Figure 2.1: Directionality of scattering processes (Castellani et al. 2014).

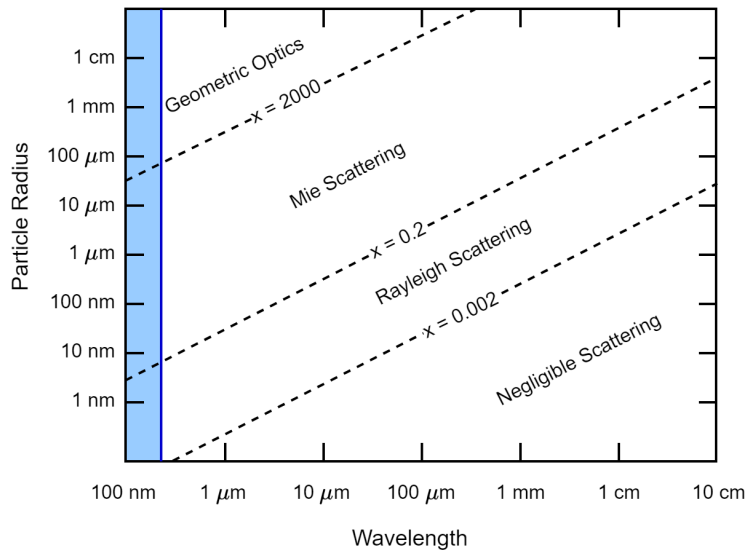


Figure 2.2: The scattering regimes for a given wavelength and particle size (Caballero 2014)

For active optical instruments like the lidar (discussed later in this chapter), the scattering coefficient in the backwards direction, also called backscattering coefficient β (as it shall be denoted in the further course of this work) and the extinction coefficient α are of importance. When light is scattered at a particle, it is mostly accompanied with a change in direction of the incident light, see illustration in Figure 2.1. The directionality of a scattering process is described by the scattering phase function $p_s(\Omega)$, where Ω is the solid angle, however, it will not be further discussed. Integrating α over a distance r yields the optical depth τ (indicated as the integral in Equation 2.2) (Gimmestad and Roberts 2023).

As the size of the scattering particle becomes similar to the wavelength or even larger, Mie scattering takes over. In atmospheric sciences Mie scattering is often referred to as particle or aerosol scattering, as is it the mechanism describing the radiative processes due to larger particles suspended in the air. The Mie theory is derived from Maxwell's equations and describes the interaction of a plane wave with a spherical particle of arbitrary size. The problem is formulated by expanding the incident plane wave, as well as the scattering field into radiating vector spherical harmonics. The solution of the Mie problem allows to calculate the total optical cross section of the scatterer (related to amount of scattered light) and how much of the light is scattered in which direction. At even larger particle sizes, the Mie solution converges to the lower size limit of geometrical optics ([Mie scattering 2023](#)).

Geometrical optics describes the propagation of light as rays, which travel as straight lines in homogeneous media. Light interacting with matter is no longer referred to in terms of scattering, but refraction. Refraction occurs at the interface between two materials with different refractive indices and is described by Snell's laws. Atmospheric particles for which the geometric optics approximation applies are hydrometeors like water droplets and ice crystal, which size can range from micrometers up to millimeters.

Figure 2.2 represents the three different scattering regimes discussed above in relation with the scattering particle size and the wavelength. The lidar system to be introduced in later chapters uses ultra-violet light at 355 nm wavelength, which is marked in Figure 2.2 as a blue dashed line. A lidar signal at that wavelength exhibits scattering from all three mechanisms aforementioned. However, the chosen wavelength is for specialized use of the lidar under clear sky conditions, where molecular scattering dominates.

2.2 Lidar Basics

lidar (Light detection and ranging) is a powerful optical remote sensing technique extensively used in atmospheric sciences to measure properties of the atmosphere at long distances. A multitude of lidar systems exists that is used for specific applications. The main advantage of lidar when compared to the related technique of Radar (Radio detection and ranging), stems from the selection of the wavelength that is used for the measurement signal. With light in the optical regime, ultra violet ($\sim 10\text{-}400\text{ nm}$) to infrared ($\sim 700\text{ nm}\text{-}1\text{ mm}$), the wavelengths used in lidar are a million to a billion times smaller that the ones used in radar ($\sim 1\text{-}100\text{ mm}$ for microwaves). With these shorter wavelengths it is possible to detect aerosols and molecules in the atmosphere. For instance, Radar needs the presence of large particles (e.g. water droplets) in the air to be able to detect any kind of atmospheric processes like wind, whereas lidar can do so under clear sky conditions by using the backscatter of molecules. In the following, the lidar principle shall be discussed and subsequently a more detailed description of the direct-detection Doppler wind lidar (DD-DWL) and coherent DWL shall be given. The focus lies on the AEROLI DD-DWL, as it is subject to this thesis. Lastly, the High Spectral

Resolution lidar (HSRL) technique shall be explained to give some understanding about the WALES instrument used to create the data products studied in Chapter 3.

As most active remote sensing instruments, the lidar consist of a radiation source, a transmitter, a receiver, a detector a analog-to-digital converter (ADC) and a computer to process the measurement data. A simplified schematic is shown in Figure 2.3. The most common

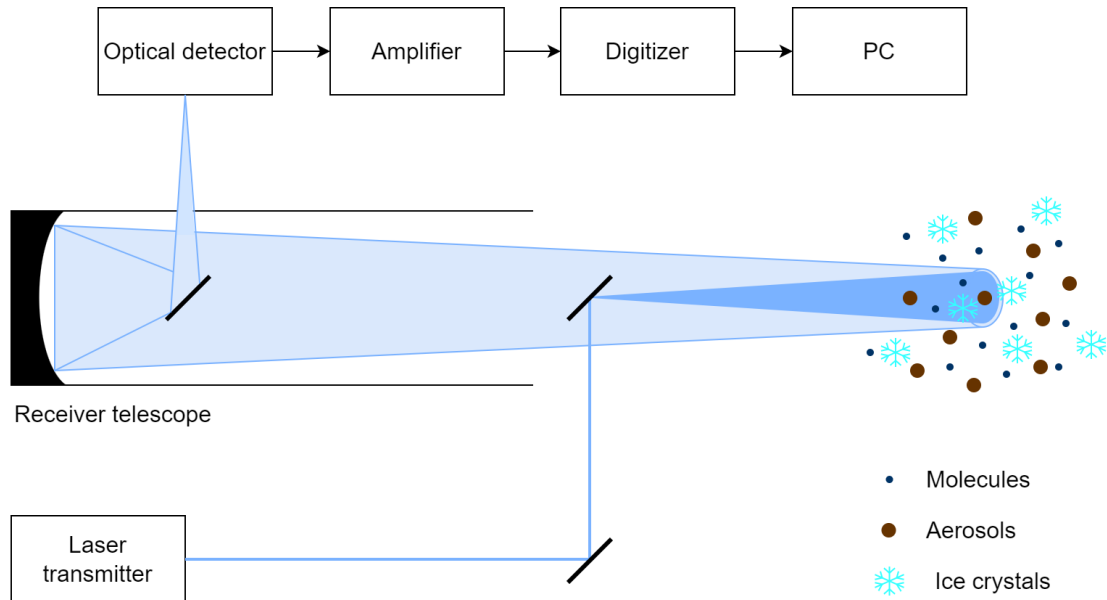


Figure 2.3: Simplified synopsis of a co-axial lidar system.

transmitter-receiver configurations for lidars are co-axial, bi-axial and common optics, the first of which is depicted in Figure 2.3. Co-axial means, that the transmitter and receiver are physically separated, but share the same optical axis. The transmitted laser beam is routed into the optical axis of the receiver telescope. The transmitted light is scattered on atmospheric particles like molecules, aerosols or hydrometeors like ice crystals or water droplets. A small fraction of the laser light is scattered directly back and captured by the receiver telescope and redirected to the optical detector. For the development of any measurement system that shall be optimized for a specific application, a descriptive model is needed to relate the inputs to the outputs of the system. The lidar equation models the system receive power as a function of range, based on instrumental and atmospheric parameters. It essentially describes the way in which a pulse of laser light is modified by continuous scattering on atmospheric particles as it propagates out through space and back to the detector. In the following, a model for the most basic type of lidar, known as *elastic back-scatter lidar*, is presented. Elastic scattering occurs when no energy is absorbed during the scattering process, meaning that the re-emitted light has the same wavelength as the incident light. Symbolically, the range-dependent lidar signal model can be written as (Gimmestad and Roberts 2023):

$$P_S(r) = P_0 k_T k_R G(r) \left(\frac{A}{r^2} \right) \left(\frac{c\tau}{2} \right) \beta(r) \exp \left[-2 \int_0^r \alpha(r') dr' \right] \quad (2.2)$$

where the first part of the right-hand side are instrumental variables. These are the transmitted laser power P_0 , the transmitter and receiver optical efficiencies k_T and k_R , the geometrical function $G(r)$, and the receiver solid angle A/r^2 . The model is written as a continuous time-varying signal of the received power. In practice however, the return signal is digitized at discrete range intervals given by the term $\frac{c\tau}{2} = \Delta r$, which are called range bins or range gates. The range resolution thus depends on the sampling frequency $1/\tau$ of the digitizing circuit used, where τ is the sampling time. The second part of the right-hand side are atmospheric parameters, namely the back-scattering coefficient β and the extinction coefficient α . The exponential of two times the integral of α over the range gives the optical two-way transmittance of the photons through the atmosphere. The signal represented by the model in Equation 2.2 is also referred to as attenuated backscatter. Both back-scattering and extinction coefficient are unknowns, which means a relation between both, found by means of empirical or theoretical methods, has to be assumed in order to determine either one of them from lidar measurements. For some cases this relation, called extinction to back-scattering ratio, or lidar ratio, is linear. For pure molecular scattering, a well established approximation for the lidar ratio exists, given by (Gimmetstad and Roberts 2023):

$$S_{mol} = \frac{\alpha_{mol}}{\beta_{mol}} = \frac{8\pi}{3} [sr] \quad (2.3)$$

where the subscript *mol* stands for molecular.

For scattering at large particles, e.g. ice crystal, the lidar ratio is assumed constant as well and values can be retrieved from look-up tables created from former experience with cirrus lidar observations. In Hlavka et al. 2012, Cloud-Aerosol lidar Infrared Pathfinder Satellite Observations (CALIPSO) satellite products are validated using the airborne Cloud Physics Lidar (CPL). Hlavka et al. explain different methods for retrieving the aerosol lidar ratio S_{aer} from lidar observations depending on (amongst others) the optical depth of a specific cloud. Average ice cloud lidar ratios derived from CALIPSO (25.4 sr) and CPL measurements (23.5 sr) are presented. These values are given for a wavelength of 532 nm. In Vaughan et al. 1998, a common reference for atmospheric parameters at DLR's institute of atmospheric physics, a lidar ratio of 13.7 sr is given for cirrus clouds at 7.5 km - 9.5 km altitude. It must be noted that this document is already >25 years old and that the values are derived from infrared observations. The varying values of the lidar ratio arise from different micro-physical conditions inside the cloud. Different size distributions and ice crystal shapes may influence the lidar ratio. For the calculations done in Chapter 3 and other parts of this thesis, a common value of 20 is assumed for the lidar ratio.

The model in Equation 2.2 also rests on the following implicit assumptions: The entire laser pulse is contained within one range bin, all received photons experienced only one scattering event on their trip through the atmosphere (single scattering approximation), and only one laser pulse is in the atmosphere during the time in which one profile is recorded (Gimmetstad and Roberts 2023). All these assumptions are valid for the application under discussion here.

The geometrical function $G(r)$, also called overlap function, is a range-dependent function which states the degree of overlap between the diverging laser beam and the receiver field of view (FOV). Together with the $1/r^2$ -term, the overlap function determines the shape of

the lidar signal, as illustrated in Figure 3.1. The general shape of the geometrical function resembles a simple sigmoid curve. The origin of this shape is shown in a geometrical context in Figure 2.4. At close ranges, no light is captured by the receiver optics (simplified as a lens and a field stop). The further the pulse moves down range, the more light enters the field stop until all of the light is captured. This is the range at which $G(r)$ reaches unity. The range before unity (total overlap) is reached, is called crossover range.

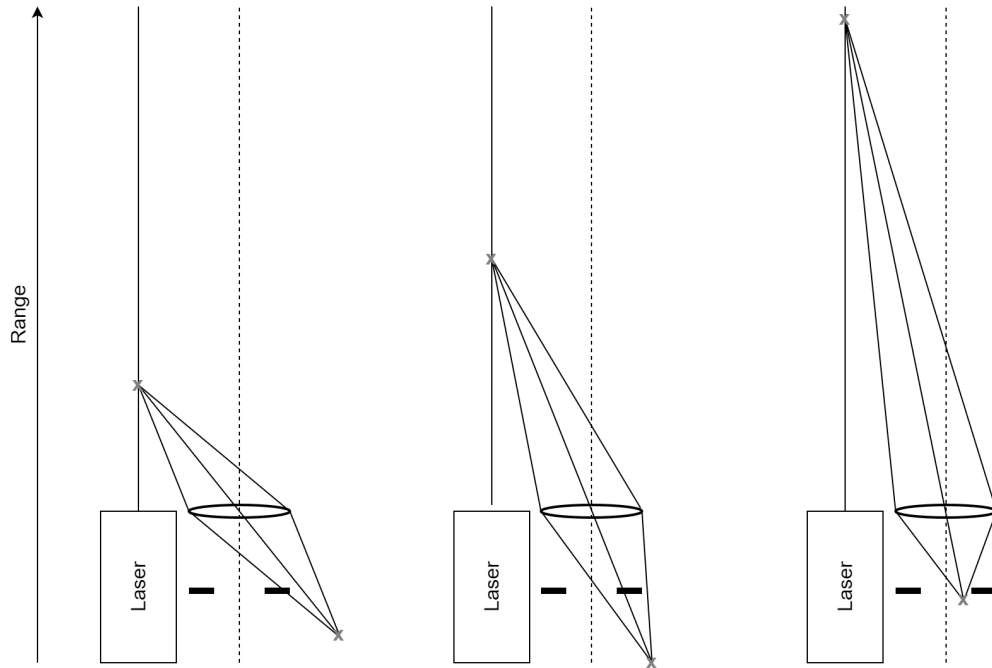


Figure 2.4: Origin of overlap function. Laser light captured by receiver optics at three different ranges.

This range is an important design variable, because it determines the minimum range at which valid measurements can be conducted. Furthermore, the minimum range r_{min} drives the dynamic range of the measurements. If r_{min} is several kilometers, the $1/r^2$ term will dominate, resulting in small variability in the measurements. While this might be used to suppress close-by signal, it has the consequence of a reduced SNR. This is why it is often desirable to make r_{min} as small as possible. However, challenges for handling the large dynamic range may occur. This exactly is the case for Doppler wind lidars used for gust load alleviation. The range of interest for turbulence detection at aviation scales lies a 50 to 300 meters ahead of the aircraft. The geometrical function needed to enable measurements at these distances gives rise to dynamic ranges of up to two orders of magnitude.

Doppler Wind lidar

Doppler wind lidars (DWLs) are broadly used in atmospheric sciences, especially for the study of the boundary layer and have become state-of-the-art measurement devices over the years. They can take range resolved measurements from the distance, as opposed to mechanical or sonic anemometers, which can only measure locally (in-situ). DWLs have been adopted for several commercial applications like measurements of the wind field to control the operation of wind turbines or include wind shear observations for operations on major airports (Han et al. 2020).

Another application mentioned in Chapter 1, is the airborne measurement of turbulence with DWL for gust load alleviation. Figure 2.5 shows the concept of a forward-pointing lidar-based feed-forward gust alleviation system (Vrancken and Herbst 2019). Information about the wind field ahead is measured by a DWL and fed to the GLA controller, so that corrective actions can be undertaken to reduce the load of gusts on the airframe.

As the name suggests, the Doppler wind lidar is based on the Doppler effect manifested on the return signal.

Any time varying signal can be described in frequency-space by its spectrum and the effect of Doppler shift can be observed in the change of said spectrum. The solid line in Figure 2.6 describes the superposition of a broad band and a narrow band Gaussian curve, representing the total spectrum from combined Rayleigh and Mie scattering. The broad spectrum from molecular scattering is owed to Doppler broadening due to the Brownian motion of molecules. The Brownian motion experienced by aerosols is negligible so that the spectrum of a monochromatic light source backscattered from aerosols remains sharp. The collective motion of atmospheric particles like molecules, aerosols or hydro-meteors caused by wind, produces a shift in the spectrum of light scattered at those particles, see dashed line in Figure 2.6. With the measurement of this Doppler shift of the spectrum, the relative wind speed in the line-of-sight vector of the instrument can be computed with the well-known equation:

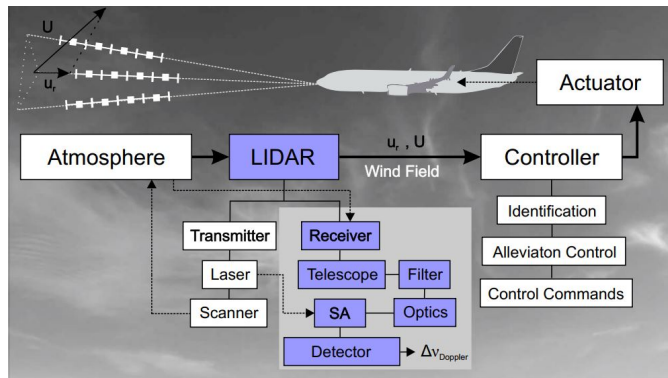


Figure 2.5: Concept of a lidar-based feed-forward gust alleviation system.

$$\Delta f_{Doppler} = \frac{2u}{\lambda_L}, \quad (2.4)$$

where $\Delta f_{Doppler}$ is the Doppler frequency shift, u is radial component of the wind speed, and λ_L the wavelength of the laser. The most commonly used techniques for lidar-based

wind measurement are heterodyne detection (throughout the lidar community termed as "coherent detection") and direct-detection.

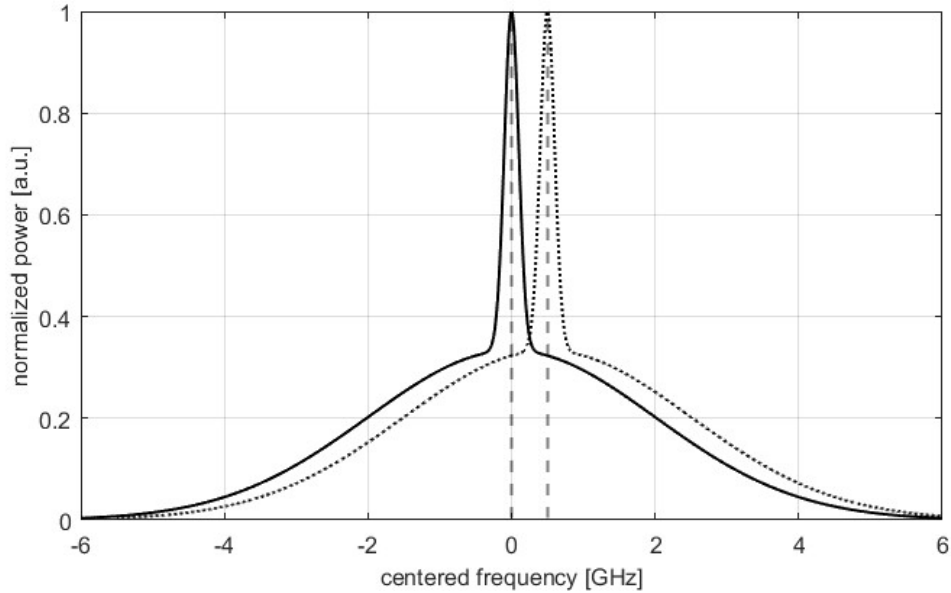


Figure 2.6: Solid line: combined molecular and aerosol back-scattering spectrum. Dashed line: combined spectrum Doppler shifted by Δf .

In coherent detection, wind speed is retrieved by analyzing the beat signal resulting from heterodyne mixing of the narrow spectral line backscattered by aerosols (Vrancken 2016). In direct-detection, wind speed fluctuations along the line of sight directly retrieved from air molecule's backscatter are measured by determining the Doppler shift in the backscattered signal with interferometric methods (Vrancken 2016).

Coherent DWL

Coherent DWLs analyse the beat signal resulting from mixing the received laser signal with the signal from a local oscillator (LO). The continuous wave (cw) LO and the pulsed return signal have a similar laser frequency and are synchronized by a phase-locked-loop (PLL) allowing them to interfere in a way, which produces a lower frequency beat. For the superposition of two sinusoidal waves with the frequencies f_1 and f_2 , the mathematical description is as follows:

$$\sin(2\pi f_1 t) + \sin(2\pi f_2 t) = 2\sin\left(2\pi \frac{f_1 + f_2}{2} t\right) \cos\left(2\pi \frac{f_1 - f_2}{2} t\right). \quad (2.5)$$

The resulting signal is a sine with a frequency which is the average of the initial frequencies, modulated by a cosine with a frequency which is half the difference of the initial frequencies

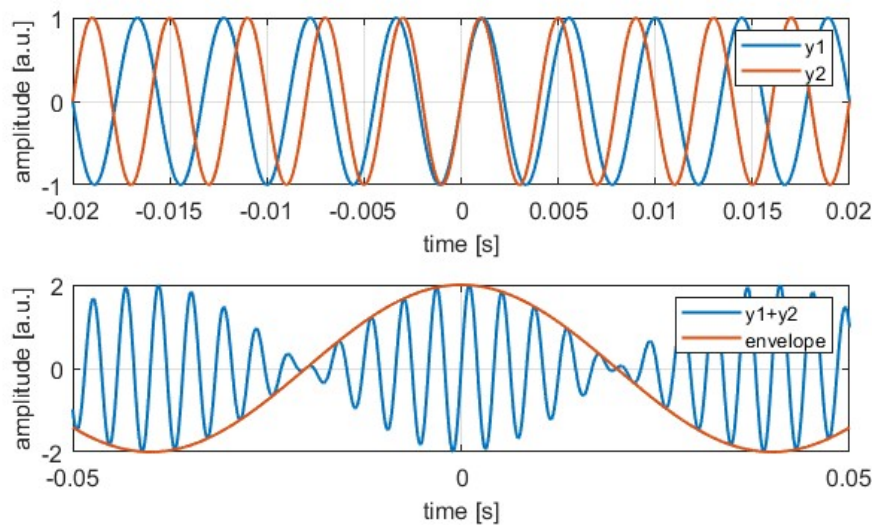


Figure 2.7: Top: sinusoidal signals y_1 and y_2 with slightly different frequencies. Bottom: resulting beat from superposition of y_1 and y_2 .

([Wave Interference and Beat Frequency 2023](#)), see Figure 2.7. As the envelope passes twice per period through zero, the effective beat frequency is $f_{beat} = |f_1 - f_2|$. In signal processing and electronics, this method is called heterodyne mixing and is widely used to facilitate the amplification or detection of high frequency signals.

Optical detectors are too slow to resolve the electromagnetic field of the laser signal and thus act as a low-pass filter to this high-frequency signal. The beat signal resulting from heterodyne mixing the LO signal and the laser return signal contains the information about the Doppler shift of the received signal, with which the wind speed is computed. Assuming a stationary DWL, and a radial wind speed of 30 m/s, a Doppler shift of $1.69 \cdot 10^8$ is computed by using Equation 2.4. After digitizing the signal, a Fast Fourier Transform (FFT) may be computed to extract the beat frequency, which is the Doppler shift corresponding to the 30 m/s wind speed. Coherent DWL is a widely used remote sensing technique for measuring wind speed due to the relatively simple principle of heterodyne mixing. Nevertheless, there is a caveat. With increasing altitude, the spectral line from particle (Mie) scattering fades due to the ever decreasing prevalence of aerosols, as seen in Figure 2.8. The analysis of heterodyne mixing of purely molecular (thus spectrally broad) backscatter signals are virtually impossible. This means that the method of coherent detection is ineffective or even impossible for airborne applications at high altitudes where the aerosol concentration is small to non-existent.

Direct-Detection DWL

The approach of direct-detection poses a promising alternative since it is adapted for molecular scattering and doesn't rely on the presence of aerosols. The direct-detection method is

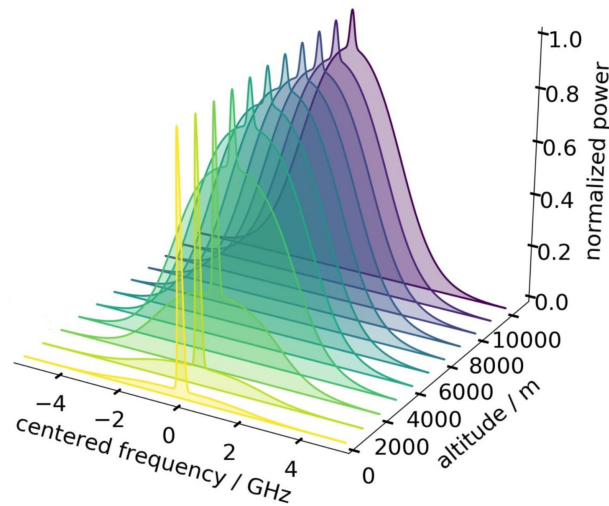


Figure 2.8: Combined Rayleigh and Mie spectrum for different altitudes (Tenti S6 model, Herbst 2019). The spectra have large differences in their magnitude depending on the altitude and have been normalized here.

based on spectroscopy, commonly realized with interferometry. This means that the information about the line-of-sight wind speed contained in the spectrum of the back-scattered laser signal, is converted to spectral information with the use of an interferometer. A multitude of interferometer types exists, e.g., double slit, Farby-Perot, Fizeau, Michelson, Mach Zehnder, etc. The following explanation is limited to the field-widened, fringe-imaging Michelson interferometer (FWFIMI) of the AEROLI system (Vrancken, Wirth, et al. 2016), shown on the right-hand side of Figure 2.9. The "field-widened" part of this specific interferometer describes its ability to accept angular distributed light without a reduction in the fringe contrast. This design makes the interferometer suitable for measurements with large incident angles in the near field (50-300 m), which is required for the detection of aviation-relevant CAT. As can be seen in Figure 2.9 both the transmitted and received signal are injected into one common optical fiber with the fiber coupler *FC*. The combined signal is then passed to the Michelson interferometer. Inside the interferometer, a beam splitter divides the incident light beam into two arms with slightly different lengths. The separated light beams travel different distances, depending on the design optical path depth, which introduces a phase difference when they are merged back together. Due to the mutual coherence of the two light beams, an interference pattern is produced. In this particular design, one of the interferometer mirrors is slightly skewed, producing almost linear interference fringes, as opposed to circular ones. The 2D fringe pattern may then be squeezed along the z-axis with a cylindrical lens, to create a one-dimensional light beam with an intensity variation along the y-axis (fringe pattern).

Figure 2.10a shows the three-dimensional signal, where the first dimension represents the fringe measured across the channels of the detector, the second dimension the range resolution of the lidar signal and the third dimension the normalized intensity of the signal. This

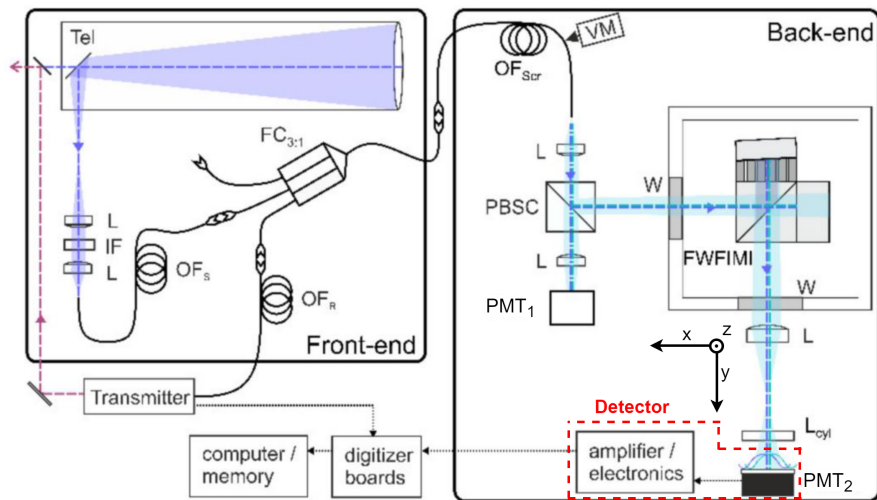
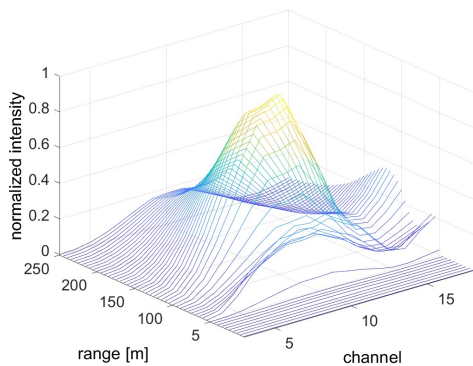
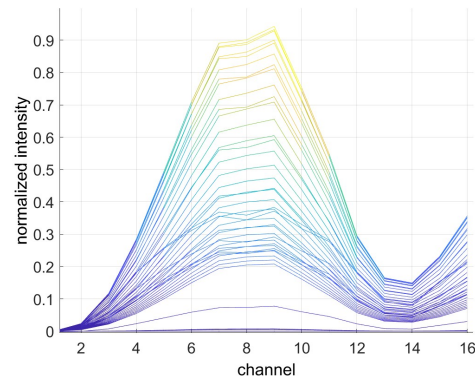


Figure 2.9: Schematics of the AEROLI direct-detection Doppler wind lidar, based on a field-widened fringe-imaging Michelson interferometer (*FWFIMI*). *Tel*: telescope, *L*: lens, *L_{cyl}* cylindrical lens, *IF*: interference filter, *FC*: fiber coupler, *OF*: optical fiber, *PBSC*: polarizing beam splitter cube, *PMT_{1,2}*: photomultiplier, *W*: window (Vrancken and Herbst 2022).

figure is produced from data taken during a ground validation campaign of the AEROLI system (Linsmayer and Vrancken 2023). Figure 2.10b shows the plot in Figure 2.10a from the front view.



(a) Range dependent, normalized fringes from ground measurements (Linsmayer 2023).



(b) Front view of the range dependent fringes.

Taking a slice of the data in Figure 2.11 along the range dimension, gives the combined attenuated backscattering signal (large peak) and reference signal of the laser transmitter (small peak at ~ 10 m).

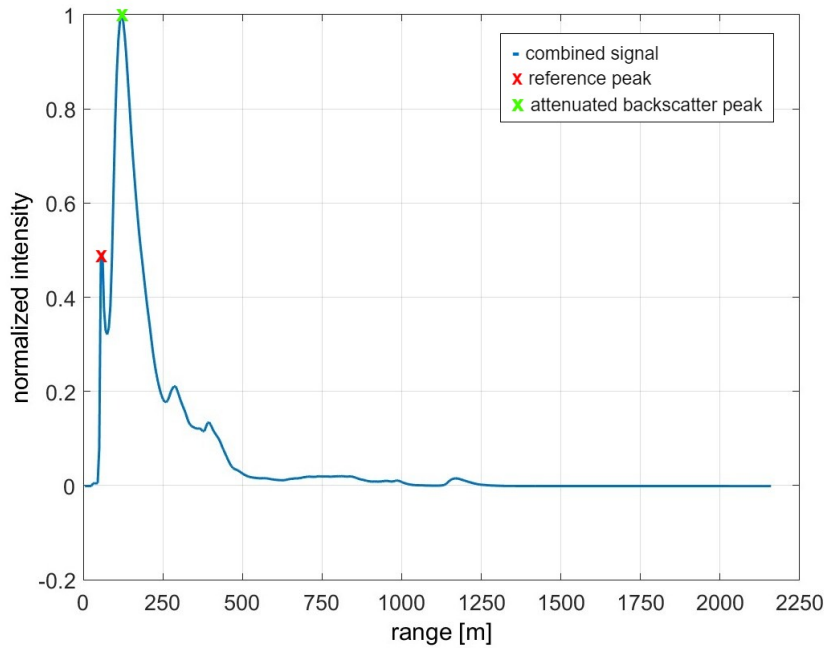


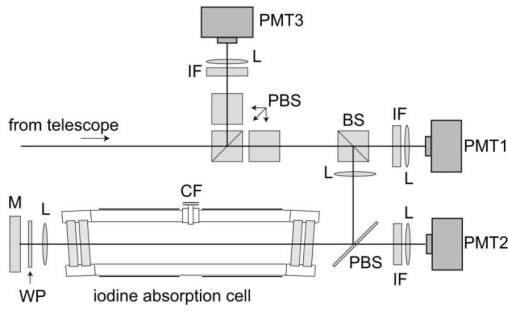
Figure 2.11: Combined reference and attenuated backscatter signal from ground measurements (Linsmayer 2023).

Depending on which range bin is selected, either the fringe from the return signal or the reference signal can be extracted. The fringes have a cosine shape, as shown in (Herbst 2019). By fitting a cosine onto each of the fringes (return signal and reference signal), their relative positions along the channel dimension can be obtained with sub-channel precision. The relative position is then translated to a frequency difference and subsequently to wind speed.

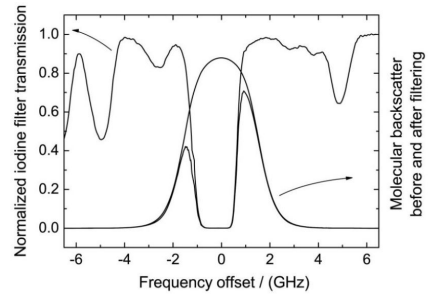
The study in Chapter 3 is conducted with data products derived from HSRL observations of the WALES airborne demonstrator lidar. To gain a better understanding of these data, the HSRL technique is explained in the following.

High Spectral Resolution lidar (HSRL)

The high spectral resolution lidar technique offers the possibility to retrieve molecular and aerosol backscatter and extinction coefficients from the attenuated backscatter signal described by Equation 2.2. The retrieval of aerosol information is an important discipline in atmospheric physics and climate research and used to describe radiative processes in the atmosphere. The principle is based on the separation of the molecular and aerosol signal. This can be achieved with a spectral method, either with similar spectrometers as in DD-DWL or with spectrally narrow molecular absorption lines. By lucky coincidence, Iodine I_2 absorption lines are within the reach of the second harmonic of the work-horse Nd:YAG



(a) Receiver of a high spectral resolution lidar based on an Iodine absorption filter (Esselborn et al. 2008). BS, beam splitter; CF, cool finger; IF, interference filter; L, lens; M, mirror; PBS, polarization beam splitter; PMT, photomultiplier; WP, quarter-wave plate.



(b) Iodine filter transmission spectrum and molecular backscatter before and after filtering (Esselborn et al. 2008).

solidstate laser at 532nm. Esselborn et al. 2008 presented an airborne HSRL lidar based on an iodine absorption filter. In the course of this thesis, backscattering ratio products derived from measurements with this particular lidar system will be used to study the horizontal variation of the backscattering coefficient of cirrus clouds.

In the following, the steps to extract the backscattering ratio from the combined aerosol and molecular attenuated backscatter observations are explained. Figure 2.12a shows the receiver of the mentioned lidar system. The received light is split into its polarized components with a polarizing beam splitter cube. The cross-polarized component P^\perp is directed to photomultiplier PMT3 whereas the parallel-polarized component P_C^\parallel is transmitted. In both paths a second polarizing beam splitter is placed to reduce polarization cross talk. The transmitted parallel component of the backscatter signal is split again, such that half of its energy is directed into what is named the molecular channel. The other part is guided to the combined channel where the intensity of the combined backscatter is measured by PMT1. Within the molecular channel light travels through the iodine vapor cell and is reflected at a 0° mirror. The plane of polarization is rotated by 90° using a quarter-wave plate in dual pass, so that a polarizing beam splitter plate allows the reflected light to be transmitted onto PMT2. The frequency of the laser transmitter is tuned to match absorption line of the iodine filter. This means that in the iodine cell, the aerosol component of the signal is filtered so that PMT2 only measures the parallel-polarized molecular component P_M^\parallel . Figure 2.12b displays the transmission spectrum of the iodine filter and the molecular backscatter before and after filtering. The signals P_C^\parallel , P_M^\parallel and P^\perp measured by PMT1, PMT2 and PMT3, respectively, have the form shown in Equation 2.2. As stated in Equation 2.3, $\alpha_{mol}(r)$ is directly proportional to $\beta_{mol}(r)$ by the factor of $8\pi/3$ and $\beta_{mol}(r)$ can be calculated from measured temperature and pressure data or from standard atmosphere profiles. This allows to compute the total received signal power P^T from P_C^\parallel and P^\perp . The two-way molecular

transmission along the LOS is given by:

$$\tau_{mol}^2(r) = exp \left[-2 \int_0^r \alpha_{mol}(r') dr' \right], \quad (2.6)$$

where r is the observation range. In the next step P_C^{\parallel} , P_M^{\parallel} and P^T are multiplied by r^2 for range correction and divided by the instrumental constants of the lidar system. Furthermore, they are divided by the known term $\tau_{mol}^2 \beta_{mol}$ to account for molecular extinction and backscatter, yielding the attenuated backscatter ratios R_C^{\parallel} , R_M^{\parallel} and R^T . Next, the two-way aerosol optical depth is computed as follows:

$$\tau_{aer}^2(r) = \frac{R_M^{\parallel}(r) - \kappa_{aer} R_C^{\parallel}(r)}{\kappa_{mol}(r) - \kappa_{aer}}, \quad (2.7)$$

where $\kappa_{mol,aer}$ are the iodine filter transmissions for molecular and aerosol backscatter. Since $R^T(r)$ can be computed from the power measured by PMT1 and PMT3, finally the backscattering ratio is obtained by:

$$R(r) = \frac{R^T(r)}{\tau_{aer}^2(r)} = 1 + \frac{\beta_{aer}^T(r)}{\beta_{mol}^T(r)}. \quad (2.8)$$

In conclusion, the HRSL technique presented in Esselborn et al. 2008 allows to separate the molecular and combined attenuated backscatter signals with an iodine absorption filter. Once the two components are isolated, range and instrumental corrections are applied individually as well as corrections for molecular transmission and backscattering, which can be derived from standard atmosphere profiles. These corrections yield the attenuated backscatter ratio of the molecular and combined components, which are used together with transmission parameters of the iodine filter to compute the aerosol extinction. Lastly, the backscattering ratio is retrieved by dividing attenuated backscatter by aerosol transmission.

2.3 Lidar Signal Detection

The signals captured by lidar receivers are very weak in intensity. The separation of these faint signals from the general background and their amplification to a level that can be measured effectively is challenging. There are mainly two detector types that are regularly used for lidar signal detection, namely photomultiplier tubes (PMTs) and avalanche photodiodes (APDs), both of which exploit the photoelectric effect to convert light into electricity. The APD is regarded as the semiconductor equivalent of the PMT. The focus in this section will lie on PMTs, since the lidar system discussed in this thesis uses one. However, many of the concepts explained in relation to PMTs also apply to APDs.

Avalanche Photodetectors APDs

APDs are a type of highly sensitive photodiode, which are based on a p-n junction (interface of positively doped and negatively doped semiconductor). Photoelectrons created in

the junction's depletion region by means of the photoelectric effect are swept towards the cathode by the built-in electric field of the depletion region, thus creating a photocurrent. APDs are operated by applying a high reverse bias voltage to a semiconductor, like silicon or germanium, which will cause an internal current gain effect due to impact ionization. This is when photoelectrons are accelerated by the applied electric field and gain enough energy to knock other electrons out of their bound state and elevating them to the conduction band. This process repeats itself and leads to an avalanche effect.

Photomultiplier Tubes PMTs

A photomultiplier tube (PMT) is a vacuum tube used to measure the intensity of electromagnetic radiation, by making use of the photoelectric effect and secondary emission. The typical construction of a PMT is illustrated in Figure 2.13.

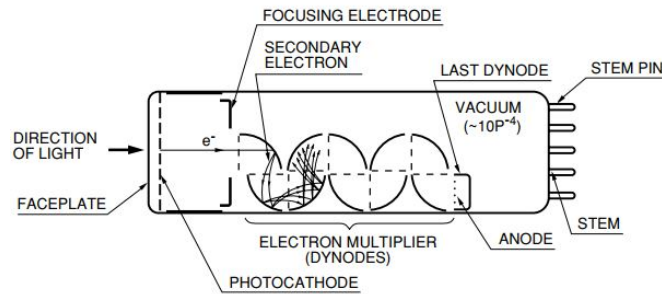


Figure 2.13: Construction of a photomultiplier tube (Hamamatsu-Optics 2017)

Incident photons are absorbed by electrons in the valence band of the photo-cathode. If the energy acquired through the absorption process surpasses the binding energy of the electron, it is likely to be ejected from the material (*Photoelectric effect 2023*). This is called the photoelectric effect. Some electrons immediately re-emit photons through the inverse process called Compton effect and fall back to the valence band. There is a probability with which photo-electrons are definitely ejected from the photo-cathode, which is called quantum efficiency η and is given by (Hamamatsu-Optics 2017):

$$\eta = \frac{hc}{\lambda e} S_k \cdot 100 \%, \quad (2.9)$$

$$\begin{aligned} h &: 6.63 \cdot 10^{-34} \text{ Js,} \\ c &: 3.00 \cdot 10^8 \text{ ms}^{-1}, \\ e &: 1.60 \cdot 10^{-19} \text{ C,} \end{aligned}$$

where h is Planck's constant, c is the speed of light in vacuum and e is the electron charge. S_k is the radiant sensitivity of the photo-cathode material, which is the photocurrent I_k measured at the photo-cathode, divided by the incident radiant flux L_p at the wavelength of interest:

$$S_k = \frac{I_k}{L_p}. \quad (2.10)$$

The photoelectrons are accelerated by a strong electric field towards the focusing electrode and onto the first dynode, where they are multiplied by means of secondary electron emission. This is a process where incident electrons physically transfer kinetic energy to one or more electrons, raising their energy enough to overcome their binding energy, and ejecting them from the material (Kollath 1956). A series of cascaded dynodes causes an amplification of the original electron beam after each stage, resulting in an avalanche effect. The multiplied electrons emitted from the last dynode are finally collected at by the anode. The multiplication factor or gain of a PMT is so large, that a measurable current can be created out of a few incident photons. The secondary emission ratio δ depends on the strength of the accelerating electric field, and is given by (Hamamatsu-Optics 2017):

$$\delta = a \cdot E^k, \quad (2.11)$$

where E is the interstage voltage between the dynodes, a is a constant, and k is determined by the structure and material of the dynode and has a value from 0.7 to 0.8. The gain μ , which is the amplification factor of the photocurrent I_k , is given by the following equation (Hamamatsu-Optics 2017):

$$\mu = \frac{I_p}{I_k} = \alpha \cdot \delta_1 \cdot \delta_2 \cdots \delta_n, \quad (2.12)$$

where I_p is the anode current, α the collection efficiency of the dynodes, and $\delta_{1,2,\dots,n}$ are the secondary emission ratios of the dynode stages 1,2,...,n. Assuming that the PMT is operated with equally distributed voltage dividers for each dynode stage, the gain can be given as a function of the supply voltage U_{HV} by the following equation (Hamamatsu-Optics 2017):

$$\mu = (a \cdot E^k)^n = a^n \left(\frac{U_{HV}}{n+1} \right)^{kn} = A \cdot U_{HV}^{kn}. \quad (2.13)$$

Up to this point only PMTs with a single anode were discussed. However, there exists a variety of multi-anode PMTs, or photo multiplier tube arrays (PMTAs), that contain a 1 or 2-dimensional array of anodes and enable a spatial resolution of the measured light. An application for imaging a 1D signal with a 32-channel PMTA is described in Section 2.2 for the AEROLI DD-DWL.

Current to Voltage Conversion

Both PMTs and APDs output a current which is proportional to the intensity of the incident light. However, to digitize the signal, it must be converted to a voltage first. This may be done with a transimpedance amplifier (TIA). The TIA is implemented with an operational amplifier (OPA) with a feedback resistor R_F connected between the output and the inverting input of the OPA, see Figure 2.14. The feedback resistor C_F is used to improve stability. R_F determines the gain of the TIA:

$$\frac{U_{out}}{I_{in}} = -R_f, \quad (2.14)$$

so

$$U_{out} = -R_f \cdot I_{in}. \quad (2.15)$$

The negative sign at R_f is due to the inverting configuration of the OPA. Once the photocurrent is converted to a voltage signal, it can be digitized using a analog-to-digital converter (ADC).

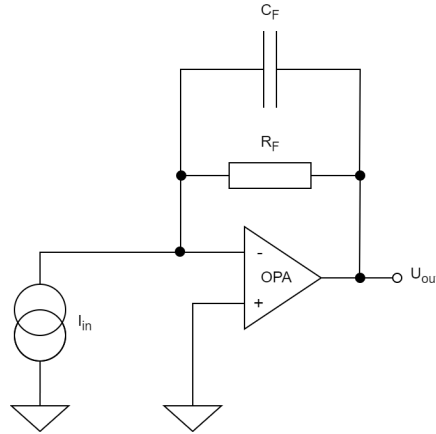


Figure 2.14: Reduced representation of a transimpedance amplifier.

2.4 Control Theory

Control theory is a field in engineering and mathematics dealing with the control of dynamic systems. Roughly speaking, the goal is to develop a model or algorithm which modifies the values of one or more system inputs to drive the system output to a desired state ([Control theory 2023](#)). It is an optimization problem to achieve the desired system state while minimizing delay, overshoot and steady state error and ensuring a level of control stability. The general feedback control scenario is represented as a block diagram in Figure 2.15. The target r is the desired system output, which is compared with a measurement of the real system output y . This configuration is called feedback control, since the system output is fed back to the input of the controller. The task of the controller is to derive a control signal u so that the difference e approaches zero for subsequent loop repetitions.

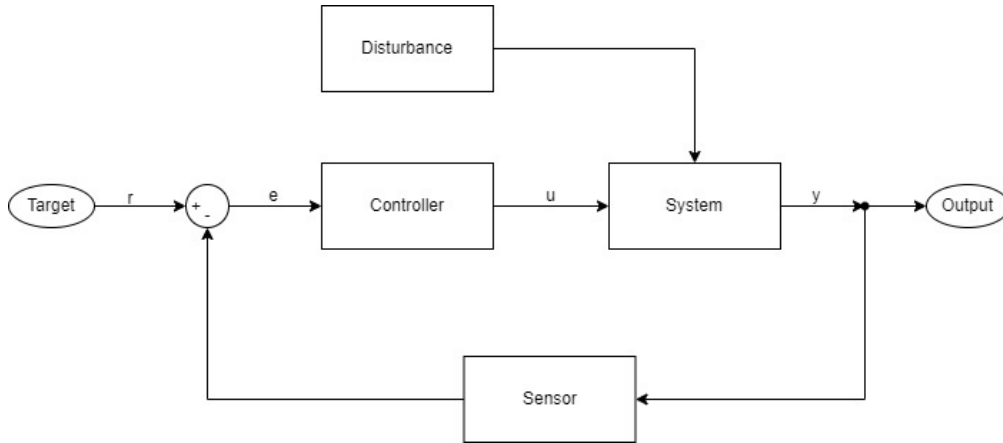


Figure 2.15: General feedback control problem.

The system, or plant, as often called in control theory, reacts to a change of the control signal in a way which is intrinsic to the physical nature of the system. The mathematical interpretation of the input/output behavior of a linear time-invariant system (LTI) is called transfer function (TF). Most systems are non-linear, but LTI theory can be assumed in many cases, when the system is operated within certain parameters. To formulate the transfer function of a system, first the Laplace transforms of the continuous-time input and output signals are formed and then the ratio is computed

$$H(s) = \frac{Y(s)}{U(s)} = \frac{\mathcal{L}\{y(t)\}}{\mathcal{L}\{u(t)\}} \quad (2.16)$$

where $H(s)$ is the transfer function, $u(t)$ the input and $y(t)$ the output signal and \mathcal{L} the Laplace transform. In classical control theory, $H(s)$ is often characterized by measuring the unit-step response of the system. In this way, $H(s)$ can be identified, even though the system is unknown. In the physical world, many processes follow the behaviour of first-order LTI systems, for example the decay of radioactive material, or the charging of an electric capacitor. These processes are described by an exponential development of their state in time. In the time domain, the charging of a capacitor is mathematically described by:

$$V_C(t) = V \left[1 - \exp\left(-\frac{t}{RC}\right) \right], \quad (2.17)$$

where $V_C(t)$ is the voltage across the capacitor, R is the load resistance and V is the applied voltage. The product RC is commonly denoted as τ and is the time constant of the system. Physically, τ is the time elapsed until the system reached $1 - 1/e \approx 63.2\%$ of the final output value. To fit the control theory terminology, Equation 2.17 is rewritten:

$$y(t) = y_{final} \left[1 - \exp\left(-\frac{t}{\tau}\right) \right], \quad (2.18)$$

yielding the following expression in the frequency domain:

$$H(s) = \frac{K}{s + 1/\tau}, \quad (2.19)$$

where K is the system gain. Many other processes in nature can be modelled by second order systems. One example is the mass-spring-damper model shown Figure 2.16. The equation of motion for a friction less surface is given by:

$$m\ddot{y} + c\dot{y} + ky = y(t), \quad (2.20)$$

where m is the mass, $y(t)$ is the position of the mass, c is the damping constant and k is the spring constant. The solution of this differential equation can be found in the time-domain by means of the Laplace transform:

$$H(s) = \frac{K}{ms^2 + cs + k}, \quad (2.21)$$

or in the form:

$$H(s) = \frac{K\omega_0^2}{s^2 + 2\zeta\omega_0s + \omega_0^2}, \quad (2.22)$$

where K again is the system gain and ω_0 is the natural frequency of the system, given by:

$$\omega_0 = \sqrt{\frac{k}{m}}, \quad (2.23)$$

and ζ the damping factor:

$$\zeta = \frac{1}{2\omega_0} \frac{c}{m}. \quad (2.24)$$

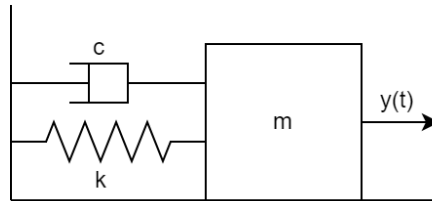


Figure 2.16: Mass-damper-spring model.

The simplest way to characterize a system is by determining its unity step response, e.g. by measuring the system output for a given input step. If the physical nature of the model is known, the solution to the differential equation describing the system can be found analytically, as shown above for the mass-spring-damper model. With the solution of the differential equation, any response of the system can be computed. Figure 2.17 shows the step responses of a first-order (PT1) and second-order system (PT2) with the transfer functions

$$H_{PT1}(s) = \frac{1}{s + 1} \quad (2.25)$$

and

$$H_{PT2}(s) = \frac{1}{s^2 + s + 1}. \quad (2.26)$$

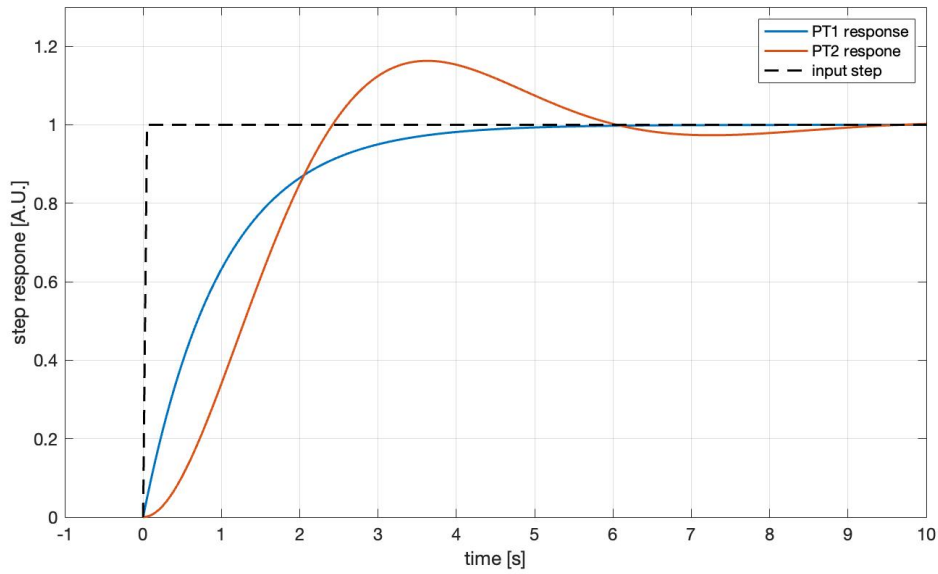


Figure 2.17: Unit-step response of a first-order (PT1) and second-order system (PT2).

If the physical nature of the system at hand is not completely understood, a grey-box approach can be chosen to determine the transfer function. To do so, a given input (could be a step or anything else) is applied to the system and both input and output are recorded. With these data, algorithms can be used to fit a transfer function to the measurement data. For this, the number of zeros and poles has to be specified. This means that a basic understanding of the system is required, hence grey-box approach. Software like MATLAB offer functions for this task. More details on this topic can be found in Chapter 5.

To ensure the desired output of a plant, a controller is needed. Various controller tech-

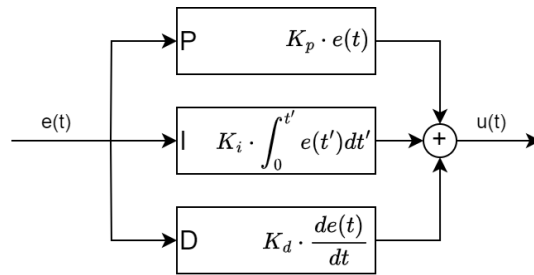


Figure 2.18: Block diagram of a PID controller.

niques exist, where the simplest one is the rule-based controller. It consist of a series of if/else statements which inspect whether a number of predefined rules are fulfilled. These rules are formulated from expert knowledge and experience and specify corrective actions of the controller for a given state. The most widely used type of controller is the proportional-integrating-derivative (PID) controller. Like most controllers, the PID controller is typically

used in a feedback configuration, meaning that the system output is fed back so that the corrective measure is executed in the next loop iteration (see Figure 2.15). The PID controller sets the desired system output, or set point, by driving the output error e to zero with three branches, namely the P, I, and D branch, as shown in Figure 2.18. The controller is tuned by setting the controller gain constants. The proportional gain K_p determines how aggressively the controller reacts to an output error, the integrating gain K_i reduces the steady-state error, and the derivative gain K_d dampens oscillations of the output. The tuning of the controller gains is commonly the greatest challenge in designing the controller, since no analytic method to solve this task exists. Oftentimes the desired controller behaviour is achieved by a trial-and-error or an empirical approach. However, there exists one heuristic tuning method widely used in PID control named the Ziegler-Nichols Method. The procedure starts by setting all the gains to zero and then gradually increasing K_p until the system output starts to oscillate and then even further until the oscillation stabilizes. The proportional gain needed to obtain the sustained oscillation is named ultimate gain K_u and the oscillation period is denoted as T_u . With these parameters, the optimal controller gains are set according to Table 2.1.

Table 2.1: Optimal gain settings following the Ziegler-Nichols method (*Ziegler-Nichols method 2023*).

Control Type	K_p	K_i	K_d
P	$0.5K_u$	-	-
PI	$0.45K_u$	$0.54K_u/T_u$	-
PD	$0.8K_u$	-	$0.10K_uT_u$
PID	$0.6K_u$	$1.2K_u/T_u$	$0.075K_uT_u$

2.5 Turbulence and Power-Law Scaling

Turbulence in fluid dynamics occurs, when the relation between flow velocity and fluid viscosity exceeds a critical value. The previously well directed (laminar) flow becomes chaotic and variations in the velocity vector occur (*Turbulence 2023*), giving rise to turbulent eddies. Large eddies are unstable and eventually break up into smaller eddies containing parts of the energy of the initial eddy. This process repeats itself again and again for the smaller eddies, resulting in a down-scaling cascade. The energy is transferred down to the smaller scales until the length scale is sufficiently small, so that the viscosity of the fluid can effectively dissipate the kinetic energy into heat (*Turbulence 2023*). In the atmosphere, mostly large-scale factors increase shear and create unstable conditions which favor the formation of eddies. This means that the turbulence which is felt by aircraft as bumpiness is owed to the injection of energy at large scales, which works its way down to aircraft scales (Sharman and Lane 2016). There is a range of scales commonly called the inertial sub-range, where the spectrum of eddy kinetic energy was found to fall off as $k^{-5/3}$, where k is the horizontal wavenumber ($2\pi/\text{wavelength}$) (Sharman and Lane 2016). The theory for this phenomenon was first introduced by the Russian mathematician Andrey Nikolaevich Kol-

mogorov, who hypothesized that for very high Reynolds number and for scales in the inertial range, the turbulent motions in the fluid become statistically isotropic. Another hypothesis of Kolmogorov states that at very high Reynolds number, the statistics of scales in the inertial range are universally and uniquely determined by the scale and the rate of energy dissipation (Kolmogorov 1991). This last hypothesis is described by the energy spectrum function (Sharman and Lane 2016):

$$S_u(k) = C_k \epsilon^{\frac{2}{3}} k^{-\frac{5}{3}} \quad (2.27)$$

where C_k is the Kolmogorov constant equal to 0.5–0.6, ϵ is the energy dissipation rate and k the horizontal wave number. Any spatially or temporally distributed field, which fulfils Equation 2.27 is said to be statistically scale invariant, or with other words, to exhibit scaling (Pressel and Collins 2012). The statistical scale invariance of many atmospheric variables has been well established in the literature. Nastrom and Gage 1985 found that upper-tropospheric wavenumber spectra of wind temperature have a power-law scaling exponent of $-5/3$ within the mesoscale (< 400 km). The property of scale invariance has also been observed on many particles embedded in the turbulent flow of the atmosphere, like water vapor (Nastrom and Gage 1985), trace gases (Cho, Newell, and Barrick 1999), aerosols (Gutleben and Groß 2021) and cirrus crystals (Wang and Sassen 2006, Demoz et al. 1998). Wang and Sassen 2006 found spectral slopes close to $-5/3$ derived from lidar-return measurements and mean radar Doppler velocity data collected from the base region of cirrus clouds. They deduce that energy injected to the cloud base by buoyancy cascades from the large- to small-scale motions, bringing about the signature $k^{-5/3}$ attributed to Kolmogorov turbulence. Demoz et al. analyzed vertical air velocity observations obtained from the NASA DC-8 on 21 April 1996 and found slopes of $-5/3$ in the power spectra of the observations for small scales and slopes close to -3 for scales from 2-20 km.

Atmospheric turbulent processes don't always behave according to the Kolmogorov model. In fact, deviations of atmospheric optical turbulence behavior from the Kolmogorov model have been examined extensively over the last few decades (Zilberman et al. 2008 and references therein). Zilberman et al. 2008 argue that the Kolmogorov model, given in Equation 2.27, constitutes only a part of a more general behavior of energy transfer across scales in a turbulent flow, and that deviations arise at altitudes above 5.5–6 km.

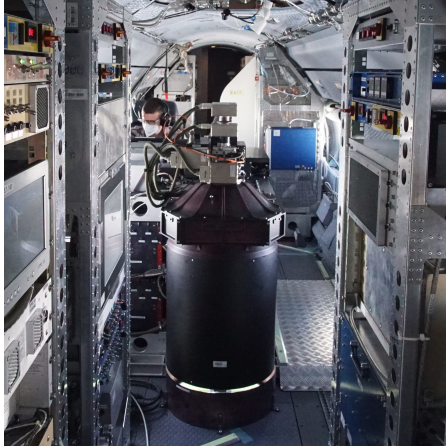
2.6 Power Spectral Density PSD

The power spectral density (PSD) is a mathematical tool describing how the power of a continuous time signal is distributed over its frequency components. For abstract signals, the power is identified as the square of the signal. The average power of a signal $x(t)$ over a time span T is given by:

$$\bar{P} = \frac{1}{T} \int_{-T/2}^{+T/2} |x(t)|^2 dt. \quad (2.28)$$

The PSD may be obtained by:

$$S_{xx}(f) = \frac{1}{T} |\hat{x}(t)|^2. \quad (2.29)$$



(a) WALEs lidar installed in the HALO aircraft (DLR 2023b).



(b) DLRs High Altitude and LOng-range research aircraft HALO (DLR 2016)

$\hat{x}(t)$ is the Fourier transform of the convolution of $x^*(-t)$ with $x(t)$, where $*$ is the complex conjugate:

$$\hat{x}(t) = \mathcal{F}\{x^*(-t) * x(t)\} = \int_{-\infty}^{+\infty} \left[\int_{-\infty}^{+\infty} x^*(t-t')x(t)dt \right] e^{-2\pi ft'} dt'. \quad (2.30)$$

Equation 2.29 is valid for untruncated random processes, where $T \rightarrow \infty$. For time limited, discrete-time signals, the PSD can be estimated with the fast Fourier transform (FFT). The FFT is an algorithm to compute the Fourier transform of discrete time signals (DFT) (Heideman, Johnson, and Burrus 1985).

2.7 WALEs, Cirrus-HL and HALO-AC3

WALEs stands for Water Vapor lidar Experiment in Space and is a DLR project for the preparation of a space-borne mission to map the global water vapour distribution. It shall do so with a H₂O-Differential Absorption lidar (DIAL) capable of delivering global water vapour observations suitable for a reliable assessment of its temporal and spatial evolution. Such analyses have the potential to enhance the understanding of climate processes in general circulation models and improve numerical weather prediction. Part of the WALEs project is the development of an air-borne demonstrator for the validation of the H₂O-DIAL measurement concept (M. Wirth et al. 2009). Although the main objective of the air-borne lidar is to measure water vapor profiles, it is also equipped with additional aerosol channels at 532 nm and 1064 nm with depolarization. WALEs uses a high-spectral resolution technique (explained in Section 2.2), which distinguishes molecular from particle backscatter, to make direct extinction measurements (Esselborn et al. 2008). With the WALEs lidar, multiple flight campaigns were performed. Two of those (Cirrus-HL and HALO-AC3) will be presented in the following, as their data are used for the study of cirrus backscatter variability in Chapter 3.

Cirrus in High Latitudes (Cirrus-HL)

The CIRRUS-HL initiative constitutes a collaborative atmospheric research endeavor involving German research institutions and universities. The campaign is carried out with the air-borne scientific platform HALO (Gulfstream G55) in conjunction with satellites and models to acquire new insights on nucleation, properties of ice clouds in high latitudes and their climate impact. This specific region corresponds to one of the areas on Earth experiencing the most significant anthropogenic rise in surface temperatures. The study aims to investigate the influence of aviation on clouds and the impact of contrails on climate through airborne observations conducted over Central Europe and the North Atlantic flight corridor (DLR 2023a). A total of 19 state-of-the-art in-situ and remote sensing instruments are deployed to study the processes of nucleation, life cycle, and radiative impact associated with ice clouds and anthropogenic contrail cirrus. Most of the instruments are in-situ, measuring properties like aerosol chemical composition, size distribution of cloud particles and aerosols, water vapor content, trace gas concentrations, and meteorologic parameters like temperature, pressure and 3-D wind vector. Remote sensing instruments like a radiometer, an albedometer and a hyperspectral imager are used to measure radiation fluxes, radiances and irradiances in multiple wave lengths. The WALES air-borne lidar is employed to measure water-vapor mixing ratio and aerosol backscatter and extinction profiles. 23 flights were accomplished over central Europe including overpasses, underpasses and in-situ flights of cirrus clouds and con-trails. Figure 2.20 shows the tracks flown during the campaign period.

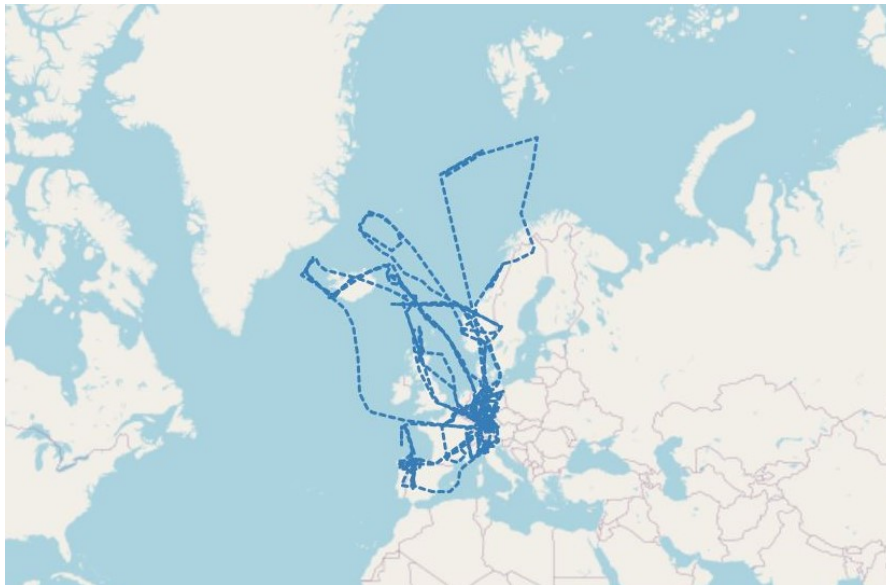


Figure 2.20: Tracks flown during the Cirrus-HL campaign (DLR 2023b).

HALO-AC3

The HALO-AC3 flight campaign is a research collaboration between various German universities and research institutes aiming to study air-mass transformations and major atmospheric and surface processes and feedback mechanisms in the Arctic to gain a better understanding of the Arctic amplification. This phenomenon manifests as a twice as rapid climate warming in polar regions as a consequence of interlinked positive feedback processes specific to the Arctic. Arctic amplification might influence the jet streams, resulting in stronger undulations of Rossby waves. As a consequence, more warm and moist air intrusions cold air outbreaks might occur, the first of which could increase water vapour and clouds in the winter-time by 70 % and 30 %, respectively. As a result, a higher local green house effect is expected heating the near-surface air. This would promote the reduction of surface reflectivity (albedo) due to melting ice, which leads to more surface warming and again more ice melting. To improve the representation of these effects in models, quasi-Lagrange observations of air-mass transformation processes are performed. The observational strategy involved three different research aircraft flying at different altitudes taking in-situ and remote measurements. The HALO aircraft, flying at an altitude of up to 15 km, performs measurements of the complete vertical tropospheric air-mass column, including meteorological quantities, turbulence parameters, water vapour, aerosol particles, and clouds. To do so, it is equipped with different passive and active remote sensing instruments, among others the WALES lidar mentioned above, and dropsondes. Additionally, two further low-flying aircraft (below 3-5 km altitude) funded by the Alfred Wegener Institute Helmholtz Centre for Polar and Marine Research (AWI) are deployed. The research aircraft Polar 5 performs active and passive remote sensing measurements and Polar 6 records in-situ data of clouds, aerosol particles, and radiative processes. The observation scheme is illustrated in Figure 2.21 and Figure 2.22 shows the tracks flown during the campaign period.

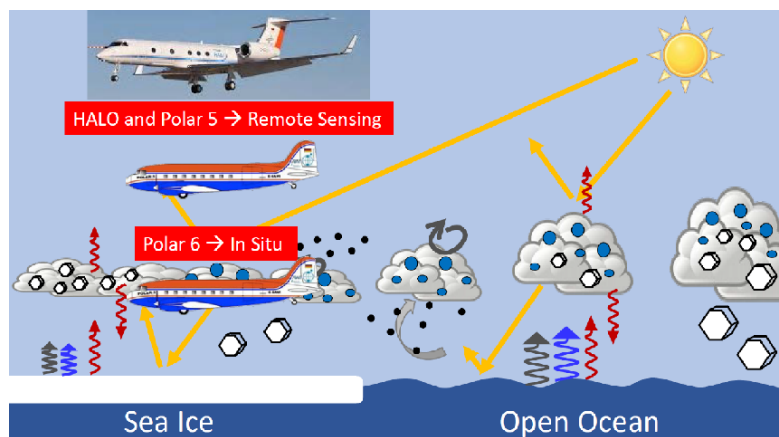


Figure 2.21: Scheme of collocation of DLR-HALO with AWI-Polar 5 and Polar 6 aircraft, as planned for HALO-AC3 (Leipzig 2023)

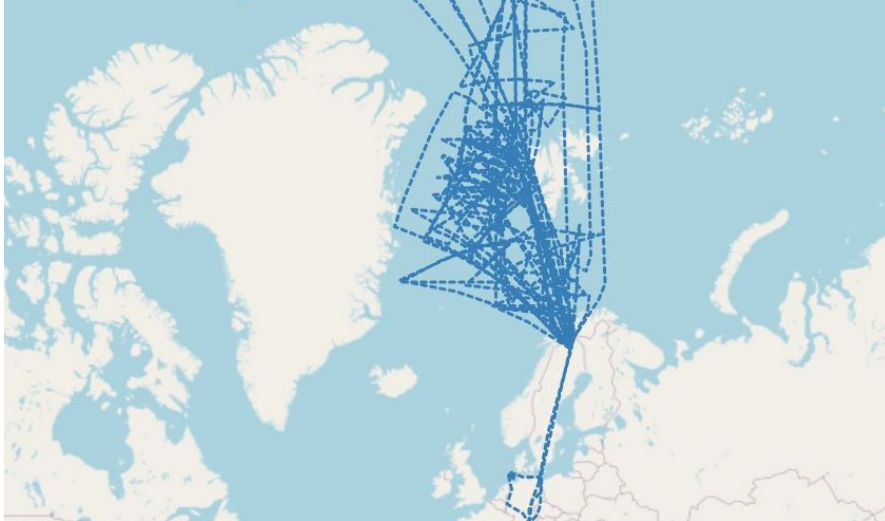


Figure 2.22: Tracks flown during the HALO-AC3 campaign (DLR [2023c](#))

Chapter 3

Horizontal Variability of Cirrus Clouds

Spaceborne, or airborne lidar systems allow to scan the atmosphere and retrieve two-dimensional profiles, which enable to image of vertical and horizontal distribution of the observed quantity. With such data, spectral methods can be used to investigate the variability of atmospheric parameters for different spatial scales. As stated in Chapter 1.3, the power spectrum and probability density function are computed from observational data in order to estimate the expected horizontal backscatter variability in cirrus clouds with respect to spatial frequency distribution and magnitude. For the study presented in the following, data from the flight campaigns Cirrus-HL and HALO-AC3 were chosen, because they were carried out at northern latitudes where there is a concentration in air traffic. Observations from this area, the major transatlantic flight corridor, are representative for the operating conditions for which the AGC presented in this thesis is designed.

Before the flight data are analysed, reference atmospheric parameters and instrumental specifications from the AEROLI lidar are used to estimate the differences in magnitude of attenuated backscatter measurements it would experience at flight altitude. This shall serve as a reference to the values resulting from the investigation of the flight data. The instrumental parameters of the AEROLI lidar system from Vrancken and Herbst 2022 are as follows ¹:

Table 3.1: Instrumental parameters of the AEROLI DWL (Vrancken and Herbst 2022.)

Laser wavelength λ	355 nm
Transmitted signal power P_0	8 W
Overall optical efficiency $k_T \cdot k_R$	0.2
Sampling frequency $1/\tau$	31.25 MHz
Telescope surface area A	0.11 m ²

Determining the overlap function is no trivial task. For the AEROLI receiver, the geometric function was derived from a model created with the ZEMAX raytracing software (Herbst 2019). The dashed line in Figure 3.1 shows the overlap function resulting from the ray tracing model. $G(r)$ plateaus at roughly 0.88, which is due to the obstruction ratio $O.R.$ of 12 % from the secondary mirror of the Newtonian telescope. The general shape of a lidar signal is dominated by the product of the $1/r^2$ factor (dotted line) and the overlap function. Next, a synthetic lidar signal is computed by inserting reference values for the atmospheric

¹schematics in Figure 2.9

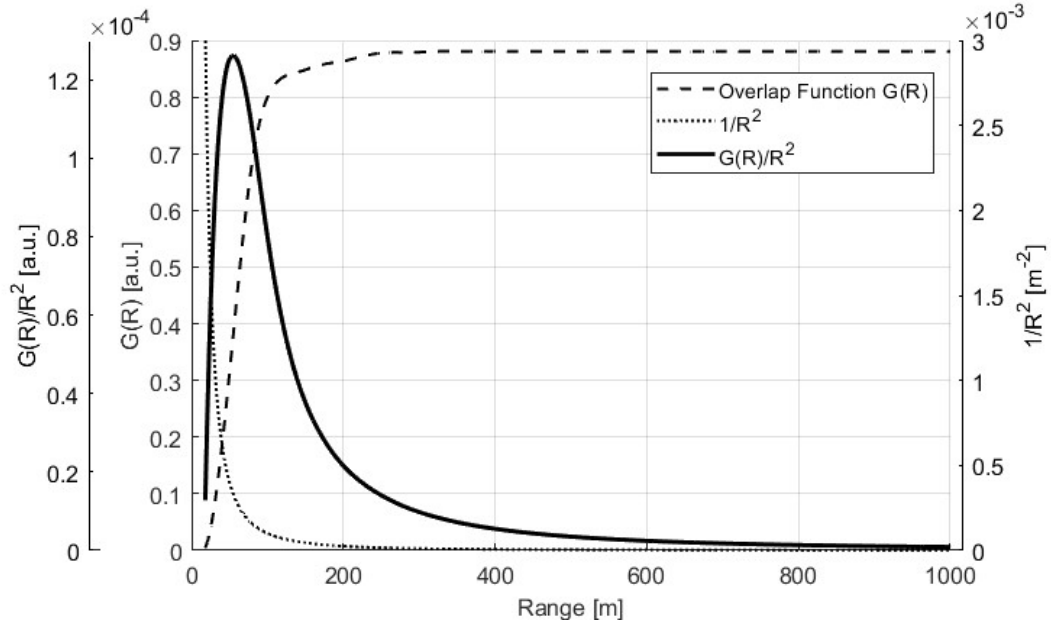


Figure 3.1: Dashed line: overlap function of the AEROLI receiver, dotted line: $1/r^2$ factor, solid line: product of the overlap function and the $1/r^2$.

parameters β (backscattering coefficient) and α (extinction coefficient) into the lidar equation (Equation 2.2). The aim is to compare the signal level resulting from a clear sky with the signal level from when a cirrus cloud is ahead of the aircraft. In clear sky conditions at cruising flight altitudes, molecular backscattering dominates. According to global aerosol models, such as ESA Reference Model for the Atmosphere (RMA) (Vaughan et al. 1998) or LIVAS (Amiridis et al. 2015), the molecular backscattering coefficient $\beta(z, \lambda)$ is a function of altitude z and wavelength λ and can be computed for arbitrary values of z and λ with:

$$\beta_{mol}(z, \lambda) = 1.010^{-7} \left(\frac{\lambda_0}{\lambda} \right)^4 \exp\left(-\frac{z}{z_{mol}}\right) [m^{-1}sr^{-1}] \quad (3.1)$$

where λ_0 is the reference wavelength of $1.06 \mu m$ and z_{mol} is the reference altitude at 8000 m. The backscattering coefficient scales for λ and z with two different mechanisms. The first comes from Rayleigh scattering being reciprocally proportional to the fourth power of the wavelength. The second scaling mechanism is owed to molecular backscattering being directly proportional to atmospheric density, which decreases exponentially with altitude according to the barometric formula. The values for β_{mol} and α_{mol} for a lidar with a wavelength of 355 nm operated at an altitude of 9000 m, are computed with Equation 3.1 and Equation 2.3 respectively and can be found in Table 3.2. Typical values for backscattering and extinction coefficients of cirrus clouds given for altitudes between 8500 m and 9500 m are taken from the ESA RMA (Vaughan et al. 1998), see Table 3.2. Inserting instrumental and atmospheric parameters for both clear sky conditions and cirrus cloud cover into Equation 2.2, yields the range dependent lidar signals illustrated in Figure 3.2.

One can observe a ratio of roughly 50 regarding the peak return signal power from inside a cirrus cloud \hat{P}_{cirrus} and the peak clear air return signal \hat{P}_{mol} .

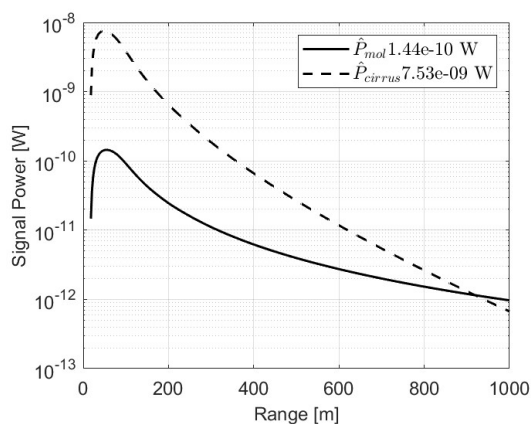


Figure 3.2: Synthetic lidar signals from clear sky and cirrus return, computed with Equation 2.2

Table 3.2: Top of table: Variables used to compute the synthetic lidar signals P_{mol} and P_{cirrus} . Bottom of table: Peak values of and the ratio of P_{mol} and P_{cirrus} .

Variable	value
β_{mol}	$2.61 \cdot 10^{-6} m^{-1} sr^{-1}$
α_{mol}	$1.93 \cdot 10^{-5} m^{-1}$
β_{cirrus}	$1.6 \cdot 10^{-4} m^{-1} sr^{-1}$
α_{cirrus}	$2.3 \cdot 10^{-3} m^{-1}$
\hat{P}_{mol}	$1.44 \cdot 10^{-10} W$
\hat{P}_{cirrus}	$7.53 \cdot 10^{-9} W$
$\hat{P}_{cirrus}/\hat{P}_{mol}$	52.14

In the following paragraphs, an explanation of the data and metadata of the backscattering ratio (R or BSR) products studied in this chapter is given. Furthermore, the process of selecting suitable data for the investigation is described.

The backscatter ratio (see Equation 2.8) is an insightful variable, since it contains both molecular backscattering and backscattering due to particles, like aerosols or hydrometeors. R indicates how much more light is scattered back from particles, as opposed to pure molecular air. According to Equation 2.8, clouds may be identified for values of R larger than one. The BSR products are computed from airborne lidar observations with the WALES lidar, which operates at 532 nm wavelength for HSRL extinction measurements. This wavelength is generated by frequency doubling of a Nd:YAG solid state laser and is often chosen because it coincides with the absorption lines of the Iodine I_2 used for the HSRL measurement technique. The retrieval of backscattering ratio from aerosol extinction measurements is explained in Chapter 2, Section 2.2. The airborne observations are carried out with a nadir-looking geometry to record vertical profiles. For each measurement flight, one NetCDF file is compiled, containing the data variables listed in Table 3.3. The number density N refers to the number of molecules promoting Rayleigh scattering, i.e. air molecules. Meteorological data like air pressure and temperature are obtained by spatially and temporally interpolating operational analysis and short-term forecast fields from the atmospheric high-resolution model (HRES), provided by the European Centre for Medium-Range Weather Forecasts (ECMWF), to the observation location and time. The ECMWF operational analysis and forecast data were retrieved from the ECMWF Meteorological Archival and Retrieval System (MARS) (Society 2023). For details about the data and interpolation, refer to Schäfler et al. 2020. The molecular backscatter cross section in Table 3.3 was interpolated from data given

Table 3.3: Data variables of backscattering ratio products.

Variable	value	Unit	Dimensions
time	-	s	time
time resolution	-	s	time
height above sea level	-	m	time
latitude	-	degrees north	time
longitude	-	degrees east	time
altitude	-	m	range
range	-	m	range
range resolution	-	m	range,time
emission wavelength λ_{TX}	532	nm	-
backscattering ratio $R(\lambda_{TX})$	-	-	range,time
molecular backscatter cross section σ_{mol}	$6.246 \cdot 10^{-32}$	m^2/sr	-
temperature	-	K	range,time
number density of air N	-	m^{-3}	range,time

in Bodhaine et al. 1999. Figure 3.3 shows the HRSL backscattering data from flight #18 of the Cirrus-HL campaign in a altitude-distance plot (upper plot) and the corresponding flight track (bottom plot). Note that the blank spaces in the upper plot of Figure 3.3 are empty data points. The data products are averaged to time resolution of one second, which at flight speeds of 200 m/s - 250 m/s correspond to spatial resolutions of 200 m - 250 m. As the horizontal slices of the data shall be interpreted in terms of spatial scales (wave number k), instead of temporal scales, the time dimension of the data is converted to a spatial dimension henceforth referred to as *trajectory*. The trajectory is computed from the haversine distance between successive GPS coordinate points. The formula gives the distance between two points on the great circle of a sphere:

$$2r \cdot \arcsin \left(\sqrt{\sin^2 \left(\frac{\phi_2 - \phi_1}{2} \right) + \cos\phi_1 \cdot \cos\phi_2 \cdot \sin^2 \left(\frac{\lambda_2 - \lambda_1}{2} \right)} \right), \quad (3.2)$$

where λ is the longitude² and ϕ is the latitude and the subscripts ₁ and ₂ represent the first and the second point along the flight track respectively. Due to the irregular flight velocity of the aircraft, the computed trajectory dimension is not evenly sampled. This issue will be addressed later in this chapter.

Not all data collected during the individual measurement flights are suitable for the investigations outlined in this chapter. In order to extract meaningful data, scenes are selected according to the following criteria:

1. No gaps/jumps in time.
2. Straight flight tracks only (no flight maneuvers) at constant flight altitude.
3. Contain mostly clouds or are within a cloud.

²Not to be confused with λ for wavelength.

4. Altitudes between 6 to 11 km.

1. is to avoid artifacts in the Fourier transform due to a non-uniform time vector, 2. is to ensure only straight, horizontal slices of the data are used, 3. is a measure to avoid that the signal from clear air dominates the data profiles and 4. is to represent the typical cruise flight altitudes.

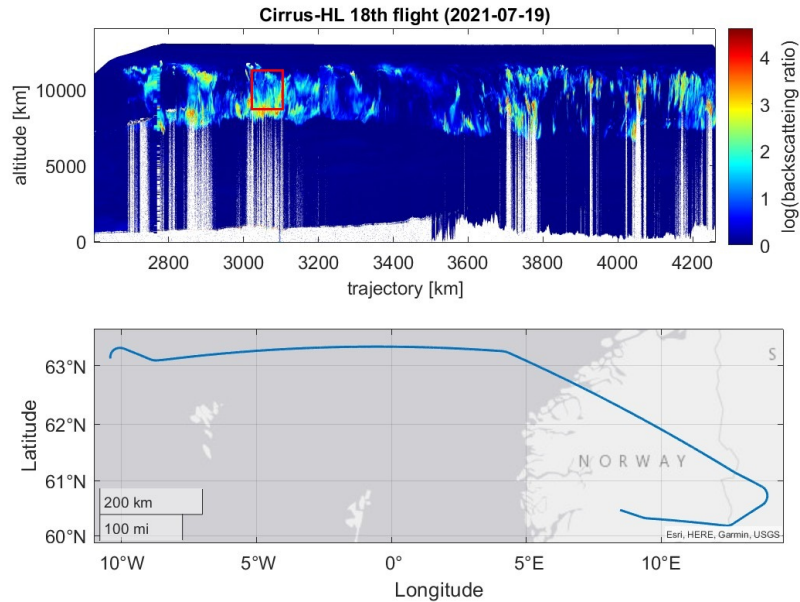


Figure 3.3: Data from the Cirrus-HL flight #18. Top: altitude-distance plot of the HSRL backscattering ratio in logarithmic scale. The red square marks the scene depicted in Figure 3.4. Bottom: flight track.

Figure 3.4 displays a zoomed-in section indicated by the red square in Figure 3.3 and represents a scene which fulfills the criteria described above. A total of 68 scenes of 2D-profiles from 16 measurement flights were selected in this way for the analysis to come in the following paragraphs. 20 of the scenes originated from the Cirrus-HL campaign and 47 from the HALO-AC3 campaign (Table 3.4).

Table 3.4: Origin of data.

campaign	#Flights	#Scenes
Cirrus-HL	10	21
HALO-AC3	6	47

The data provided by the WALES lidar was measured at 532 nm wavelength, but the AEROLI lidar operates at 355 nm. To obtain data representative for the AEROLI lidar system, the BSR data products are scaled to the 355 nm wavelength. Table 3.5 demonstrates how to compute the backscattering ratio R , the backscattering coefficient β and the extinction

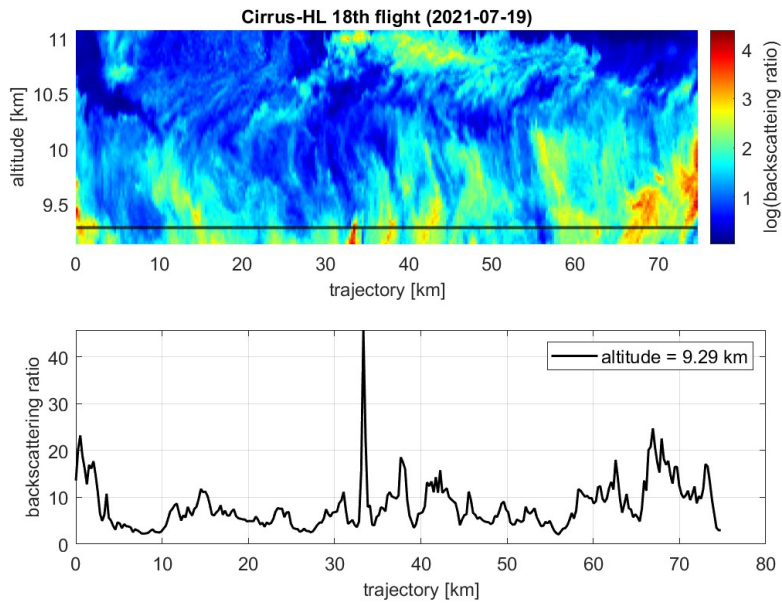


Figure 3.4: Selected scene from flight #18 of Cirrus-HL. Top: altitude-distance plot of the HSRL backscattering ratio in logarithmic scale. Bottom: horizontal profile of the HSRL backscatter ratio at 10 km altitude.

coefficient α at 355 nm from 532 nm observations of R . The molecular backscattering coef-

Table 3.5: Origin of data.

step	variable obtained	Equation used
1.)	$\beta_{mol}(532nm)$	$\sigma_{mol} \cdot N(z)$
2.)	$\beta_{mol}(355nm)$	Equation 3.1
3.)	β_{aer}	Equation 2.8
4.)	$\beta(355nm)$	Equation 2.8
5.)	$R(355nm)$	Equation 2.8
6.)	$\alpha_{mol}(355nm)$	Equation 2.3
7.)	α_{aer}	$k \cdot \beta_{aer}$
8.)	$\alpha(355nm)$	$\alpha_{mol}(355nm) + \alpha_{aer}$

ficients at 532 nm is computed with the values for the molecular backscattering cross section σ_{mol} and the number density of air $N(z)$ contained in the BSR data product. $\beta_{mol}(355nm)$ is obtained by means of wavelength scaling as described in Equation 3.1. Computations of β_{aer} , $\beta(355nm)$ and $R(355nm)$ are done with Equation 2.8. The difference in the backscattering coefficients at 532 nm and 355 nm is assumed negligible in this part. With the well established model for the molecular lidar ratio in Equation 2.3, $\alpha_{mol}(355nm)$ is computed. The lidar ratio for Mie scattering k in cirrus clouds is assumed constant. In Section 2.2,

different values presented in the literature were cited, which range from 14 to 24. Here a value of 20 is used for k . Lastly, the extinction coefficient at 355 nm $\alpha(355nm)$ is computed as the sum of the molecular and aerosol extinction coefficients. $\alpha(355nm)$ and $\beta(355nm)$ are used later in this chapter to compute synthetic lidar signals according to Equation 2.2.

3.1 Spectral Analysis

The lidar system for which the AGC shall be designed, is used for turbulence detection in aviation-relevant scales. This means that the measurement range is 50 m - 300 m ahead of the aircraft. Dominant structures found in the backscattering ratio products for this length scales, may provide a reference for the formulation of functional requirements for the AGC. However, the interpretation of scales in the near field is limited due to the horizontal resolution of 200 m - 250 m. According to the Nyquist-shannon sampling theorem, only structures above $2 \times (200 \text{ m to } 250 \text{ m})$ can be resolved with the given data.

To find any dominant structures, the distribution of the signal power over the frequency space of horizontal backscattering ratio profiles will be investigated. For this, the power spectral density (PSD) of the individual horizontal profiles is computed based on the fast Fourier transform FFT (see Section 2.6). The PSD $S_{i,j}(k)$ for every altitude level i of each scene j of the BSR data is computed, and then averaged along the altitude dimension. The resulting average spectrum of each scene $S_j(k)$ is inspected individually. To get a representation of the mean spectral composition of the cirrus clouds contained in the available data, the spectra of the individual scenes are averaged once again to give the total power spectrum $S(k)$. For the calculation of each $S_{i,j}(k)$ and the total $S(k)$, two points need to be considered, which are addressed in the following.

Point 1: Variable length of scenes

In order to compute the total average spectrum $S(k)$, the dimensions of the individual $S_j(k)$ must be the same. However, this is not the case, since the scenes have different sizes in the trajectory dimension. This issue is mitigated by padding the data arrays with zeros to match the size of the longest scene in the collection before computing the FFT. This procedure does not influence the result of the FFT, but only increases number of frequency bins of the result. This is a consequence of the definition of the frequency vector f used for the FFT:

$$f = 0, 1 \cdot \frac{f_{smp}}{2n}, 2 \cdot \frac{f_{smp}}{2n}, \dots, n \cdot \frac{f_{smp}}{2n} \quad (3.3)$$

Point 2: Non-uniformly sampled data

As indicated by the k in $S_{i,j}(k)$, the PSD is computed w.r.t. the wavenumber instead of the frequency in order to facilitate the interpretation of the data. k is computed from the frequency vector f as follows:

$$k = \frac{2\pi}{\lambda} = 2\pi \cdot \frac{f}{v}, \quad (3.4)$$

where λ is the wavelength and \bar{v} the average flight velocity of the HALO aircraft. \bar{v} varies for different BSR scenes, as the flight speed is not precisely the same for every flight. Naturally, the speed of the aircraft fluctuates throughout the individual flights as well, which means that the BSR observations are non-uniformly sampled w.r.t. the trajectory dimension, as illustrated in Figure 3.5. The variations in flight speed within the individual scenes is typically below 1 % of the average flight speed. Across all scenes, the typical variability in mean flight speed is more than 6 % (see Table 7.2, in the Appendix).

To obtain the same k vector for every $S_j(k)$, all the data can be resampled to a fixed spatial sampling distance $dRTarget$. However, with this procedure implausible features arise in the computed spectra. Since the variation in flight speed is sufficiently small, the resampling procedure is omitted and $S(k)$ is computed without any further processing of the data.

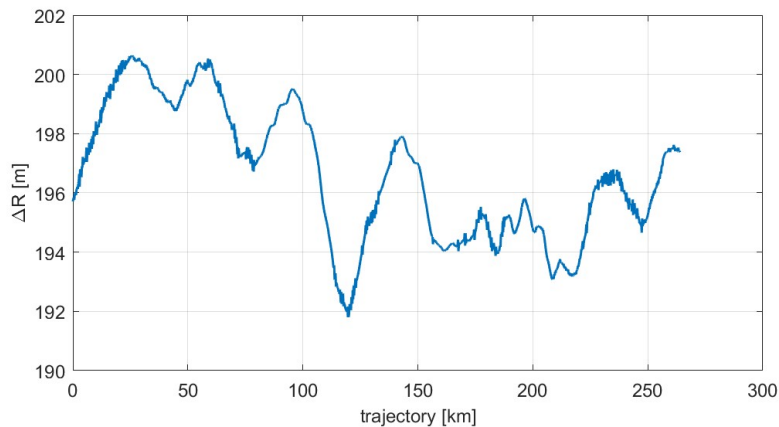


Figure 3.5: Distance travelled between successive location points ΔR along the flight trajectory sampled at 1 Hz. Exemplary data from flight #18 of the Cirrus-HL campaign.

The data processing is carried out in two nested FOR loops. The outer loop iterates through the selected two-dimensional (altitude, aircraft trajectory) BSR scenes and performs zero-padding on the data arrays. The inner loop iterates through the altitude levels of the data. If a data gap is detected in the horizontal slice of the BSR data, that altitude level is excluded from further analysis³. Data gaps can occur due to over-saturation of the lidar instrument and are represented as not-a-number (NaN) values. The pseudo code section 7 in Appendix 7, illustrates how the procedures explained above are implemented.

Results

The averaged spectra resulting from applying the processing steps explained above, display different characteristics from case to case. Figure 3.6 displays the altitude-distance plot of a scene and its corresponding power spectrum as a function of the wave number in a double-

³The FFT algorithm from MATLAB doesn't accept NaN values.

logarithmic scale. A linear function is fitted to the logarithm of the data ($\log(S_j(\log(k)))$), and

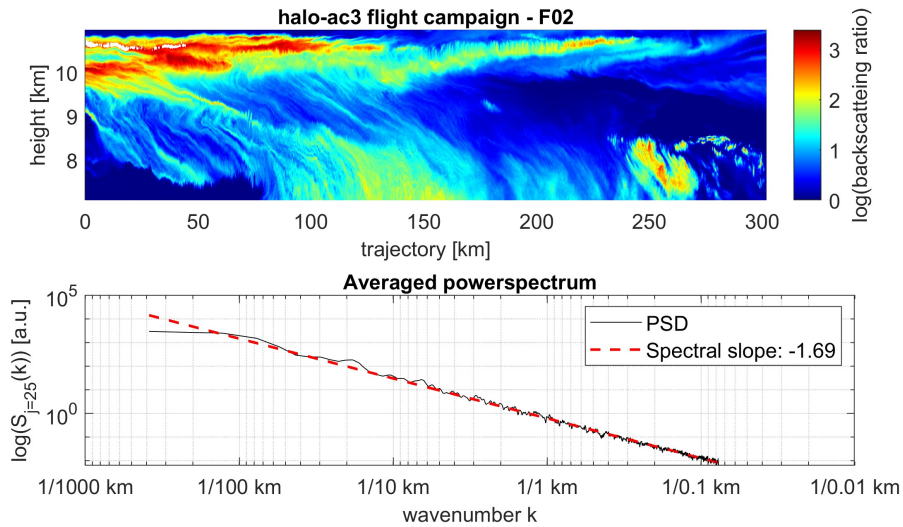


Figure 3.6: Top: slice of backscattering ratio profile. Solid, black line: corresponding power spectrum averaged over all altitude levels. Dashed, red line: corresponding spectral slope.

represents the scaling exponent of the spectrum. This example contains a cloud patch covering most of the horizontal and vertical extent of the data slice. With $k^{-1.68}$, the spectrum computed from this specific scene almost perfectly fits the characteristic turbulence slope of $k^{-5/3}$ up to scales of roughly 1/100 km, where the spectrum begins to level out. A slight bump can be seen at $k = 1/20$ km, which corresponds to a wavelength of 126 km, according to Equation 3.4. This fits the size of the dominant feature in this scene, resembling a pillar of falling ice crystals, skewed by wind shear. As a comparison, the example shown in Figure 3.7 contains a cloud extending over the same horizontal distance, however less homogeneous and with smaller-scale horizontal features. In this example, the spectrum begins to flatten at scales of 1 km and multiple peaks can be seen at scales of a few km to tens of km. The early flattening of the spectrum indicates that fewer signal power is contained in the larger scales of the data. The peaks in the spectrum may be attributed to localized features, for example, the peak in the spectrum, slightly below $k = 1/7$ km ($\lambda = 43$ km) may be related to the structure between 180 km and 270 km along the trajectory in the scene in Figure 3.7.

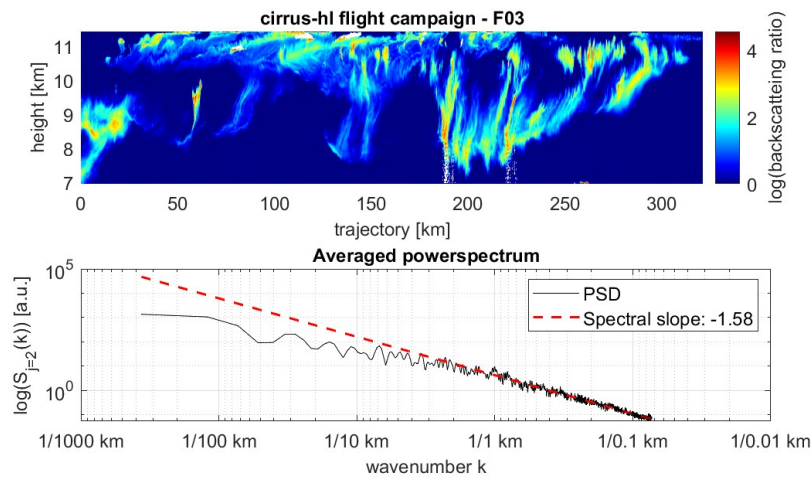


Figure 3.7: Top: slice of backscattering ratio profile. Solid, black line: corresponding power spectrum averaged over all altitude levels. Dashed, red line: corresponding spectral slope.

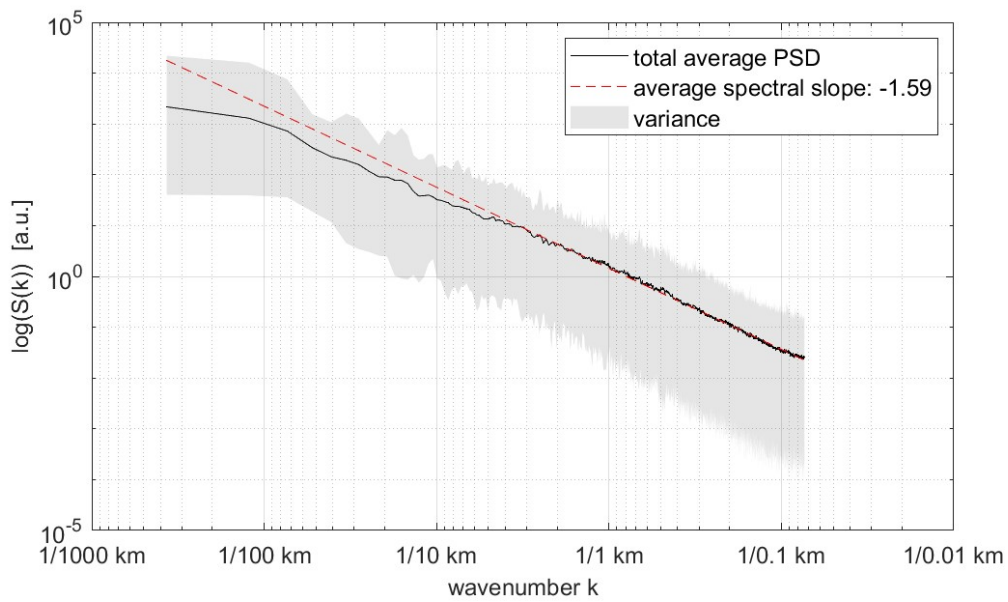


Figure 3.8: Solid, black line: Power spectrum of the backscattering ratio averaged over all the measurement data. Dashed, red line: corresponding spectral slope.

The averaged spectra from the several scenes exhibit different scaling exponents ranging from -2 to -1.3 (Figure 3.9) and show peaks related to the spatial features of the clouds. Prominent features are averaged out when computing the mean over all the available data, which leads to a smooth power spectrum, see Figure 3.8. The overall spectrum falls off with

$k^{-1.59}$ for k up to 1/4 km.

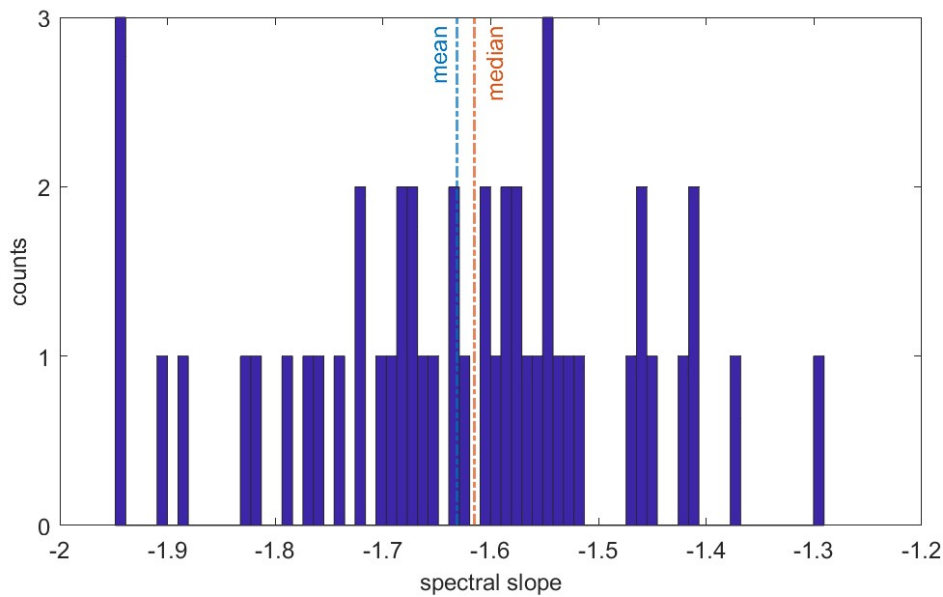


Figure 3.9: Histogram of the scaling exponents from the individual data scenes.

Above are presented the results of the spectral analysis using the non-uniformly⁴ sampled data. Interpolating the data to a uniformly sampled grid as shown in Code 7 introduced significant changes in the corresponding power spectra. The spectrum does not fall off with a straight slope, as opposed to the spectrum in Figure 3.8, which goes against the Kolmogorov turbulence model. Furthermore, a sharp dip occurs at scales below $k = 1/0.1$ km, which contradicts the expected flattening of the spectrum in sub-inertial scales. Due to these implausible characteristics, the results from the analysis with interpolated data are disregarded.

3.2 Magnitude of Backscattered Signal Power Variability

Previously, the spectral composition of horizontal clouds profiles were discussed. The following paragraphs focus on the magnitude of the backscattering variability an aircraft would typically experience while passing horizontally through a cirrus cloud. For this, lidar measurements of the attenuated backscatter are simulated for each point along the flight trajectory. In this context, the variability in backscattering magnitude is defined as the change in power level of the return signal from one point to the other. It is noted that the results presented in the following correspond to the simulated return signals of the AEROLI lidar, which has a specified transmit signal power of 8 W.

⁴With respect to the *trajectory* dimension.

Since the measurement range for gust detection with a DWL is around 50 m to 300 m, it is worthwhile to explore how much the conditions can change as the aircraft traverses these distances. However, the interpretation of those scales with the available data is limited, since the maximum spatial resolution is about 200 m to 250 m. The task is to compute the probability density function of the change in backscattered signal power within different distances. That is, how much does the signal level of the attenuated backscatter change after covering e.g. 230 m, 460 m, and so on. As aforementioned, the sampling w.r.t the trajectory dimension is non-uniform due to fluctuations in flight velocity of the airborne measurement platform. This means that the distance bins are only given approximately.

To obtain synthetic AEROLI attenuated backscatter from the observational data, the backscattering and extinction coefficients are retrieved from the WALES backscattering ratio and scaled to 355 nm wavelength as demonstrated in Table 3.5. With the atmospheric parameters established, the lidar equation and the instrumental specifications of AEROLI are used to compute synthetic lidar signals. The extinction and backscattering coefficients are functions of the trajectory flown during the observation period. The synthetic lidar signals are computed for values of range r that correspond to the trajectory dimension of the horizontal profiles of α and β . The peak power of the return signal is computed separately for each point along the horizontal dimension, which is representative for the flight trajectory of the airborne lidar. This can be understood as applying a moving window of a given length to $\alpha(r)$ and $\beta(r)$. The range r is defined as

$$r = r_0, r_0 + 1 \cdot dr, r_0 + 2 \cdot dr, \dots, r_0 + l_{win}, \quad (3.5)$$

where r_0 is the instantaneous position of the hypothetical lidar along the flight trajectory, and thus the starting point of the moving window and l_{win} is the length of the window. Since only the near range is important for this analysis, the attenuated backscatter is simulated for a range of 1000 m (window length) at a time. The peak value of the generated lidar signals is extracted and appended to a vector $\hat{P}_{return,i}(trajectory)$ which is the estimated maximum return signal power when flying along that specific altitude level i . Figure 3.10 illustrates the process of extracting the peak return power from synthetic attenuated backscatter signals computed from observed values of α and β . The lower plot in this figure shows α and β along the flight trajectory. The red, green and purple squares indicate the moving windows for different instantaneous positions r_0 . The middle plot depicts the synthetic lidar signal for the red window, from which the peak value is extracted and appended to the vector $\hat{P}_{return,i}(trajectory)$ (red cross in upper plot). This step is repeated for the green, purple, and all the subsequent windows along the trajectory. The procedure in Figure 3.10 is applied to all altitude levels i in a scene to obtain $\hat{P}_{return,s}(trajectory)$, where s is the index of the corresponding scene. To find the change in backscattered signal power after covering a given distance $\Delta r(n) = n \cdot dr$ ($n=1,2,3,\dots$), $\hat{P}_{return,s}(trajectory)$ is subtracted from itself shifted by n samples:

$$\Delta \hat{P}_{return,s}^n(trajectory) = \hat{P}_{return,s}(trajectory) - \hat{P}_{return,s}(trajectory - n \cdot dr). \quad (3.6)$$

This procedure is repeated for all of the 68 selected scenes. The results of all scenes are flattened and concatenated to form one vector $Delta \hat{P}_{return}^n$ for each value of n . The pro-

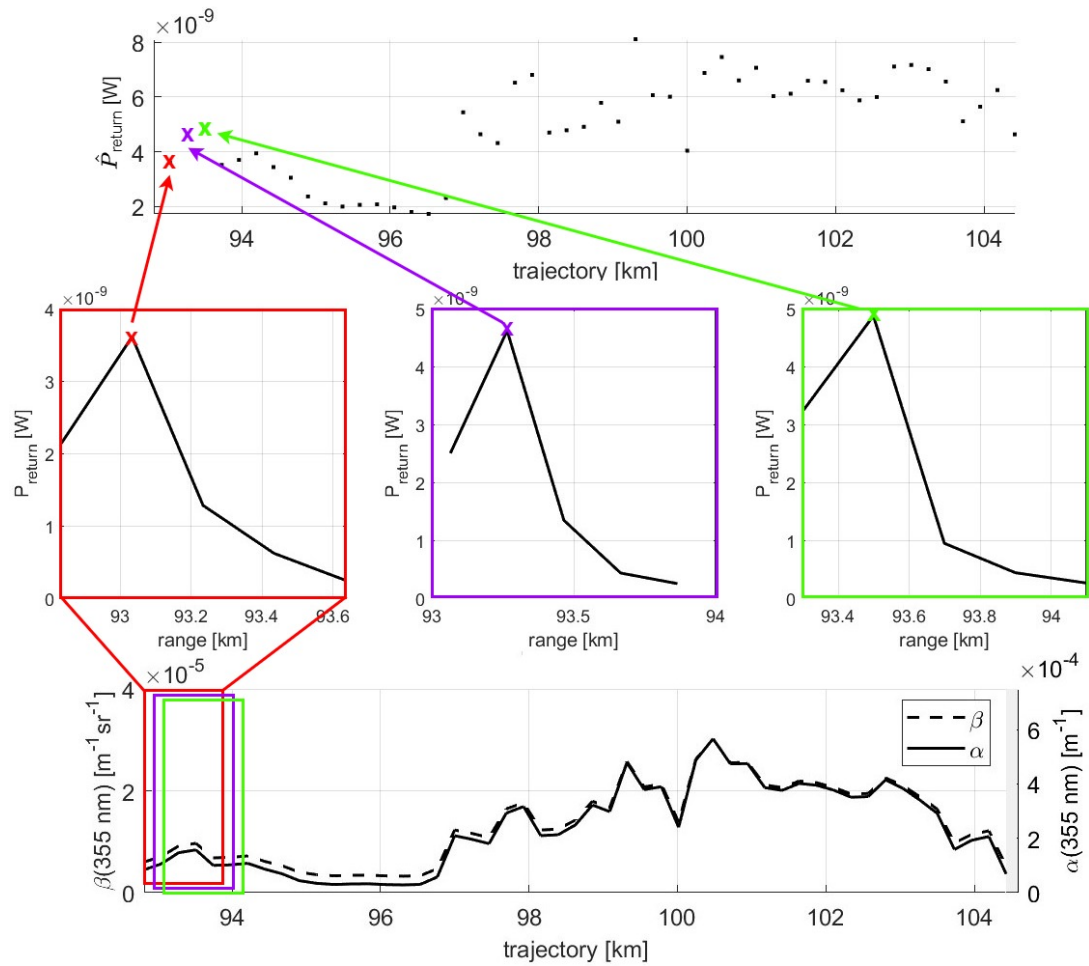


Figure 3.10: Extraction of the peak return power $\hat{P}_{return}(trajectory)$ from synthetic attenuated backscatter signals $P_{return}(r)$ computed from observed values of α and β for three different windows (red, purple and green rectangles).

cessing steps named above are represented in the pseudo code 7 in Appendix 7.

The probability density functions (PDFs) of $\Delta \hat{P}_{return}^n$ for $n = 1,2,3,4$ are approximated by computing the respective histograms. The histograms are calculated for ~ 3000 bins, and for each of the bins, the relative probability is determined as follows:

$$v_i = c_i/N, \quad (3.7)$$

where v_i is the bin value, C_i are the bin counts, and N is the total number of values in $P_{return}^n(r)$. The histograms are displayed in Figure 3.11 on a logarithmic y-axis. The bin edges of the histograms are interpolated to portray a smooth curve of the distribution. The vertical, dashed line corresponds to three times the standard deviation of $\Delta P_{return}^{n=1}$. With the specified hardware settings of the lidar (Table 3.1), this indicates that in 99.7 % of the cases, the return signal power measured by the lidar detector will fluctuate by less than 1.63 nW after covering ~ 230 m of distance (ca. 1s of flight time). In the extremes, changes of up to 18.37 nW can be observed within ~ 230 m.

The histograms reveal that most of the counts are concentrated around small variability values. As Δr increases, the probability moves from the center to the outside of the histogram. This indicates that most of the changes in return signal power are small, however larger changes happen more often at larger distances. This trend already starts to decrease for values of Δr larger than ~ 230 m. Even though no definite plateau can be observed, a much shallower slope of the trend sets in after $\Delta r \approx 20$ km, as illustrated Figure 3.12. This would be in agreement with the results of the spectral analysis, where the slope of the overall power spectrum flattens for scales larger than 10 km.

The 3σ value of 1.63 nW sets the boundary of the magnitude in variability the AGC must be able to balance. Based on this results, a validation procedure is devised, which is demonstrated in Chapter 6.

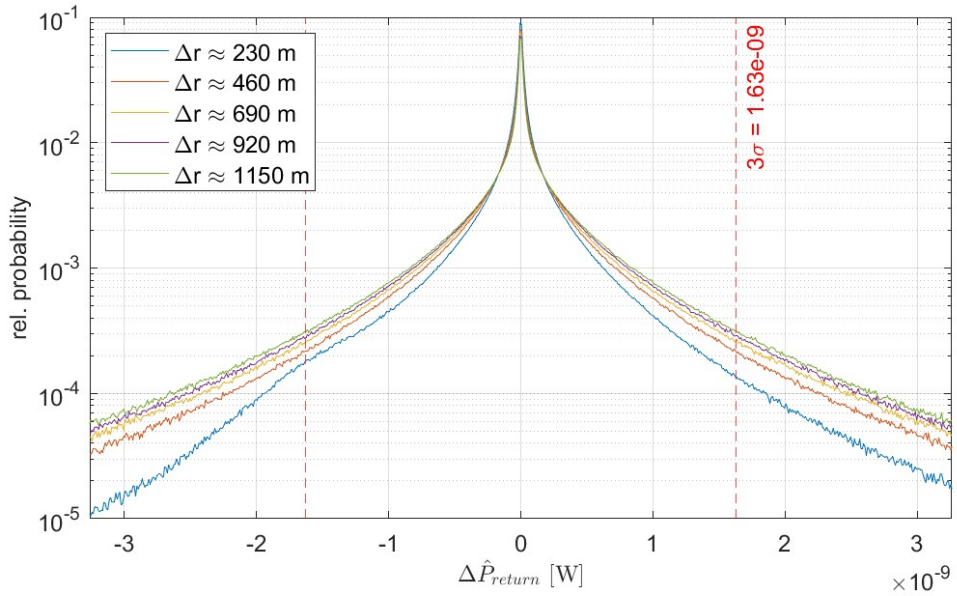


Figure 3.11: Histograms of $\Delta \hat{P}_{return}^n$ for $n = 1, 2, 3, 4, 5$. 3σ relates to $\Delta \hat{P}_{return}^{n=1}$.

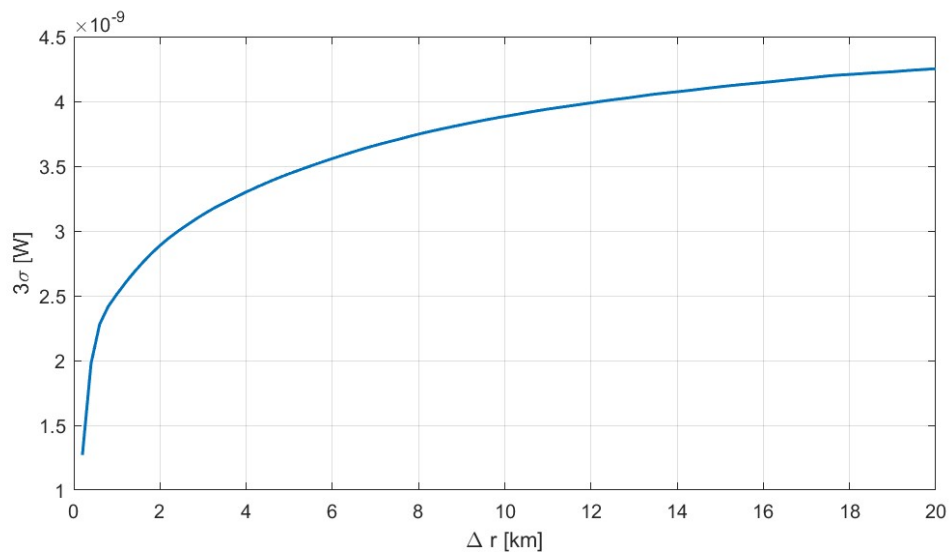


Figure 3.12: 3σ of the peak return signal power variability vs Δr .

Chapter 4

Experimental Set-Up

Both characterization of the detector subsystem electronics and the validation of the AGC are carried out with the same experimental set-up depicted in Figure 4.1.

A 355 nm CW-laser combined with an electro-optical modulator (EOM) and a function generator are used to create rectangular laser pulses at 100 Hz and 20 % duty cycle. In reality, the laser pulses, which are measured by the detector, have a shape as shown in Figure 2.11. The pulse shape is not of major concern for the design of the AGC, but the pulse length is and will be discussed in Chapter 5. Electro-optic modulators are frequently built around a Pockels cell, which is a crystal whose refractive index is modified by an electric field. The Pockels effect, or electro-optic effect, can be observed in lithium niobite (LiNbO₃) and other crystalline materials (Pockels 1906). This effect may impose a modulation on the phase, frequency, amplitude or polarization of the incident beam. Phase-modulating Pockels cells can be understood as voltage controlled half-wave plates, meaning they shift the polarization direction of light that is linearly polarized depending on the applied electric field. The change in polarization is achieved by introducing a phase delay between the two orthogonal components of polarization by changing the refractive index along one crystal axis. A phase delay of π will rotate the polarization by 90 degrees. The set-up in Figure 4.1 shows two polarizing beam splitter cubes (BS_1 and BS_2) before and after the EOM. BS_1 allows the S-polarized component to pass through the EOM, and BS_2 only allows S-polarized light to continue propagating through the setup. If the polarization in between is rotated back and forth by 90 degrees, this will produce quasi-rectangular pulses after BS_2 . The shape of the laser pulses is controlled by the trigger signal produced by a function generator. In order to induce the phase change of π , the trigger signal is amplified to high voltage.

Two neutral density filters (F1 and F3) are used to attenuate the laser power to the required level. The other filter (F2) is a gradual neutral density filter with an angle-dependent optical density and is driven by a servo motor. This part serves the validation of the AGC and will be discussed in more detail in Section 6.2.

The laser beam is passed through an optical fiber to a lens system, where lens L1 creates a collimated beam and lens L2 is a cylindrical lens, which reduces the laser beam's cross-section along the z-axis down to a line. This is to ensure that as much light as possible is captured by the sensor of the PMTA.

The detector assembly outputs voltage signals on 32 channels, however only the 16 cen-

tral channels are transferred to digital signals using two 8-channel Spectrum M2i.4932 analogue-to-digital converters (ADCs). The cards are connected to a measurement computer via PCI and have a sampling rate of 31.25 MS/s, a quantization depth of 16 bit and 256 MSamples of memory (Spectrum-Instrumentation 2023). They are triggered with the same signal used to create the laser pulses to synchronize the data acquisition. The detector gain can be adjusted at several points along the detection chain, e.g. type of PMT selected, or feedback resistor value of the TIA ¹.

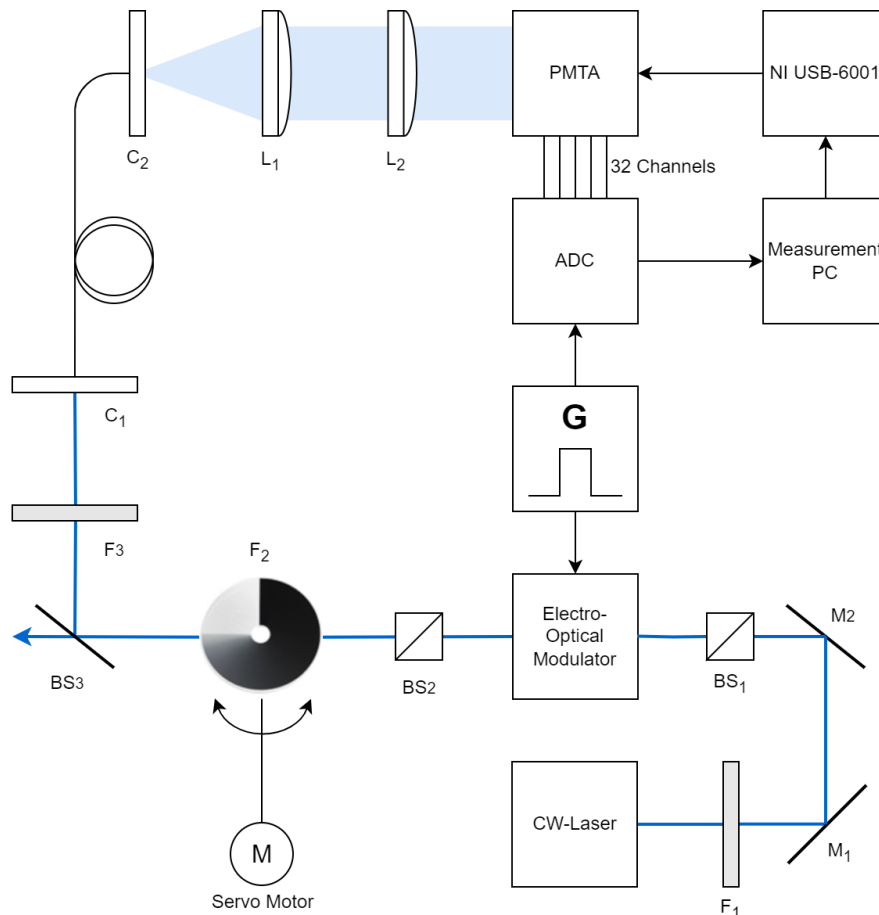


Figure 4.1: Experimental set-up for characterization of the detector electronics and validation of AGC. $F_{1,2,3}$: neutral density filters, $BS_{1,2}$: polarizing beam splitters, BS_3 : non-polarizing beam splitter, $C_{1,2}$: fiber couplers, L_1 : collimating lens, L_2 : cylindrical lens.

To dynamically adjust the gain of the PMT across a large range of values, the supply voltage is varied. The control of the PMT gain is done with the measurements computer by supplying the detector assembly with a gain voltage of 0-10 V using a National Instruments

¹More information on lidar signal detection in Chapter 2, Section 2.3.

USB-6001 digital acquisition card (DAQ) (National-Instruments 2023). The detector can be operated with a fixed gain voltage for characterization measurements, or with an adaptive gain voltage, when running in AGC mode.

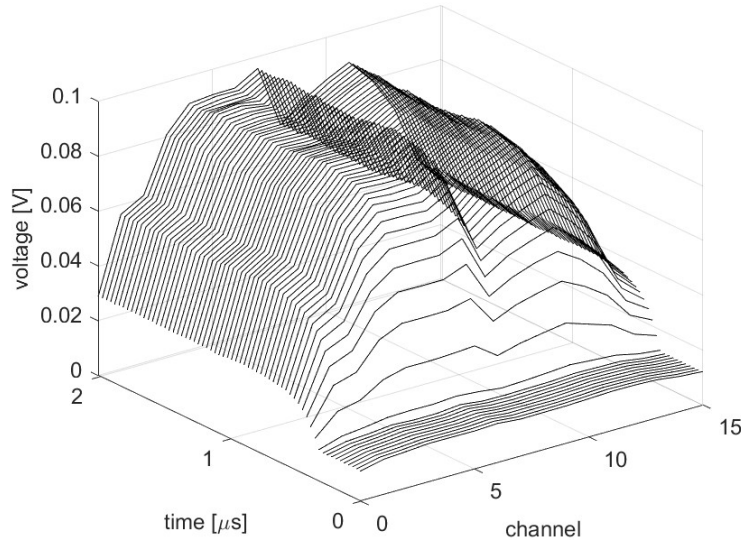


Figure 4.2: 2D voltage signal of a laser pulse's rising edge.

The data acquisition procedure is implemented in MATLAB code using designated drivers provided by the manufacturer of the digitizing cards (Spectrum Instrumentation). The detector gain controller is an addition to the data acquisition program and will be discussed in Chapter 6. The architecture is based on a first-in-first-out (FIFO) buffer acquisition mode. At the time the card receives a trigger signal, it starts recording samples at a frequency of 31.25 MSamples/s. Per received trigger, it records one segment consisting of 64 samples for each of the 8 channels, where four of the 64 samples are pre-trigger samples. These numbers were chosen to fit the initial slope and a part of the plateau of the laser pulse in one segment. The segments are stored in the FIFO buffer with a size of 128 MSamples. Whenever $8 \cdot N_P$ new segments have been recorded, the driver outputs $8 \cdot N_P$ segments from the end of the buffer. N_P corresponds to the number of pulses in one batch and the total number of samples per return action ($8 \cdot 64 \cdot N_P$) is the notify size (Spectrum terminology). N_P also determines the update rate of the AGC and will be discussed in more detail in the Chapters 5 and 6. Two acquisition cards run synchronously, which means that the data returned by the spectrum drivers after each notify size has the dimensions $(16, 64 \cdot N_P)$. The workflow of the data acquisition and processing is illustrated by the flowcharts in Figure 7.2 in the Appendix. Figure 4.2 shows the rising edge of the laser pulse measured across the 16 central channels of the PMTA.

Chapter 5

Characterization of the Detector Electronics

This chapter serves the description and characterization of the detector system, for which an AGC shall be designed. To guide the design parameters of the AGC, some properties of the detector system need to be understood beforehand. First, a simplified mathematical model of the complete detector chain is will be presented and compared with measurement data. Then, the response time of the whole detector system upon changes in the control voltage will be analysed to establish how fast the AGC can operate. Lastly, some measurements are taken to determine the dark current level of the PMT and the signal-to-noise ratio of the measurements.

5.1 Mathematical Description of the Detector Chain

The red, dashed box in Figure 2.9 indicates the position of the detector assembly within the AEROLI DWL system. A more detailed, but still abstracted representation of the detector assembly is shown in Figure 5.1.

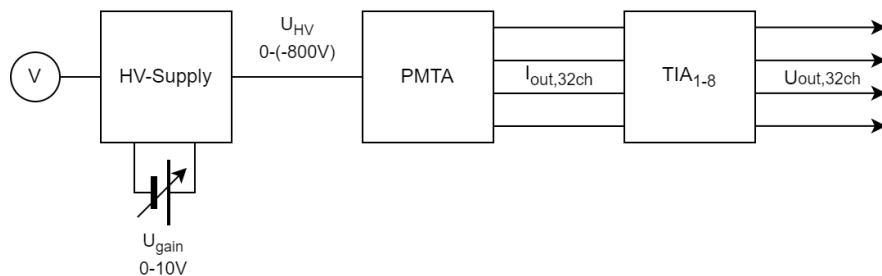


Figure 5.1: Reduced representation of the detector subsystem

A photo-multiplier tube array (PMTA), specifically a Hamamatsu H7260 32-channel linear array (Figure 5.2) is used to image the fringe pattern of the back-scattered signal. The supply voltage for the PMTA's dynodes comes from a high voltage module which steps up the input voltage (gain voltage U_{gain}) of 0 to 10 V to a voltage of 0 to -800 V (U_{HV}).



Figure 5.2: 32-channel linear photo-multiplier tube array (Hamamatsu H7260 Series) (Hamamatsu-Optics 2023).

The PMTA outputs a current on 32 channels for each pixel of the array. A set of eight transimpedance amplifiers (based on OPA4820, Texas-Instruments 2004) with a transimpedance gain of ca. $1\text{k}\Omega$ and four channels each, convert the 32 channel currents into voltage signals. The mathematical description of the detector chain illustrated in Figure 5.1 is given by:

$$U_{out,ch} = \eta_{rad} \cdot \mu(U_{HV}) \cdot P_{laser,ch} \cdot \kappa \cdot Z_{TIA}, \quad (5.1)$$

where $U_{out,ch}$ is the channel output voltage, η_{rad} is the radiant sensitivity of the PMTA's photocathode and $\mu(U_{HV})$ is the current amplification factor as a function of the supply voltage U_{HV} given by Equation 5.4. $P_{laser,ch}$ is the laser power illuminating one pixel of the PMTA and κ are the losses due to dead space between the pixels of the PMT array. Finally, Z_{TIA} is the transimpedance given by the feedback resistor R_F of the TIA shown in Figure 2.14. η_{rad} and $\mu(U_{HV})$ are provided by the manufacturer, Z_{TIA} has a value of $1\text{k}\Omega$, and $P_{laser,ch}$ can be adjusted with the different neutral density filters in the setup (Figure 4.1). As stated in Chapter 4, laser pulses at 100 Hz and 20 % duty cycle are generated. To measure the average laser power, a Newport 2936-C optical power meter is used. For the calculation in Equation 5.1, the instantaneous laser power is needed, which means, the average power \bar{P}_{laser} is divided by the duty cycle: $P_{laser} = \bar{P}_{laser}/0.2$. To obtain the laser power per pixel $P_{laser,ch}$, P_{laser} is divided by the number of pixels N_{ch} illuminated by the laser.

Table 5.1: Instrumental parameters of the AEROLI DWL (Vrancken and Herbst 2022).

variable	value	source
η_{rad}	$124 \cdot 10^{-3} \text{ A/W}$	PMTA datasheet
$\mu(800\text{V})$	$2 \cdot 10^6$	PMTA datasheet
P_{laser}	32 nW	measured
Z_{TIA}	1032Ω	internal communication , Linsmayer and Vrancken 2023
N_{ch}	32	

Using the values listed in Table 5.1, Equation 5.1 yields $U_{out,ch} = 0.20 \text{ V}$. In the experimental set-up shown in Figure 4.1, only 16 of the 32 channels are measured, which means that the

sum of the output voltage across all measured channels should amount to $U_{out} = 3.2$ V. It must be noted, that in this calculation, the illumination function of the PMTA sensor was not considered. Actually, the laser intensity is focused on the center channels of the sensor (those which are measured). As a consequence, the resulting value of U_{out} should be higher. On the other hand, U_{out} may be overestimated due to the fact, that the losses of the optics, C_2 , L_1 and L_2 in Figure 4.1, were not considered in this calculation.

Figure 5.3 displays the mean rising edge of a laser pulse resulting from summing up the measurements of 16 of the output channels, and then computing the average of the ~ 1000 laser pulses recorded during the measurement period. The grey area represents the noise envelope of the pulses (extreme values from the 1000 pulses). For the settings in Table 5.1, the detector measures a value of ~ 1.1 V for the plateau of the laser pulse. The measurement value is smaller than the theoretical estimate by a factor of roughly three. This deviation may be attributed to unaccounted losses in the optics, but most likely to the fact that the PMTA is designed for a pulse operation with much shorter pulses. The pulses generated with the EOM have a width of 2 ms, which for the PMTA is perceived as a quasi-continuous wave. If the illumination time of the PMTA is too large, then the output voltage begins to drop (Hamamatsu-Optics 2017, Linsmayer and Vrancken 2023).

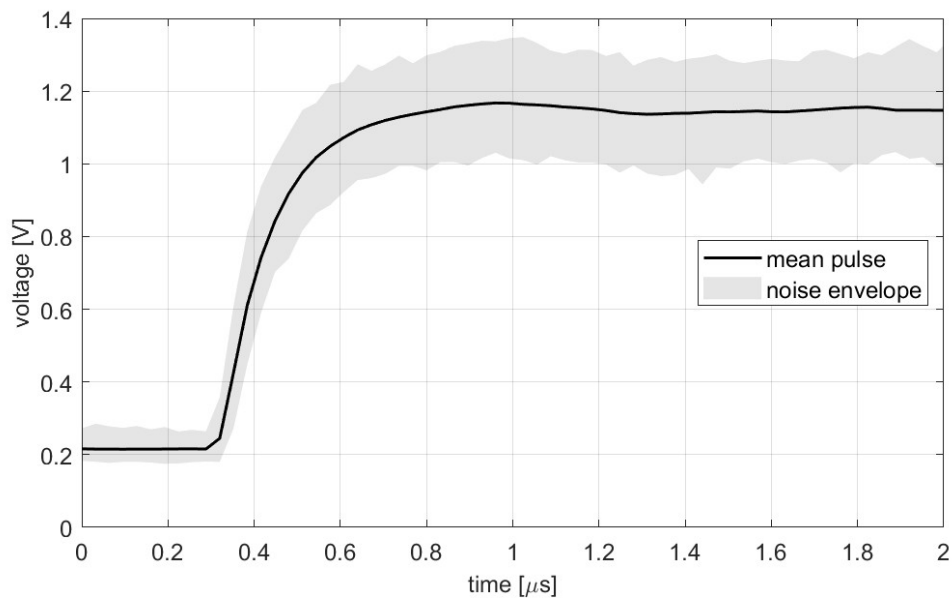


Figure 5.3: Rising edge of a laser pulse, measured with the set-up in Figure 4.1 and with the settings in Table 5.1. Solid line: average of ~ 1000 pulses. Grey area: noise envelope of the pulses.

Most of the electronics integrated in the detector assembly are assumed linear within their operation range. For example, the high voltage supply has a linear amplification factor of 80, and the TIA has a transimpedance gain defined by Z_{TIA} , which is also constant. The gain

of the PMTA, however, is not linear. According to the manufacturer, the current amplification factor μ is proportional to the supply voltage U_{HV} raised to the power of kn (Equation 2.13), where k is a material constant (ranging from 0.7 - 0.8) and n is the number of dynodes in the PMTA ($n = 10$ for Hamamatsu h7260). The proportionality constant a is not specified. The effective use of PID controllers is limited to LTI systems. If U_{HV} or U_{gain} are used as the controlled variable, changes applied to them will cause non-linear changes in the system output and lead to instabilities. To overcome this issue, μ is defined as the controlled variable, since it is proportional to the system output. Then, U_{gain} is derived analytically from μ with Equation 2.13.

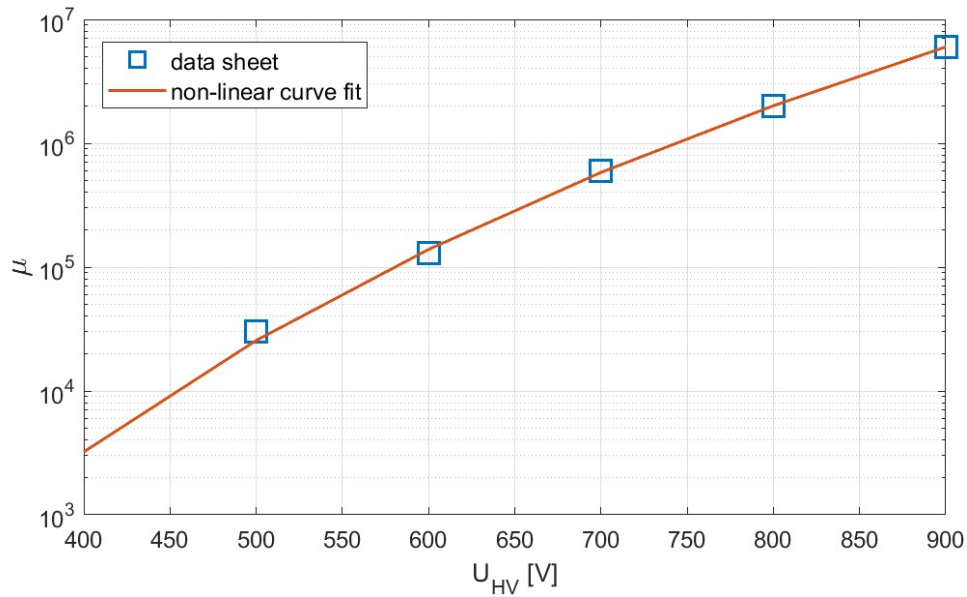


Figure 5.4: Solid line: Non-linear curve-fitting of gain μ vs. supply voltage U_{HV} . Squares: data from the data sheet of the PMTA (H7260-200).

In order to find exact values for a and k , data points are extracted from a rating curve in the data sheet of the PMTA (H7260-200) and fitted to the model in Equation 2.13 by using the *lsqcurvefit* function from MATLABs optimization toolbox (MathWorks-Inc. 2023b). This function is based on a non-linear least-squares solver with the following form:

$$\min_c \sum_i (F(c, U_{HV}) - \mu)^2, \quad (5.2)$$

where $F(c, U_{HV})$ is the function in Equation 2.13, and c are the coefficients that solve the problem. c is a two-dimensional vector containing the unknown constants a and k . Equation 2.13 is rewritten as:

$$F(c, U_{HV}) = a^n \left(\frac{U_{HV}}{n+1} \right)^{kn}, \quad (5.3)$$

where n , the number of dynodes is set to 10, as indicated in the data sheet. The solid line in Figure 5.4 shows the result of the non-linear curve-fitting with the coefficients $c_1 = a = 0.0797$ and $c_2 = k = 0.9285$. Even though the manufacturer specifies values between 0.7 to 0.8 for k , it was kept variable to obtain a better fit. The least squares adjustment yields the following analytical expression for μ as a function of U_{gain} :

$$\mu(U_{gain}) = 2.214 \cdot 10^{-21} (U_{gain} \cdot 80)^{9.285}, \quad (5.4)$$

with a normalized root mean squared error (NRMSE) of the residuals of 0.59 %, given by:

$$NRMSE = \frac{1}{\bar{\mu}} \sqrt{\frac{1}{n} \sum_{i=1}^n (\hat{\mu} - \mu)^2}, \quad (5.5)$$

where $\hat{\mu}$ are the predictions from Equation 5.4, μ are the data points from the data sheet and $\bar{\mu}$ is the respective average. The inversion of Equation 5.4 is as follows:

$$U_{gain}(\mu) = 2.096 \cdot \mu^{1/9.285}. \quad (5.6)$$

The integration of Equation 5.6 in the implementation of the AGC is discussed in Chapter 6.

5.2 Time response - Experimental Derivation

For LTI systems of first order, the response time to a step input is characterized by the time constant τ . Physically, τ is the time elapsed until the system reached $1 - 1/e \approx 63.2\%$ of the final output value. Another important temporal characteristic of an LTI system is the settling time. It is defined as the time it takes for the system to remain within a certain margin around the final output value. Each electronic component of the detector system has its own rise and settling time and is most likely not a first-order LTI system. For the sake of simplicity, the complete detector system is viewed as a grey box system, which means that it will be characterized as if it was one single first-order LTI. The reasons for that simplification are the following. The manufacturer assures that the settling time of the PMTA's μ upon an input voltage step is typically 0.3 ms and that in reality it is limited by the time response performance of the high voltage power supply. From experience inside the Lidar department of DLRs Institute of Atmospheric Physics, it is known that the power supply of the detector system (XP Power DC-HVDC converter C10N) is quite slow, with a time response in the higher millisecond range.

At this point, some terminology regarding different response times must be introduced to avoid confusion. The response time of the photon-to-electron conversion of the PMTA upon a change in the intensity of incident light is defined as photocurrent response time. The response time of the current gain factor μ of the PMT upon a change in the supply voltage of the dynodes is henceforward called μ response time. Lastly, the HV voltage U_{HV} response time upon a change in the control voltage U_{gain} is related to the DC-HVDC converter electronics and in the following referred to as HV supply response time. For the Hamamatsu H7260, the manufacturer specifies a typical rise time of 0.6 ns. In this case, the system

(PMTA) reacts much faster to a disturbance (light) than the HV supply reacts to a change of U_{gain} . It must be noted that what in this scenario is defined as the disturbance, is normally the measurement variable for which the PMTA is sensible.

The objective of determining the HV voltage response time is to find out what the maximum update rate of the controller can be. If the controller is updated before the system has reached steady state, instabilities will arise. To measure the response time with the set-up shown in Figure 4.1, a 0.5 Hz square wave is given as input voltage (U_{gain}) to the detector. As previously mentioned, the measurement cards read the first 64 samples of the 100 Hz laser pulses across 16 channels, since the information along the channels (usually containing the Doppler spectral information) is not needed for the present analysis. The data are reduced to a one-dimensional vector by summing them up along the channels. For each laser pulse, a median value of the steady state section of the pulse is computed. This creates one value per laser pulse, effectively down-sampling the data to the pulse repetition frequency of 100 Hz (illustrated in Figure 7.2). Data are recorded for 40 seconds, resulting in 20 cycles of U_{gain} . To smooth out noise, the cycles are stacked and a mean along the cycles is computed. Lastly, the averaged data is normalized to a range between 0 and 1, to simulate a unity step response. Figure 5.5 illustrates the pre-processing steps explained above.

The rising edge (positive input step response) and the falling edge (negative input step response) of the pre-processed square wave response data (bottom right plot in Figure 5.5) are analysed separately to obtain the respective rise and settling times. MATLABs system identification toolbox (MathWorks-Inc. 2023c) is used to fit a first-order transfer function to both the rising edge and the falling edge with the *tfest* function. The function takes the measured input (U_{gain}) and output data (U_{out}), normalized between 0 and 1, as well as the number of poles and zeros as input arguments. For a simple first-order system, the number of poles and zeros are set to 1 and 0 respectively. The resulting transfer function has the form:

$$H(s) = \exp(-t_d \cdot s) \frac{K}{s + 1/\tau}, \quad (5.7)$$

where t_d is the output delay, K is the gain factor and τ is time constant. After obtaining the transfer function, some parameters associated with the step response can be accessed with the function *stepinfo* from the control system toolbox (MathWorks-Inc. 2023a). Two of those are of interest, namely the rise time t_{rise} and the settling time t_{set} . Mathworks defines the rise time as the time it takes for the system output to rise from 10 % to 90 % of $|y_{init} - y_{final}|$, where y_{init} the initial output and y_{final} is the output value at steady-state. The settling time is specified as the time until the error stays below 2% of $|y_{init} - y_{final}|$. The rise and settling times of the rising edge and the falling edge are estimated for different input steps to cover different scenarios. First, the offset (initial value) of the step is kept constant, but the step size (final value - initial value) is varied, and then the offset is varied and the step size is kept constant. The steps are chosen such that the complete dynamic range of μ is covered evenly. For the measurements μ is converted to U_{gain} as explained above. Table 5.2 summarizes the parameters of the input steps that are measured.

The rising and settling times of both the positive and negative input step responses listed in

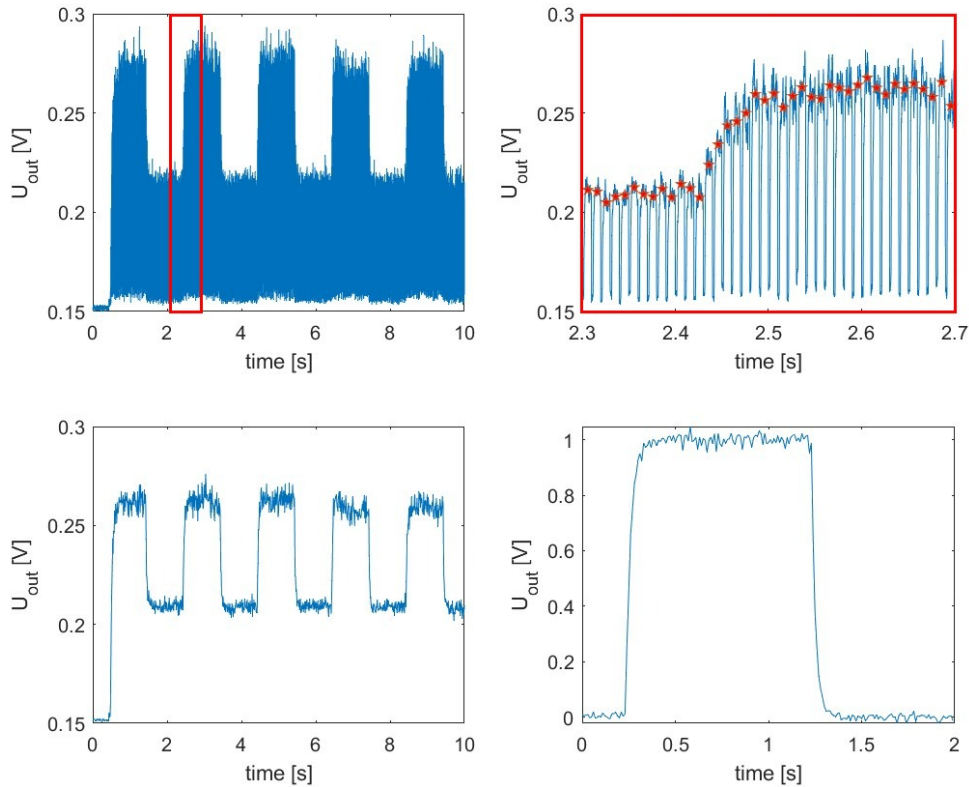


Figure 5.5: Illustration of the pre-processing steps for the response time analysis. Top left: first 10 s of the raw output voltage. The red box marks the zoom-in section shown in the top right plot. Top right: enlarged view of the raw data. The red stars indicate the median values of the individual pulse plateaus. Bottom left: down-sampled output data. Bottom right: mean value of all the periods from the down-sampled output data.

Table 5.2 are presented in Figure 5.6 and Figure 5.7, respectively. The plots on the left hand side represent the response times as functions of the input step size and the plots on the right hand side represent the response times as functions of the input offset. A first visual inspection reveals what can already be seen in the bottom right plot of Figure 5.5, namely that stepping up the input voltage is a slower process than stepping it down, meaning the falling edge of the square wave response is steeper than the rising edge. Looking at the positive step responses, both the rising and settling time only increase slightly, by increasing the step size. On the other side, when increasing the offset of the input step, at a constant step size (w.r.t. μ), both the rising and settling time decrease more strongly. In the case of the right hand side plot, the step size is constant w.r.t. μ , but it decreases in terms of U_{gain} . This indicates, that there is a linear relationship between U_{gain} and the response time, which may be attributed to the high voltage supply.

Table 5.2: Parameters of the input steps measured for the time response analysis.

offset		step size	
U_{gain} [V]	μ	U_{gain} [V]	μ
6.36	$3 \cdot 10^4$	1.63	$2.18 \cdot 10^5$
6.36	$3 \cdot 10^4$	2.19	$4.37 \cdot 10^5$
6.36	$3 \cdot 10^4$	2.55	$6.59 \cdot 10^5$
6.36	$3 \cdot 10^4$	2.82	$8.74 \cdot 10^5$
6.36	$3 \cdot 10^4$	3.03	$1.09 \cdot 10^6$
6.36	$3 \cdot 10^4$	3.22	$1.31 \cdot 10^6$
6.36	$3 \cdot 10^4$	3.38	$1.53 \cdot 10^6$
6.36	$3 \cdot 10^4$	3.52	$1.75 \cdot 10^6$
6.36	$3 \cdot 10^4$	3.64	$1.97 \cdot 10^6$
7.99	$2.48 \cdot 10^5$	0.56	$2.19 \cdot 10^5$
8.55	$4.67 \cdot 10^5$	0.36	$2.22 \cdot 10^5$
8.91	$6.89 \cdot 10^5$	0.27	$2.15 \cdot 10^5$
9.18	$9.04 \cdot 10^5$	0.21	$2.16 \cdot 10^5$
9.39	$1.12 \cdot 10^6$	0.19	$2.22 \cdot 10^5$
9.58	$1.34 \cdot 10^6$	0.16	$2.22 \cdot 10^5$
9.74	$1.56 \cdot 10^6$	0.14	$2.22 \cdot 10^5$
9.88	$1.78 \cdot 10^6$	0.12	$2.22 \cdot 10^5$

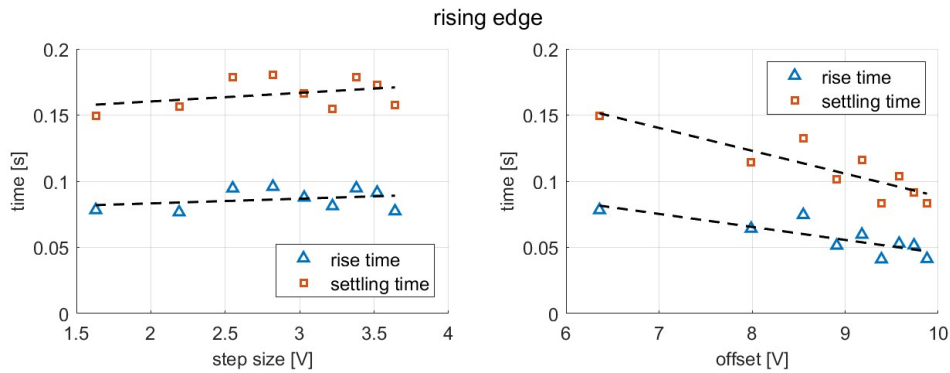


Figure 5.6: Rise times and settling times of the rising edges of the input steps listed in Table 5.2

For the case of an negative input step, an inverted trend can be observed. Increasing the step size causes a reduced response time and raising the offset slightly enhances the response time.

Table 5.3 presents the statistics of the data in Figure 5.6 and Figure 5.7. For a stable operation of a feedback controller, it must be assured that the output of the detector has settled before the controlled variable is updated. Therefore, the definition of the update rate of the AGC is based on the settling time of the detector system. The maximum settling time

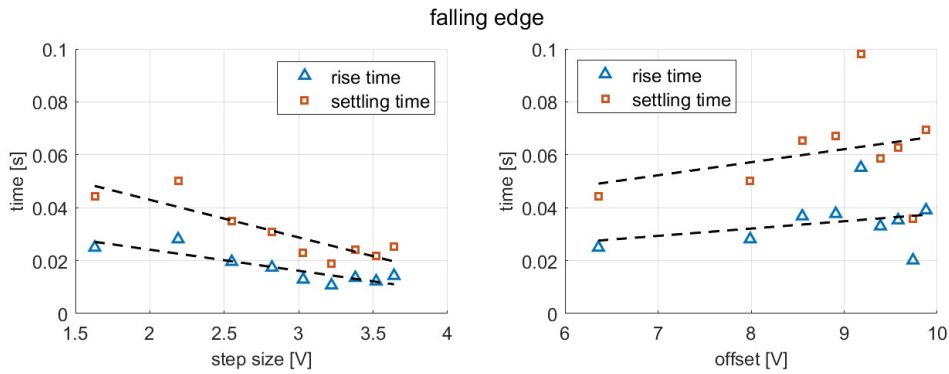


Figure 5.7: Rise times and settling times of the falling edges of the input steps listed in Table 5.2

measured in this experiment is 181 ms and is owed to a positive input step. This considered, the minimum update rate of the AGC shall be no smaller than 181 ms.

Table 5.3: Parameters of the input steps measured for the time response analysis.

input step	t_{rise} [ms]			t_{set} [ms]		
	min	max	mean	min	max	mean
positive	41	96	72	83	181	137
negative	11	55	26	19	98	46

5.3 Dark Current and Signal-to-Noise-Ratio

Figure 5.3 displays the rising edge of a single laser pulse, as measured with the experimental set-up presented in Chapter 4. Over a period of n seconds, $n \cdot PRF$ laser pulses are recorded, where PRF is the pulse repetition frequency of the laser. The solid black line indicates the average of all pulses over a period of several seconds and the gray area describes the lower and upper boundaries of the noise level. During the initial part of the signal (up to $\sim 0.3 \mu s$), the laser does not emit light. Yet a voltage of more than 200 mV is measured across the central 16 detector channels. The current produced by the PMTA when not illuminated is called dark current and is related to the random generation of free electrons, not associated with the photoelectric effect. The dark current is a bias signal, independent of the irradiation intensity, but dependent on the supply voltage of the PMTA dynodes. The dashed red line in Figure 5.8 illustrates the output voltage owed to dark current U_{dark} for increasing U_{gain} and the solid black line is the amplitude of the actual laser pulse U_{pulse} . Both U_{dark} and U_{pulse} display an exponential relation w.r.t. U_{gain} . The dotted black line indicates the signal-to-noise ratio (SNR) of the laser pulses, which is the standard deviation of the noise computed across several pulses, divided by the mean value of the laser pulse amplitude U_{pulse} . As seen in the figure, at $U_{gain} = 4$ V and below, no signal is detected. From there on, the SNR continuously rises and reaches values of 13-14 for U_{gain}

larger than 8 V. To assure good quality measurements, the lower boundary of U_{gain} is set to 6.5 V for the experiments presented in Chapter 6

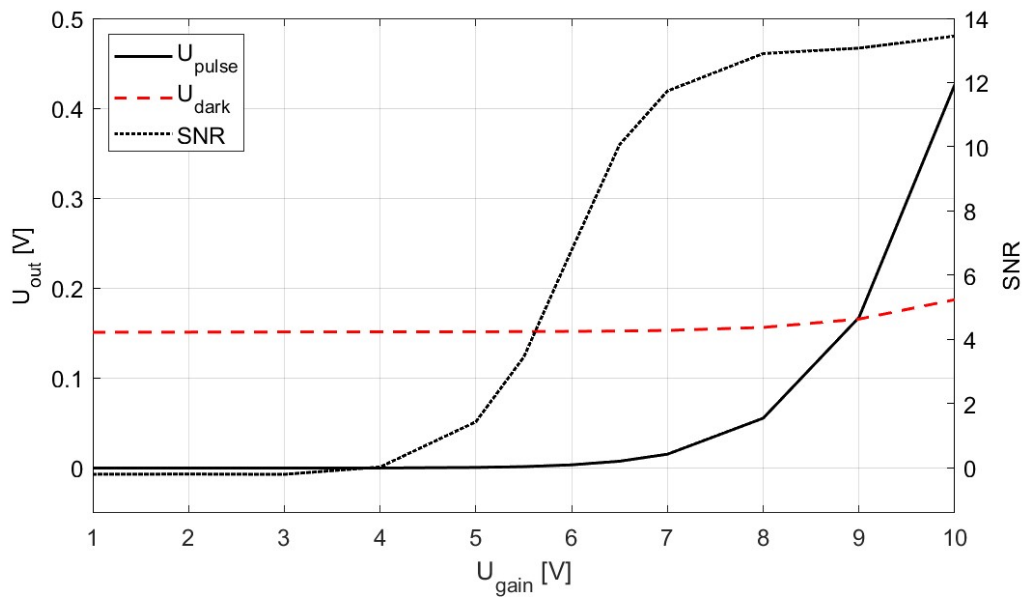


Figure 5.8

Chapter 6

Automatic Gain Controller

In the last chapters requirements for an automatic gain controller (AGC) were formulated based on hardware limitations of the lidar detector system of discussion and the estimation of operational conditions extracted from observational data. The task of the AGC is disturbance rejection. In the context of the application at hand, the disturbance is the variation in back-scattering caused by cirrus clouds inside the field of view of the DWL instrument, which results in changes of the returned signal power. In this section, the design process of an AGC capable of balancing the expected variability in return signal power is described. Initially, the classical PID-controller design is considered, and the Ziegler-Nichols tuning method is used to find the optimal controller gains. However, this approach does not deliver good results. As a consequence, the derivative path of the controller is eliminated, ultimately resulting in a PI-controller design, which fulfills the task of disturbance rejection within a margin of error of less than 10 %.

6.1 Design and Implementation

An important design parameter is the controller update rate dt . To set a suitable value, the settling time of the detector system must be considered. The investigations described in Chapter 5 revealed that the time until the detector reaches 99 % of its final output value may range from 11 ms to 181 ms, depending on the change of the input U_{gain} . Updating the controller faster than that will lead to instabilities of the system. The update rate of the controller is determined by the settings of the data acquisition procedure. As explained in Chapter 4, the drivers of the acquisition cards are set up such that a batch with a pre-defined number of samples (named notify size) is returned at a time. The notify size is defined as $8 \cdot 64 \cdot N_P$, where 8 is the number of channels per acquisition card, 64 the number of samples per laser pulse and N_P is the number of laser pulses. The update rate dt is ultimately defined by N_P and at a pulse repetition frequency of 100 Hz, dt equates to $n_P \cdot 10ms$. The smallest value for N_P accepted by the ADC driver, which is larger than 181 ms, is 24, thus dt is set to 240 ms.

In Figure 2.18, the form of the classical PID controller is depicted, and Figure 2.15 describes the common terminology of a feed back controller. The implementation of the PID controller in code is realized with basic mathematical operations. The proportional path of the controller is simply the multiplication of the proportional gain K_p with the output error e . The

integrating path is computed by means of discrete integration. The simplest form of discrete integration is achieved by incrementing a variable, let's say int , by the factor $K_i \cdot dt \cdot e$ after every iteration of the feedback loop. Here $dt \cdot e$ represents the area under the curve described by $e(t)$ within a time period of dt , and K_i is the integrating gain. For the derivative path, the secant line between successive values of $e(t)$ is computed as $(e(t) - e(t - dt))/dt$ and scaled by the derivative gain K_d .

The pseudo code 7 in the appendix, describes the implementation of the AGC in MATLAB. r is the setpoint, y the system output, and thus e the output error. In the first loop iteration, the integrating path and the prior value of e are initialized. The loop is updated every $dt = 240$ milliseconds. In this time, 24 laser pulses are recorded, from which y is computed by first determining the steady state value of each of the pulses and then building an average. e is evaluated at the beginning of each loop iteration and subsequently the proportional, integrating and derivative paths are updated. The three paths are summed up to build u , which represents the current amplification factor μ of the PMTA. In line 16-19 of the pseudo code 7, upper and lower limits for the controlled variable u are defined to avoid wind-up. This is when the controller output increases beyond what the hardware can supply. The upper boundary is set to the value of μ corresponding to $U_{gain} = 10$ V. The lower boundary is set to the value of μ corresponding to $U_{gain} = 6.5$ V beyond which the SNR of the measurements is too low to differentiate between signal and dark current of the detector (see Figure 5.8). At the end, the controller output U_{gain} is computed by with Equation 5.6, as explained in Chapter 5.

The controller gains are tuned following the Ziegler-Nichols method mentioned in Section 2.4. For this purpose, the detector is illuminated with a constant laser power, K_i and K_p are set to zero and K_p is set to an arbitrary non-zero value. At the beginning of the data acquisition program, U_{gain} is turned down to 0 V and the controller will attempt to adjust it in order to reach the specified setpoint r . K_p is increased iteratively until a sustained oscillation of the system output is achieved, then K_i and K_d are computed according to Table 2.1. In Figure 6.1, the detector output for several values of K_p is plotted. Up to $K_p = 10^5$, no change can be seen in the output. At $K_p = 10^6$, U_{out} goes up to a steady state value of ~ 0.17 V. Raising K_p to $5 \cdot 10^6$ produces some initial oscillations which subside and converge to ~ 0.23 V. For $K_p = K_u = 10^7$, a sustained oscillation of the output at a period of around 1 second is achieved. The black line represents the hypothetically optimal gain settings according to the Ziegler-Nichols tuning method ($K_p = 6 \cdot 10^6$, $K_i = 1.2 \cdot 10^7$ and $K_d = 7.5 \cdot 10^5$). It is evident that these are not the right PID settings, since nothing anywhere close to stability is produced by them. Therefore, the gain settings are rolled back to $K_p = 1 \cdot 10^6$, $K_i = 0$ and $K_d = 0$ and from there only K_i is incremented step by step. This approach is depicted in Figure 6.2, where the black line portrays the final gain settings. With this configuration, K_i is 8.5 times larger than K_p and thus dominates the controller output. The setpoint is reached within ~ 1 second with a slight overshoot.

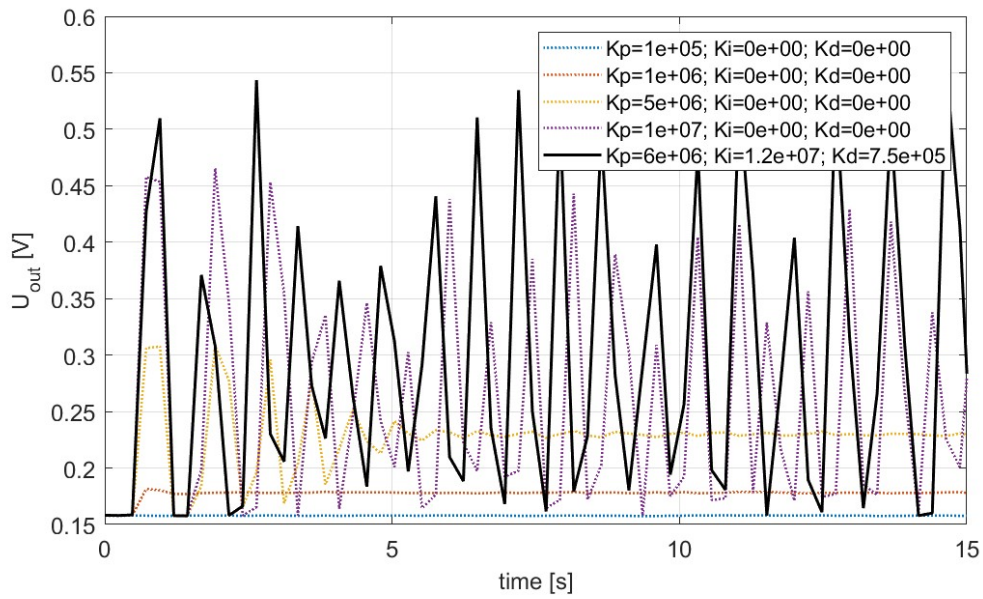


Figure 6.1: PID tuning procedure. The dotted lines are the output achieved by incrementing the proportional gain K_p until a sustained oscillation is achieved. The solid line represents the system output with the hypothetically optimal PID gains.

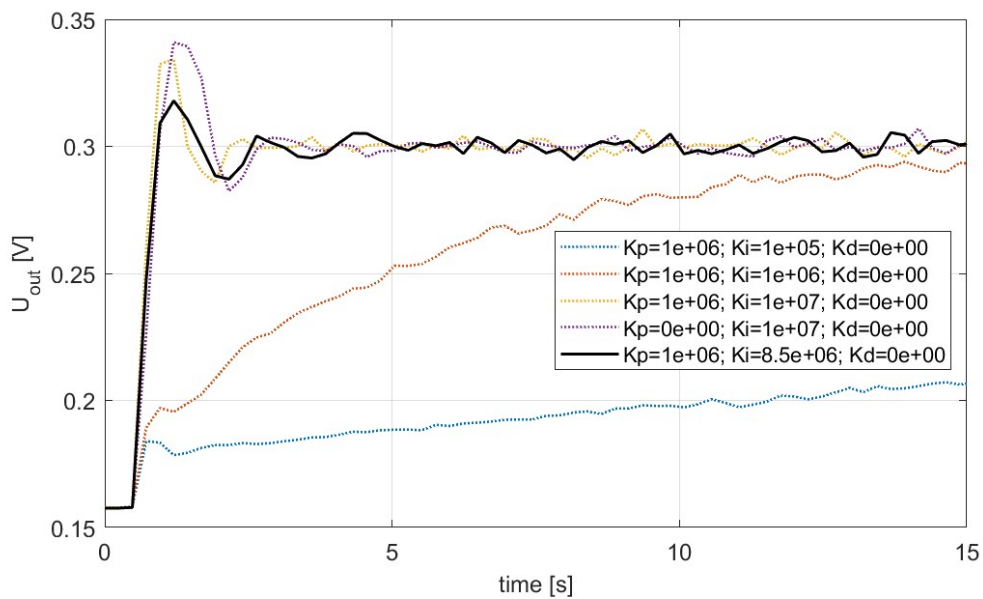


Figure 6.2: PI tuning procedure. The dotted lines are tuning attempts and the solid line represents the system output with the final gains.

6.2 Testing

In Chapter 3, the variability of the backscattered signal power level for horizontal cirrus cloud profiles was computed from observational data. The results serve as a reference for the conditions expected during flight operation of the AEROLI lidar, and are used in the following to compose a testing procedure for the AGC.

A probability density function for the changes in return signal power was computed in Chapter 3. The changes relate to the horizontal translation of the aircraft through a cloud, due to which the backscattering conditions change. For a GLA, measurements in the near field (50 m - 300 m) are of interest, which is why the changes that occur after every ~ 230 m along the flight profile were considered. It was found that in 99.7 % of the cases, the fluctuation of return signal power will lie below 1.63 nW for the AEROLI system with the specifications listed in Table 3.1. An AGC that can ensure a good level of disturbance rejection 99.7 % of the time can be considered very reliable. Based on this statement, a validation procedure is developed, which shall be explained in the following.

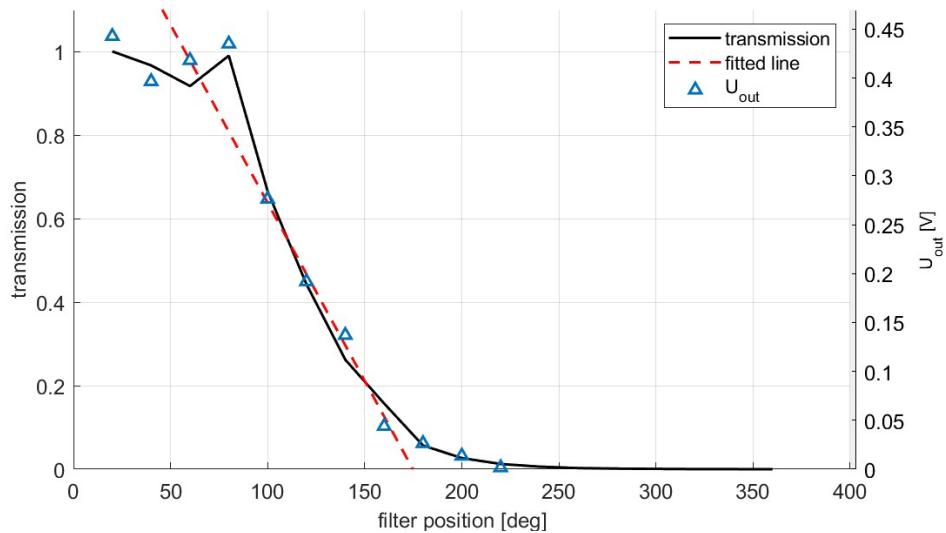


Figure 6.3: Solid line: Filter transmission vs. filter position in degrees. Triangles: corresponding output signal level. Dashed line: linear fit of the transmission for angles between 100 and 150 degrees.

The experimental set-up shown in Figure 4.1 includes a gradual neutral density filter with an angle-dependent optical depth. It is placed such that the rotation of the filter will cause an attenuation of the laser beam. The task is to rotate the filter in a manner that will produce a laser power variability representative for the conditions while traversing a cloud. For this, a random sub-sample from $\Delta \hat{P}_{return}^{n=1}$ with values for below 1.63 nW is taken (refer to 3 for context). The cumulative sum of the the random sample of ΔP (change in laser power) is

computed to obtain the laser power profile P_{laser} which shall be performed during the test of the AGC. The relation between filter position (in degrees) and transmission is determined by turning the filter step by step and recording the corresponding laser power in the process. The mean laser power is measured by a Newport 2936-C optical power meter with a 918-D detector head connected via an optical fiber at the fiber coupler C_1 in Figure 4.1. Later, the same process is repeated, but with the detector connected, so that the output voltage depending on the filter angle can be measured. The measured transmission and corresponding output voltage values U_{out} are plotted against the filter position, as illustrated in Figure 6.3. With this set-up, a transmission of 1 refers to a mean laser power of 6.8 nW^1 . The filter is transparent up to ~ 90 degrees, then the transmission gradually decreases until it reaches a plateau at ~ 260 degrees, where the transmitted power falls below the sensitivity of the power meter. A linear function is fitted to the transmission curve for angles between 100 and 150 degrees, where the slope is approximately linear. This function is used to compute the angles α_{filter} corresponding to the values of P_{laser} .

Test 1 - randomly varying laser power

Two tests are carried out in order to assess the performance of the AGC. During the first test, the angles of the rotating filter α_{filter} are adjusted by a servomotor at a rate of 1 Hz. The angle values are interpolated to a finer grid of 200 ms to assure a smooth transition between the values in α_{filter} . In the beginning of the test, the angle is turned evenly from 100 degrees to 150 degrees and back to 100 degrees (dotted line until 19 seconds in Figure 6.4). This serves as a reference to align the data for visualization. After the reference procedure is done, the α_{filter} sequence begins (dotted line in Figure 6.4 starting at 19 seconds). The first test is executed in two steps. First, the varying laser signal produced by the turning filter is measured by the detector while the controller is disabled. During this part, the control voltage of the detector U_{gain} is fixed to a value that corresponds to an output voltage of 300 mV at a filter position of 100 degrees. In the second step of the first tests, the same procedure is repeated. However, the controller is enabled with setpoint of 0.3 V. Figure 6.4 displays the measurements taken during *Test 1*. In the upper plot, the output voltage U_{out} is depicted. The dotted, orange line represents the measurement taken without an AGC and the solid, blue line is the output controlled by the AGC. In the lower plot, the filter transmission is shown as a black, dotted line and the controller output U_{gain} as a solid blue line. It can be seen that the AGC successfully counteracts the changes in laser power, as U_{gain} approximately describes the inverted pattern of the filter transmission. A closer look reveals that U_{gain} lags behind the changes in signal power (represented by the filter transmission) at about 1-2 seconds. This might be attributed to the slow controller update rate, which is limited by reaction time of the HV module of the detector electronics. The grey box indicates a tolerance margin of $\pm 10\%$ around the setpoint. As can be seen, the AGC manages to keep the detector output within $\pm 10\%$ of the setpoint almost during the whole period of the test. It is only until the first second, that the output is outside the

¹The artifact at ca. 60 degrees may be due to a finger print on the filter.

tolerance, because the controller needs a while to build up U_{gain} . In contrast, the output of the uncontrolled detector falls outside the tolerance for roughly half of the duration of the test. This happens when the attenuation of the laser goes beyond $\sim 50\%$.

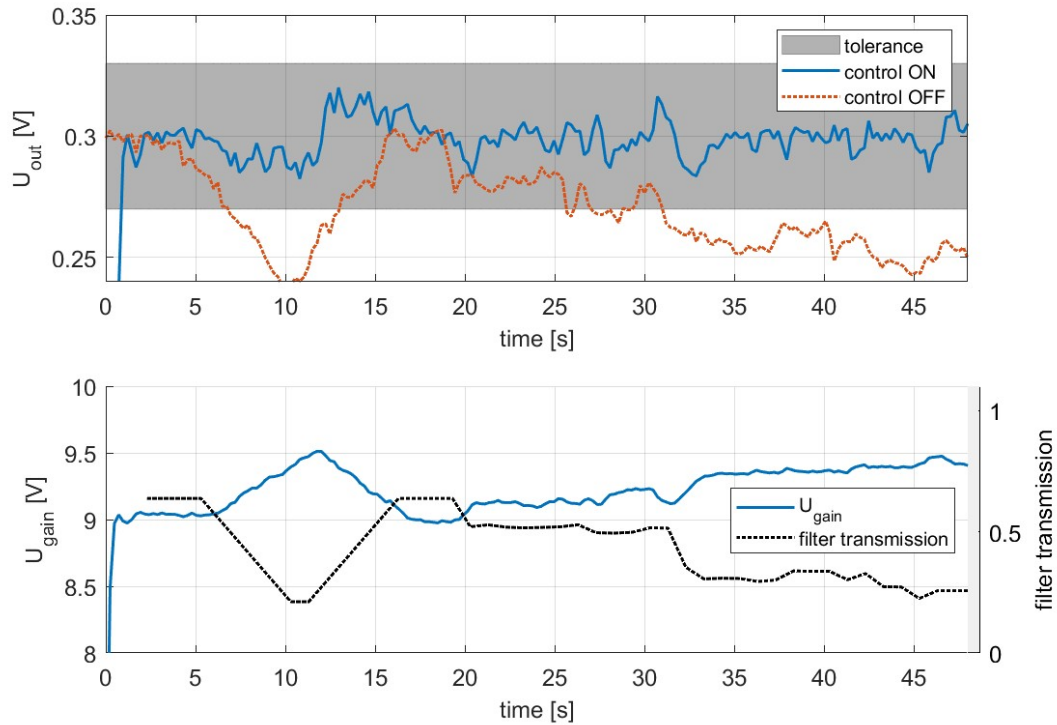


Figure 6.4: Upper plot: Measured laser intensity with the AGC disabled (dotted line), and with the AGC enabled (solid line). The grey area represents a tolerance margin of $\pm 10\%$ of the setpoint of 0.3 V. Lower plot: Filter transmission (dotted line), and control voltage U_{gain} (solid line).

Test 2 - continuously varying laser power

For the second test, the filter is continuously turned from ~ 260 deg to ~ 20 deg and then back at a period of roughly one minute. The drive of the servomotor in the set-up in Figure 4.1 can only set angles in a range of 90 degrees. As a consequence, the filter position is varied manually for this second tests. The rest of *Test 2* is carried out analogously to *Test 1*.

Figure 6.5 displays the results of *Test 2*. As the filter angle is adjusted manually, the dotted curve displayed in the lower plot of the figure must be seen as a rough approximation. This test begins with the filter at a position which causes a strong attenuation of the laser. As a result, the controller output quickly runs into saturation at 10 V. The output remains saturated until 25 seconds into the test, where the filter is at ~ 100 deg, which corresponds to a transmission of 60% according to Figure 6.3. From there on U_{out} stays within the tolerance

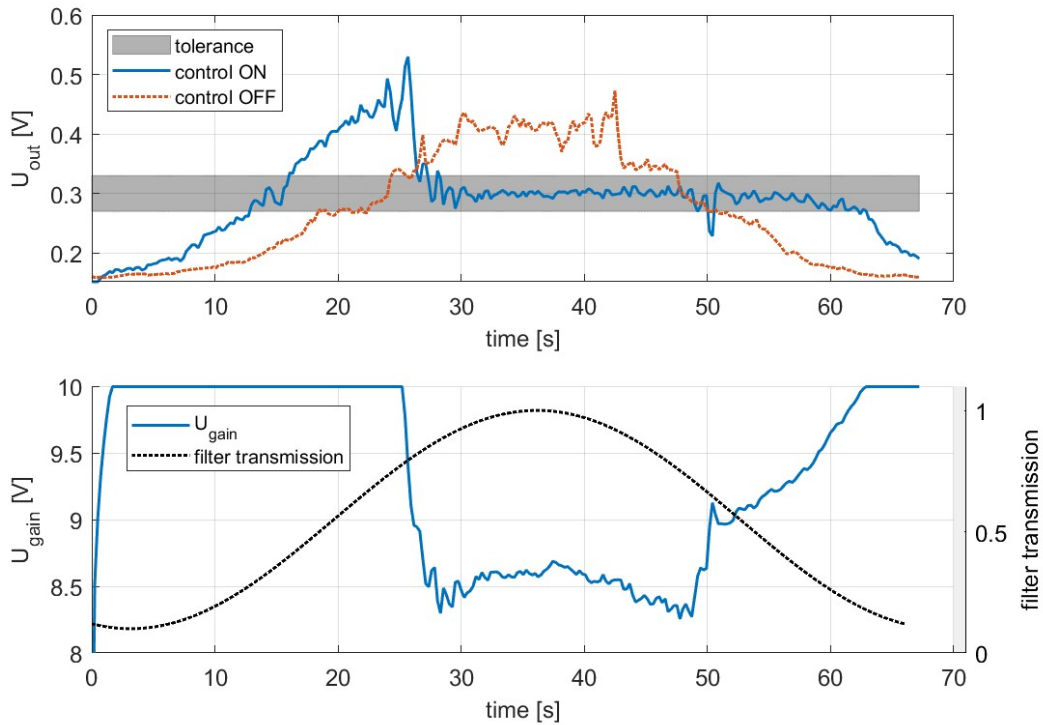


Figure 6.5: Analogous to Figure 6.4

almost continuously until $t = 63$ s, where the filter position goes back to ~ 250 deg (below 1 % transmission), and after which U_{gain} saturates again. According to this last event, the controller should have come out of saturation roughly after $t = 10$ s, where the transmission starts to increase (filter position < 250 deg). However the saturated state remains for 15 more seconds. To investigate this matter, the integrating contribution of the PI-controller is examined. Illustrated in Figure 6.6, the integrating component of the controller, which is represented by the dashed, orange line, climbs up to values of 12 volts. This is precisely what the wind-up effect is (mentioned earlier in this chapter). An anti-windup measure was implemented for the controlled variable, represented as u in pseudo-code 7 . However, no anti-windup was implemented for the integrating component of the PI-controller (int in pseudo-code 7). Since int is incremented after every loop iteration, it continues to rise, even above the saturation level of 10 V. The amount above 10 V, to which int has accumulated, must be iteratively reduced again before the overall controller output u can come back from saturation. The de-winding of int can be observed between $t = 15$ s and $t = 25$ s in Figure 6.6 and explains the overshoot of U_{gain} between $t = 15$ s and $t = 25$ s in Figure 6.5.

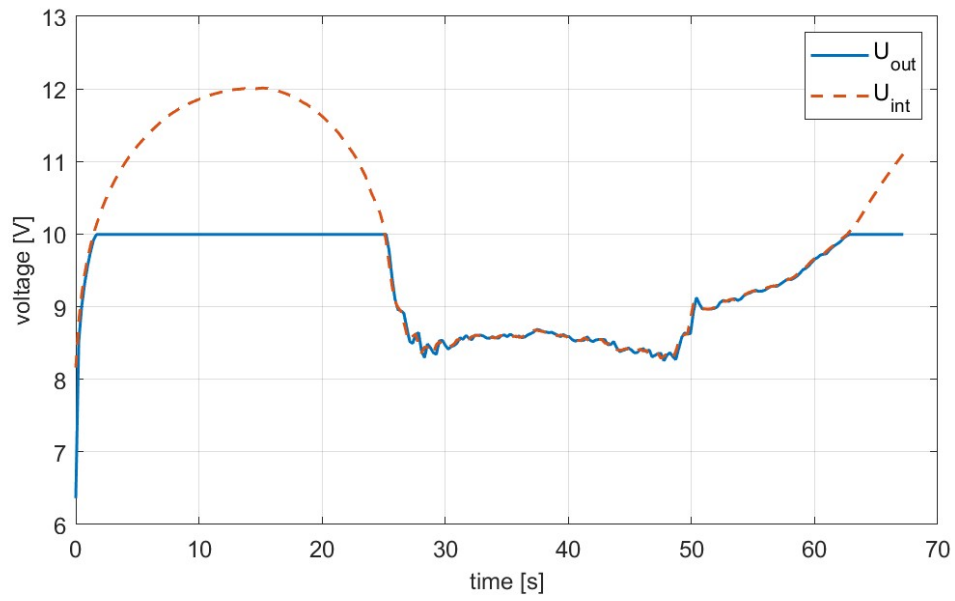


Figure 6.6: Development of U_{gain} and U_{int} throughout *Test 2*. Dashed line: integrating component. Solid line: U_{gain} .

Chapter 7

Summary

Spectral Analysis

In Chapter 3, the horizontal variability of backscattering conditions in cirrus clouds was investigated in terms of frequency composition and absolute magnitude. The spectral analysis of the WALES data demonstrated that the backscattering ratio exhibits scaling according to the Kolmogorov model of turbulence. In average a spectral slope of $k^{-1.55}$ was found which deviates from the hypothesized $k^{-5/3}$ power scaling law. For individual scenes, the slope of the spectrum can vary considerably. For example, the scene depicted in Figure 3.6 exhibits a scaling cascade falling of as $k^{-5/3}$ up to scales of 100 km. On the other hand, the scene in Figure 3.7 exhibits a shallower scaling of the spectrum with $k^{-1.58}$ and a flattening at scales above 1 km. Other scenes display spectral slopes ranging from $k^{-1.3}$ to k^{-2} . This deviations may be attributed to differences in the geometry of the individual clouds and their micro physical composition. Deviations from the Kolmogorov model have been widely documented in the literature and are the result of complex processes, not fully understood to this date. Zilberman et al. 2008 claims that the energy transfer across scales in a turbulent flow begins to deviate from the general case described by the Kolmogorov model at altitudes above 5 km. Atmospheric variables associated with turbulence, like radiative properties, may be also be affected by non-Kolmogorov turbulence.

Wispy streaks, which are common in cirrus clouds and attributed to the sedimentation of ice crystals, can be observed in many of the scenes studied in the course of this thesis. These vertically extended, elongated structures can also be identified as local extrema in the power spectra of the respective scenes (see Figure 3.7). The horizontal extent of these falling strands of ice crystals varies across a wide range of scales but is typically below a few 10s of kilometers. Occasionally, gravity waves can be observed, e.g. in Figure 7.1 with a wavelength of 50 km to 150 km, and a corresponding local maxima in the power spectrum between $k = 1/10$ km and $k = 1/30$ km. The local minimum at $k = 1/40$ km ($\lambda = 251$ km) and the subsequent flattening of the spectrum may be attributed to the zero-padding of the data. The sizes the features previously mentioned, lie beyond the scales which are relevant for aviation turbulence (50 m - 300 m). With the spatial resolution of the available data (typically 230 m), a detection of spatial features at aviation relevant scales is not possible.

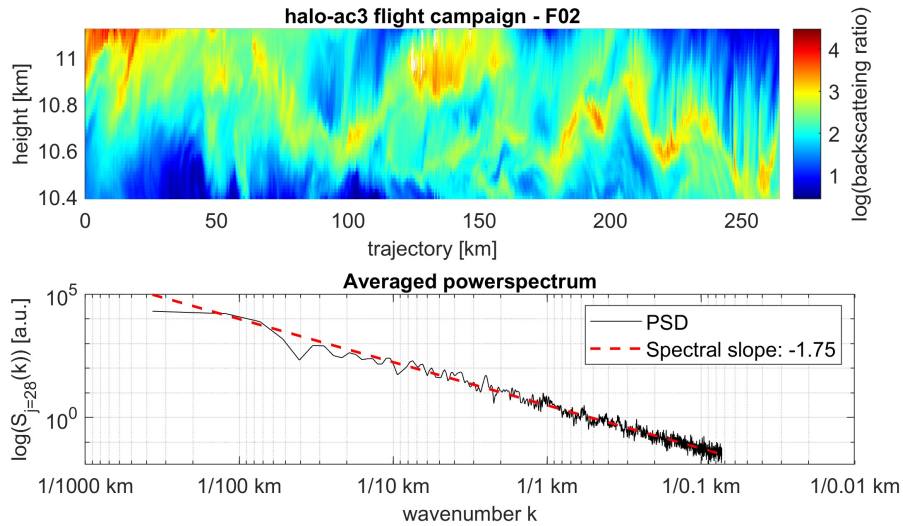


Figure 7.1: Top: slice of backscattering ratio profile. Solid, black line: corresponding power spectrum averaged over all altitude levels. Dashed, red line: corresponding spectral slope.

Magnitude of Backscattered Signal Power Variability

Nevertheless, it is possible to assess the statistics of changes in the backscattering conditions within steps of 230 meters along the horizontal dimension. With the lidar equation (Equation 2.2), instrumental parameters of the AEROLI lidar (Table 3.1) and backscattering and extinction coefficients retrieved from backscattering ratio observations, changes in the peak power of the backscattered signal were computed in the second part of Chapter 3. The statistics were computed for the absolute value of change in return signal power. The results from this investigation served the formulation of boundary conditions within which the AGC was tested, so absolute values were needed. It was estimated that, at a transmitted power of 8W, the AEROLI laser will perceive changes in the return signal power below ± 1.63 nW with a probability of $3\sigma = 99.7\%$, when flying through a cirrus cloud. This corresponds to a factor of ~ 11 when normalized with the return signal power from pure molecular backscattering at an altitude of 9 km. The estimated changes in backscattering signal power within 230 m are at least 11 times smaller than the ratio of return signal power from particulate and molecular scattering, calculated with values of α and β taken from the ESA RMA reference model (Vaughan et al. 1998, see beginning of Chapter 3). This ratio represents the typical difference in return signal power resulting from pure molecular backscattering versus backscattering due to cirrus clouds.

The objective of this thesis, is to design an automatic gain controller (AGC) capable of balancing variations in the return signal power which are expected during flight operation. Since the AEROLI lidar will not undergo flight testing during the time frame of this work, an experimental set-up was devised (Figure 4.1) to recreate the return signal power signature of a cirrus cloud. The approach was to use an adjustable neutral density filter to randomly

modulate the laser pulse power, such that it varies by less than ± 1.63 nW, thus simulating a cirrus cloud according to the findings of the investigation explained above. A proportional-integrating (PI) controller was designed, which achieved a satisfactory level of disturbance rejection and kept the detector output within $\pm 10\%$ of the specified setpoint during the whole period of a test, where the laser power was varied as aforementioned. A second test was conducted, where the laser power was continuously increased from 0 W to 6.8 nW and then decreased back to 0 W. Throughout this experiment, a flaw in the design of the controller was discovered. As demonstrated in Chapter 6, an anti-windup measure was implemented for the controlled variable u . This is when the controller output increases beyond what the hardware can supply. However, this measure was omitted for the integrating path int of the controller. As a consequence, int continued to build up, when the controller was saturated, leading to an overshoot of the detector output (depicted in Figure 6.6). With the implementation of an anti-windup for int , a better performance is expected under the conditions of this experiment.

Another limitation of the AGC is related to the response time of the detector electronics. It was found, that the high voltage supply primarily contributes to the settling time of the detector output U_{out} upon changes in the control voltage U_{gain} , which can extend up to 181 ms. The settling time defines how fast the controller can operate. With a limitation in the update rate, the AGC is inhibited from reacting to fast changes of the disturbance, i.e. the return signal power. To enable a more performant AGC, the detector electronics, mainly the HV supply, must be re-designed.

Additional improvements of the controller may be done from the side of signal processing. More sophisticated filters can be implemented to reduce the noise of the measurements. A filter may also be integrated in the controller design. The derivative path of a PID controller is sensitive to changes in the system output, which means that it is also vulnerable to noise. With a noisy system output, a PID controller can easily become unstable. This is most likely the reason for the oscillations of the detector output illustrated by the black line in Figure 6.1, which corresponds to the PID gains found with the Ziegler-Nichols tuning method. A common approach to stabilize a PID controller is to add a lowpass filter at the end of the derivative path. This controller design is named PIDF controller, where the "F" stands for derivative filter.

Characterization of the Detector Electronics

In the course of characterizing the detector chain, some investigations were done, which did not contribute to the controller design, but were important to understand the detector system as a whole. The mathematical expression in Equation 5.1 was formulated and describes the output voltage U_{out} of the detector chain as a function of the control voltage U_{gain} . Calculations with this expression deviated by a factor of 3 from measurements. The reasons for this discrepancy are not completely understood, but some possible causes may be due to the fact that the illumination function of the sensor and losses in the optics were omitted in expression 5.1. Another possible reason for the aforementioned deviation may

be associated with the large laser pulse width used in the experimental set-up in Figure 4.1. Due to capacitances in the PMTA, large pulses may cause an effect called base-line shift, where an attenuation of the output occurs depending on the pulse width. With the available equipment, it was only possible to generate pulses with a width of 2 ms. The PMTA installed in the detector assembly, however, is specialized for pulsed operation with pulse widths in the range of ns to μ s.

A better agreement of the model in Equation 5.1 and measurements may be obtained by using shorter pulses. The AEROLI laser produces pulses with an FWHM of ~ 9 ns, which is too short to resolve at a sampling rate of 31.25 GHz. The return signal is elongated due to the continuous backscattering in the atmosphere during normal operation, enabling the measurement at the given sampling rate of the ADC. The AEROLI lidar also provides a reference signal that is split off from the transmitted laser and optically delayed by a long optical fiber, see OF_R in Figure 2.9. This delay produces a pulse, long enough to be resolved by the ADC. This reference signal could have been used in the experimental set-up to provide better measurements. However due to lengthy preparation procedures and a more complex operation, it was decided to use the more user friendly laser source shown in Figure 4.1.

Outlook

The AGC presented in this work performed well under the estimated conditions of cruise flight, where only cirrus clouds are encountered. However, the conditions owed to backscattering from optically thicker clouds were not considered in the scope of this work. For the realization of a GLA system based on turbulence detection with a DWL, a nominal operation must be assured during all flight phases. Therefore, it remains open to investigate the extent to which the backscattering conditions due to optically thicker clouds impact the operation of a DWL and how the design of an AGC must be adapted to account for it.

Bibliography

- Amiridis, V. et al. (Jan. 2015). *LIVAS: a 3-D multi-wavelength aerosol/cloud climatology based on CALIPSO and EARLINET*. en. preprint. Aerosols/Remote Sensing/Troposphere/Physics (physical properties and processes). DOI: [10.5194/acpd-15-2247-2015](https://doi.org/10.5194/acpd-15-2247-2015). URL: <https://acp.copernicus.org/preprints/15/2247/2015/acpd-15-2247-2015.pdf> (visited on 12/03/2023) (cit. on p. 34).
- Bendixen, G. E., R. F. O'Connell, and C. D. Siegert (Nov. 1981). "Digital active control system for load alleviation for the Lockheed L-1011". en. In: *The Aeronautical Journal* 85.849. Publisher: Cambridge University Press, pp. 430–436. ISSN: 0001-9240, 2059-6464. DOI: [10.1017/S0001924000030244](https://doi.org/10.1017/S0001924000030244). URL: <https://www.cambridge.org/core/journals/aeronautical-journal/article/abs/digital-active-control-system-for-load-alleviation-for-the-lockheed-l1011/A6A3727E5AA7709D18D4F8CA62FE40DD> (visited on 10/27/2023) (cit. on p. 2).
- Bodhaine, Barry A. et al. (Nov. 1999). "On Rayleigh Optical Depth Calculations". en. In: *Journal of Atmospheric and Oceanic Technology* 16.11, pp. 1854–1861. ISSN: 0739-0572, 1520-0426. DOI: [10.1175/1520-0426\(1999\)016<1854:ORODC>2.0.CO;2](https://doi.org/10.1175/1520-0426(1999)016<1854:ORODC>2.0.CO;2). URL: [http://journals.ametsoc.org/doi/10.1175/1520-0426\(1999\)016%3C1854:ORODC%3E2.0.CO;2](http://journals.ametsoc.org/doi/10.1175/1520-0426(1999)016%3C1854:ORODC%3E2.0.CO;2) (visited on 11/26/2023) (cit. on pp. 7, 36).
- Caballero, Rodrigo (Nov. 2014). "Atmospheric radiation". en. In: *Physics of the Atmosphere*. IOP Publishing. DOI: [10.1088/bk978-0-7503-1052-9ch5](https://doi.org/10.1088/bk978-0-7503-1052-9ch5). URL: <https://iopscience.iop.org/book/mono/978-0-7503-1052-9/chapter/bk978-0-7503-1052-9ch5.pdf> (visited on 12/02/2023) (cit. on p. 8).
- Castellani, Beatrice et al. (July 2014). "Comparative Analysis of Monitoring Devices for Particulate Content in Exhaust Gases". en. In: *Sustainability* 6.7. Number: 7 Publisher: Multidisciplinary Digital Publishing Institute, pp. 4287–4307. ISSN: 2071-1050. DOI: [10.3390/su6074287](https://doi.org/10.3390/su6074287). URL: <https://www.mdpi.com/2071-1050/6/7/4287> (visited on 06/02/2023) (cit. on p. 8).
- CFR (2023). *14 CFR 25.303 – Factor of safety*. en. URL: <https://www.ecfr.gov/current/title-14/part-25/section-25.303> (visited on 09/21/2023) (cit. on p. 1).
- Cho, John Y. N., Reginald E. Newell, and John D. Barrick (1999). "Horizontal wavenumber spectra of winds, temperature, and trace gases during the Pacific Exploratory Missions: 2. Gravity waves, quasi-two-dimensional turbulence, and vortical modes". en. In: *Journal of Geophysical Research: Atmospheres* 104.D13. _eprint: <https://onlinelibrary.wiley.com/doi/pdf/10.1029/1999JD900068>. pp. 16297–16308. ISSN: 2156-2202. DOI: [10.1029/1999JD900068](https://doi.org/10.1029/1999JD900068). URL: <https://onlinelibrary.wiley.com/doi/abs/10.1029/1999JD900068> (visited on 11/19/2023) (cit. on p. 28).

Bibliography

- Control theory* (Oct. 2023). en. Page Version ID: 1179372111. URL: https://en.wikipedia.org/w/index.php?title=Control_theory&oldid=1179372111 (visited on 12/02/2023) (cit. on p. 23).
- Delcambre, Sharon C. et al. (July 2013). “Diagnosing Northern Hemisphere Jet Portrayal in 17 CMIP3 Global Climate Models: Twenty-First-Century Projections”. en. In: *Journal of Climate* 26.14, pp. 4930–4946. ISSN: 0894-8755, 1520-0442. DOI: [10.1175/JCLI-D-12-00359.1](https://doi.org/10.1175/JCLI-D-12-00359.1). URL: <http://journals.ametsoc.org/doi/10.1175/JCLI-D-12-00359.1> (visited on 11/20/2023) (cit. on p. 2).
- Demoz, Belay B. et al. (1998). “Wavelet analysis of dynamical processes in cirrus”. en. In: *Geophysical Research Letters* 25.9. _eprint: <https://onlinelibrary.wiley.com/doi/pdf/10.1029/97GL03226>, pp. 1347–1350. ISSN: 1944-8007. DOI: [10.1029/97GL03226](https://doi.org/10.1029/97GL03226). URL: <https://onlinelibrary.wiley.com/doi/abs/10.1029/97GL03226> (visited on 12/01/2023) (cit. on p. 28).
- DLR (2016). *Photograph of the HALO research aircraft*. URL: <https://www.halo.dlr.de/news.html> (visited on 12/02/2023) (cit. on p. 29).
- (2023a). *CIRRUS-HL – Research campaign on ice clouds in high latitudes*. en-GB. URL: <https://cirrus-hl.de/> (visited on 11/20/2023) (cit. on p. 30).
- (2023b). *Mission: CIRRUS-HL – HALO Database – The High Altitude and LOng Range Research Aircraft Database*. URL: <https://halo-db.pa.op.dlr.de/mission/125> (visited on 11/20/2023) (cit. on pp. 29, 30).
- (2023c). *Mission: HALO-AC3 – HALO Database – The High Altitude and LOng Range Research Aircraft Database*. URL: <https://halo-db.pa.op.dlr.de/mission/130> (visited on 12/02/2023) (cit. on p. 32).
- Efremenko, Dmitry and Alexander Kokhanovsky (May 2021). *Foundations of Atmospheric Remote Sensing*. en. Google-Books-ID: iT8vEAAAQBAJ. Springer Nature. ISBN: 978-3-030-66745-0 (cit. on p. 7).
- Engineering, National Academy of (Apr. 2001). *Memorial Tributes: National Academy of Engineering, Volume 9*. Washington, D.C.: National Academies Press. ISBN: 978-0-309-07411-7. DOI: [10.17226/10094](https://doi.org/10.17226/10094). URL: <http://www.nap.edu/catalog/10094> (visited on 12/02/2023) (cit. on p. 4).
- Esselborn, Michael et al. (Jan. 2008). “Airborne high spectral resolution lidar for measuring aerosol extinction and backscatter coefficients”. EN. In: *Applied Optics* 47.3. Publisher: Optica Publishing Group, pp. 346–358. ISSN: 2155-3165. DOI: [10.1364/AO.47.000346](https://doi.org/10.1364/AO.47.000346). URL: <https://opg.optica.org/ao/abstract.cfm?uri=ao-47-3-346> (visited on 07/03/2023) (cit. on pp. 19, 20, 29).
- FAA (2023). *Turbulence | Federal Aviation Administration*. URL: <https://www.faa.gov/newsroom/turbulence> (visited on 09/23/2023) (cit. on pp. 1, 2).
- Factor of safety* (2023). en. Page Version ID: 1185817948. URL: https://en.wikipedia.org/w/index.php?title=Factor_of_safety&oldid=1185817948 (visited on 12/02/2023) (cit. on p. 1).
- Fezans, Nicolas, Hans-Dieter Joos, and Christoph Deiler (Dec. 2019). “Gust load alleviation for a long-range aircraft with and without anticipation”. en. In: *CEAS Aeronautical Journal* 10.4, pp. 1033–1057. ISSN: 1869-5590. DOI: [10.1007/s13272-019-00362-9](https://doi.org/10.1007/s13272-019-00362-9). URL: <https://doi.org/10.1007/s13272-019-00362-9> (visited on 05/26/2023) (cit. on p. 3).

Bibliography

- Gimmestad, Gary G. and David W. Roberts (2023). *Lidar engineering: introduction to basic principles*. Cambridge, United Kingdom ; New York, NY, USA: Cambridge University Press. ISBN: 978-1-139-01410-6 (cit. on pp. 8, 10, 11).
- Gutleben, M. and S. Groß (2021). "Turbulence Analysis in Long-Range-Transported Saharan Dust Layers With Airborne Lidar". en. In: *Geophysical Research Letters* 48.18. _eprint: <https://onlinelibrary.wiley.com/doi/pdf/10.1029/2021GL094418>, e2021GL094418. ISSN: 1944-8007. DOI: [10.1029/2021GL094418](https://doi.org/10.1029/2021GL094418). URL: <https://onlinelibrary.wiley.com/doi/abs/10.1029/2021GL094418> (visited on 10/10/2023) (cit. on p. 28).
- Hahn, K.-U. and R. Koenig (Aug. 1992). "ATTAS flight test and simulation results of the advanced gust management system LARS". In: *Guidance, Navigation and Control Conference*. Guidance, Navigation, and Control and Co-located Conferences. American Institute of Aeronautics and Astronautics. DOI: [10.2514/6.1992-4343](https://doi.org/10.2514/6.1992-4343). URL: <https://arc.aiaa.org/doi/10.2514/6.1992-4343> (visited on 10/27/2023) (cit. on p. 3).
- Hamamatsu-Optics (2017). *Photomultiplier Tubes: Basics and Applications (Fourth Edition)*. URL: https://www.hamamatsu.com/content/dam/hamamatsu-photonics/sites/documents/99_SALES_LIBRARY/etd/PMT_handbook_v4E.pdf (cit. on pp. 21, 22, 53).
- (2023). *H7260 Datasheet(PDF) - Hamamatsu Corporation*. en. URL: <https://www.alldatasheet.com/datasheet-pdf/pdf/575342/HAMAMATSU/H7260.html> (visited on 09/14/2023) (cit. on p. 52).
- Han, Yuli et al. (Mar. 2020). "Fine gust front structure observed by coherent Doppler lidar at Lanzhou Airport (103°49′E, 36°03′N)". eng. In: *Applied Optics* 59.9, pp. 2686–2694. ISSN: 1539-4522. DOI: [10.1364/AO.384634](https://doi.org/10.1364/AO.384634) (cit. on p. 13).
- Heideman, Michael T., Don H. Johnson, and C. Sidney Burrus (1985). "Gauss and the History of the Fast Fourier Transform". In: *Archive for History of Exact Sciences* 34.3. Publisher: Springer, pp. 265–277. ISSN: 0003-9519. URL: <https://www.jstor.org/stable/41133773> (visited on 11/28/2023) (cit. on p. 29).
- Herbst, Jonas (Apr. 2019). "Development and test of a UV lidar receiver for the measurement of wind velocities aiming at the near-range characterization of wake vortices and gusts in clear air". de. Text.PhDThesis. Ludwig-Maximilians-Universität München. URL: <https://edoc.ub.uni-muenchen.de/24347/> (visited on 05/24/2023) (cit. on pp. 16, 18, 33).
- Hlavka, Dennis L. et al. (2012). "Airborne validation of cirrus cloud properties derived from CALIPSO lidar measurements: Optical properties". en. In: *Journal of Geophysical Research: Atmospheres* 117.D9. _eprint: <https://onlinelibrary.wiley.com/doi/pdf/10.1029/2011JD017053>. ISSN: 2156-2202. DOI: [10.1029/2011JD017053](https://doi.org/10.1029/2011JD017053). URL: <https://onlinelibrary.wiley.com/doi/abs/10.1029/2011JD017053> (visited on 10/31/2023) (cit. on p. 11).
- Kollath, R. (1956). "Sekundärelektronen-Emission fester Körper bei Bestrahlung mit Elektronen". de. In: *Electron-Emission Gas Discharges I / Elektronen-Emission Gasentladungen I*. Ed. by Wayne B. Nottingham et al. Encyclopedia of Physics / Handbuch der Physik. Berlin, Heidelberg: Springer, pp. 232–303. ISBN: 978-3-642-45844-6. DOI: [10.1007/978-3-642-45844-6_3](https://doi.org/10.1007/978-3-642-45844-6_3). URL: https://doi.org/10.1007/978-3-642-45844-6_3 (visited on 12/02/2023) (cit. on p. 22).
- Kolmogorov, A. N. (1991). "The Local Structure of Turbulence in Incompressible Viscous Fluid for Very Large Reynolds Numbers". en. In: *Proceedings: Mathematical and Phys-*

Bibliography

- ical Sciences* 434.1890, pp. 9–13. URL: <http://www.jstor.org/stable/51980> (cit. on p. 28).
- Küpfmüller, K (1928). “On the Dynamics of Automatic Gain Controllers”. en. In: (cit. on p. 4). Leipzig, University of (2023). *Campaign – HALO AC3*. de-DE. URL: <https://halo-ac3.de/halo-ac3/campaign/> (visited on 11/20/2023) (cit. on p. 31).
- Linsmayer, Philippe (July 2023). *Internal communication* (cit. on pp. 17, 18).
- Linsmayer, Philippe and Patrick Vrancken (2023). *Private communication*. (Cit. on pp. 17, 52, 53).
- MathWorks-Inc. (2023a). *MATLAB Control System Toolbox* (cit. on p. 56).
- (2023b). *MATLAB Optimization Toolbox* (cit. on p. 54).
- (2023c). *MATLAB System Identification Toolbox* (cit. on p. 56).
- Mie scattering* (Nov. 2023). en. Page Version ID: 1184569870. URL: https://en.wikipedia.org/w/index.php?title=Mie_scattering&oldid=1184569870 (visited on 12/01/2023) (cit. on p. 9).
- Nastrom, G. D. and K. S. Gage (May 1985). “A Climatology of Atmospheric Wavenumber Spectra of Wind and Temperature Observed by Commercial Aircraft”. EN. In: *Journal of the Atmospheric Sciences* 42.9. Publisher: American Meteorological Society Section: Journal of the Atmospheric Sciences, pp. 950–960. ISSN: 0022-4928, 1520-0469. DOI: 10.1175/1520-0469(1985)042<0950:AC0AWS>2.0.CO;2. URL: https://journals.ametsoc.org/view/journals/atasc/42/9/1520-0469_1985_042_0950_acoaws_2_0_co_2.xml (visited on 10/03/2023) (cit. on p. 28).
- National-Instruments (2023). *National Instruments USB-6001*. de. URL: <https://www.ni.com/de-de/shop/model/usb-6001.html> (visited on 11/14/2023) (cit. on p. 50).
- Photoelectric effect* (Nov. 2023). en. Page Version ID: 1186362456. URL: https://en.wikipedia.org/w/index.php?title=Photoelectric_effect&oldid=1186362456 (visited on 11/23/2023) (cit. on p. 21).
- Pockels, F. (1906). *Lehrbuch der kristallographie*. eng. Leipzig Und Berlin Druck Und Verlag Von B.G. Teubner. URL: <http://archive.org/details/lehrbuchderkrist0000drfp> (visited on 11/16/2023) (cit. on p. 48).
- Pressel, Kyle G. and William D. Collins (Aug. 2012). “First-Order Structure Function Analysis of Statistical Scale Invariance in the AIRS-Observed Water Vapor Field”. EN. In: *Journal of Climate* 25.16. Publisher: American Meteorological Society Section: Journal of Climate, pp. 5538–5555. ISSN: 0894-8755, 1520-0442. DOI: 10.1175/JCLI-D-11-00374.1. URL: <https://journals.ametsoc.org/view/journals/clim/25/16/jcli-d-11-00374.1.xml> (visited on 10/03/2023) (cit. on p. 28).
- Puempel, Herbert and Paul D Williams (2019). “THE IMPACTS OF CLIMATE CHANGE ON AVIATION: SCIENTIFIC CHALLENGES AND ADAPTATION PATHWAYS”. en. In: (cit. on p. 2).
- Robinson, Paul A. (May 1996). “Use of predictive lidar measurements in alleviating turbulence-induced disturbances of aircraft in flight”. In: ed. by Robert G. Otto, James Lenz, and Russell Targ. Orlando, FL, pp. 86–97. DOI: 10.1117/12.241056. URL: <http://proceedings.spiedigitallibrary.org/proceeding.aspx?articleid=1018342> (visited on 10/05/2023) (cit. on p. 3).

Bibliography

- Schäfler, Andreas et al. (June 2020). "Observation of Jet Stream Winds during NAWDEX and Characterization of Systematic Meteorological Analysis Errors". EN. In: *Monthly Weather Review* 148.7. Publisher: American Meteorological Society Section: Monthly Weather Review, pp. 2889–2907. ISSN: 1520-0493, 0027-0644. DOI: [10.1175/MWR-D-19-0229.1](https://doi.org/10.1175/MWR-D-19-0229.1). URL: <https://journals.ametsoc.org/view/journals/mwre/148/7/mwrD190229.xml> (visited on 11/28/2023) (cit. on p. 35).
- Sharman, Robert and Todd Lane, eds. (2016). *Aviation Turbulence*. en. Cham: Springer International Publishing. ISBN: 978-3-319-23629-2 978-3-319-23630-8. DOI: [10.1007/978-3-319-23630-8](https://doi.org/10.1007/978-3-319-23630-8). URL: <http://link.springer.com/10.1007/978-3-319-23630-8> (visited on 09/21/2023) (cit. on pp. 1, 27, 28).
- Society, European Meteorological (2023). *Meteorological Archival and Retrieval System*. URL: <https://www.emetsoc.org/awards/award/meteorological-archival-and-retrieval-system/> (visited on 12/13/2023) (cit. on p. 35).
- Spectrum-Instrumentation (2023). *M2i.4932 16 bit multi-purpose digitizer - SPECTRUM Instrumentation*. URL: <https://spectrum-instrumentation.com/products/details/M2i4932.php> (visited on 11/14/2023) (cit. on p. 49).
- Texas-Instruments (Sept. 2004). *Quad, Unity-Gain STable, Low-Noise, Voltage-Feedback Operational Amplifier*. URL: <https://www.ti.com/product/OPA4820> (cit. on p. 52).
- Turbulence* (Nov. 2023). en. Page Version ID: 1186025120. URL: <https://en.wikipedia.org/w/index.php?title=Turbulence&oldid=1186025120> (visited on 11/24/2023) (cit. on p. 27).
- Tvryanans, Anthony P. (Sept. 2003). "Epidemiology of turbulence-related injuries in airline cabin crew, 1992-2001". eng. In: *Aviation, Space, and Environmental Medicine* 74.9, pp. 970–976. ISSN: 0095-6562 (cit. on p. 1).
- Vaughan, J. M. et al. (1998). "Establishment of a backscatter coefficient and atmospheric database. ESA-CR12510 22". In: (cit. on pp. 11, 34, 70).
- Vrancken, Patrick (2016). "Airborne Remote Detection of Turbulence with Forward-Pointing LIDAR". en. In: *Aviation Turbulence: Processes, Detection, Prediction*. Ed. by Robert Sharman and Todd Lane. Cham: Springer International Publishing, pp. 443–464. ISBN: 978-3-319-23630-8. DOI: [10.1007/978-3-319-23630-8_22](https://doi.org/10.1007/978-3-319-23630-8_22). URL: https://doi.org/10.1007/978-3-319-23630-8_22 (visited on 11/13/2023) (cit. on p. 14).
- Vrancken, Patrick and Jonas Herbst (2019). "Development and Test of a Fringe-Imaging Direct-Detection Doppler Wind Lidar for Aeronautics". en. In: *EPJ Web of Conferences*. Hefei, Volksrepublik China, pp. 1–4. DOI: [10.1051/epjconf/202023707008](https://doi.org/10.1051/epjconf/202023707008). URL: <https://elib.dlr.de/123605/> (visited on 11/10/2023) (cit. on p. 13).
- (Jan. 2022). "Aeronautics Application of Direct-Detection Doppler Wind Lidar: An Adapted Design Based on a Fringe-Imaging Michelson Interferometer as Spectral Analyzer". en. In: *Remote Sensing* 14.14. Number: 14 Publisher: Multidisciplinary Digital Publishing Institute, p. 3356. ISSN: 2072-4292. DOI: [10.3390/rs14143356](https://doi.org/10.3390/rs14143356). URL: <https://www.mdpi.com/2072-4292/14/14/3356> (visited on 04/25/2023) (cit. on pp. 3, 5, 17, 33, 52).
- Vrancken, Patrick, Wirth, et al. (Nov. 2016). "Airborne forward pointing UV Rayleigh lidar for remote clear air turbulence (CAT) detection: system design and performance". In: *Applied Optics* 55.32. arXiv:1606.09533 [physics], p. 9314. ISSN: 0003-6935, 1539-4522.

Bibliography

- DOI: [10.1364/AO.55.009314](https://doi.org/10.1364/AO.55.009314). URL: <http://arxiv.org/abs/1606.09533> (visited on 06/01/2023) (cit. on p. 16).
- Wang, Likun and Kenneth Sassen (Feb. 2006). "Cirrus Mammatus Properties Derived from an Extended Remote Sensing Dataset". EN. In: *Journal of the Atmospheric Sciences* 63.2. Publisher: American Meteorological Society Section: Journal of the Atmospheric Sciences, pp. 712–725. ISSN: 0022-4928, 1520-0469. DOI: [10.1175/JAS3648.1](https://doi.org/10.1175/JAS3648.1). URL: <https://journals.ametsoc.org/view/journals/atsc/63/2/jas3648.1.xml> (visited on 12/01/2023) (cit. on p. 28).
- Wave Interference and Beat Frequency* (2023). en. URL: <https://academo.org/demos/wave-interference-beat-frequency/> (visited on 11/13/2023) (cit. on p. 15).
- Williams, Paul D. (May 2017). "Increased light, moderate, and severe clear-air turbulence in response to climate change". en. In: *Advances in Atmospheric Sciences* 34.5, pp. 576–586. ISSN: 1861-9533. DOI: [10.1007/s00376-017-6268-2](https://doi.org/10.1007/s00376-017-6268-2). URL: <https://doi.org/10.1007/s00376-017-6268-2> (visited on 10/26/2023) (cit. on p. 2).
- Williams, Paul D. and Luke N. Storer (2022). "Can a climate model successfully diagnose clear-air turbulence and its response to climate change?" en. In: *Quarterly Journal of the Royal Meteorological Society* 148.744. _eprint: <https://onlinelibrary.wiley.com/doi/pdf/10.1002/qj.4270>, pp. 1424–1438. ISSN: 1477-870X. DOI: [10.1002/qj.4270](https://doi.org/10.1002/qj.4270). URL: <https://onlinelibrary.wiley.com/doi/abs/10.1002/qj.4270> (visited on 10/26/2023) (cit. on p. 2).
- Wirth, M. et al. (July 2009). "The airborne multi-wavelength water vapor differential absorption lidar WALES: system design and performance". en. In: *Applied Physics B* 96.1, pp. 201–213. ISSN: 1432-0649. DOI: [10.1007/s00340-009-3365-7](https://doi.org/10.1007/s00340-009-3365-7). URL: <https://doi.org/10.1007/s00340-009-3365-7> (visited on 07/03/2023) (cit. on p. 29).
- Ziegler–Nichols method* (Feb. 2023). en. Page Version ID: 1140258750. URL: https://en.wikipedia.org/w/index.php?title=Ziegler%E2%80%93Nichols_method&oldid=1140258750 (visited on 12/13/2023) (cit. on p. 27).
- Zilberman, Arkadi et al. (Apr. 2008). "Lidar study of aerosol turbulence characteristics in the troposphere: Kolmogorov and non-Kolmogorov turbulence". In: *Atmospheric Research* 88.1, pp. 66–77. ISSN: 0169-8095. DOI: [10.1016/j.atmosres.2007.10.003](https://doi.org/10.1016/j.atmosres.2007.10.003). URL: <https://www.sciencedirect.com/science/article/pii/S016980950700172X> (visited on 10/27/2023) (cit. on pp. 28, 69).

Acknowledgements

I want to thank my colleagues from DLR's institute of atmospheric physics for their help and support.

Appendix

Pseudo Code

Computation of the Power Spectrum

```
1 lenTarget = 5000; % target length of trajectory dimension
2 Fs = 1; % temporal sampling frequency of data in Hz
3 for iSection = nSections
4     % non uniform spatially sampled data
5     data = BSR(iSection,:,:);
6
7     % zero padding
8     dataPad = zeropad(data,lenTarget);
9
10    % definition of the frequency vector
11    f = linspace(-Fs/2,Fs/2,lenTarget);
12
13    sumPSD = zeros(1,length(f));
14    for iAlt = 1:nAlt
15        X = dataPad(iAlt,:) % horizontal BSR slice
16        if NaN in X
17            continue % skip this horizontal BSR slice
18        end
19
20        % fourier transform of X with zero-frequency component shifted to the
21        % center of the spectrum
22        xFFT = fftshift(fft(X));
23        xPSD = abs(xFFT)/(lenTarget/Fs); % power spectrum of X
24        sumPSD = sumPSD + xPSD;
25    end
26
27    % average power spectrum of BSR section
28    avgPSD = sumPSD/lenTarget;
29
30    k = 2*pi*f/(dTarget*Fs);
end
```

Computation of the Probability Density

```

1 % load overlap function and corresponding range vector from data
2 GTemp = load(overlap);
3 RTemp = load(range);
4
5 % interpolate overlap function to target range vector
6 R = 18:dR:1000; % target range vector [m]
7 G = interp1(Rtemp,Gtemp,R);
8 windowLen = length(R);
9
10 PFlat = []; % flattened difference vector
11 for nDiff = [1,2,3,4,5]
12     for iScene = 1:nScenes
13         beta = betaAll(iScene);
14         alpha = alphaAll(iScene);
15         for iAlt = 1:nAlt
16             if NaN in beta(iAlt)
17                 continue % skip this horizontal alpha and beta slice
18             end
19
20             for iWin = 1:shape(2)-windowLen
21                 % get window of
22                 betaWin = beta(iAlt,iWin:iWin+windowLen-1);
23                 alphaWin = alpha(iAlt,iWin:iWin+windowLen-1);
24
25                 % compute optical depth T
26                 T = 0;
27                 for iR = 1:length(R)
28                     T = T + alphaWin(iR)*dR;
29                 end
30                 P_return = P0*dR*A*eta*0./R.^2.*betaWin.*exp(-2*T); % Lidar
31                 equation
32                 [M,I] = max(P_return);
33                 PMax(iAlt,iWin) = M;
34             end
35         end
36         PDiff = diff(PMax,nDiff,2); % compute difference of shifted Pmax
37         PDiff = reshape(PDiff,[],1); % flatten array
38         PFlat(end+1:(end+length(PDiff))) = PDiff; % Append all data Scenes
39     end
40 end

```

Implementation of the Automatic Gain Controller

```

1 dt = 240 % [ms]
2 iCounter = 0;
3 while true

```

```
4   if iCounter == 0 % initialization
5       int = 0;
6       ePrior = r-y;
7   else
8       e = r-y; %output error
9       prop = Kp*e; % proportional path
10      int = int+Ki*dt*e; % integrating path
11      der = Kd*(e-ePrior)/dt; % derivative path
12      u = prop+int+der;
13
14      % define limits for u to avoid wind-up
15      if u > uMax
16          u = uMax;
17      elseif u < uMin
18          u = uMin;
19      end
20      ePrior = e;
21      % conversion of u: current amplification factor to uGain: control
22      % voltage
23      uGain = 2.096*u^(1/9.285);
24      output(uGain);
25  end
26  iCounter = iCounter + 1;
end
```

Flow Diagrams

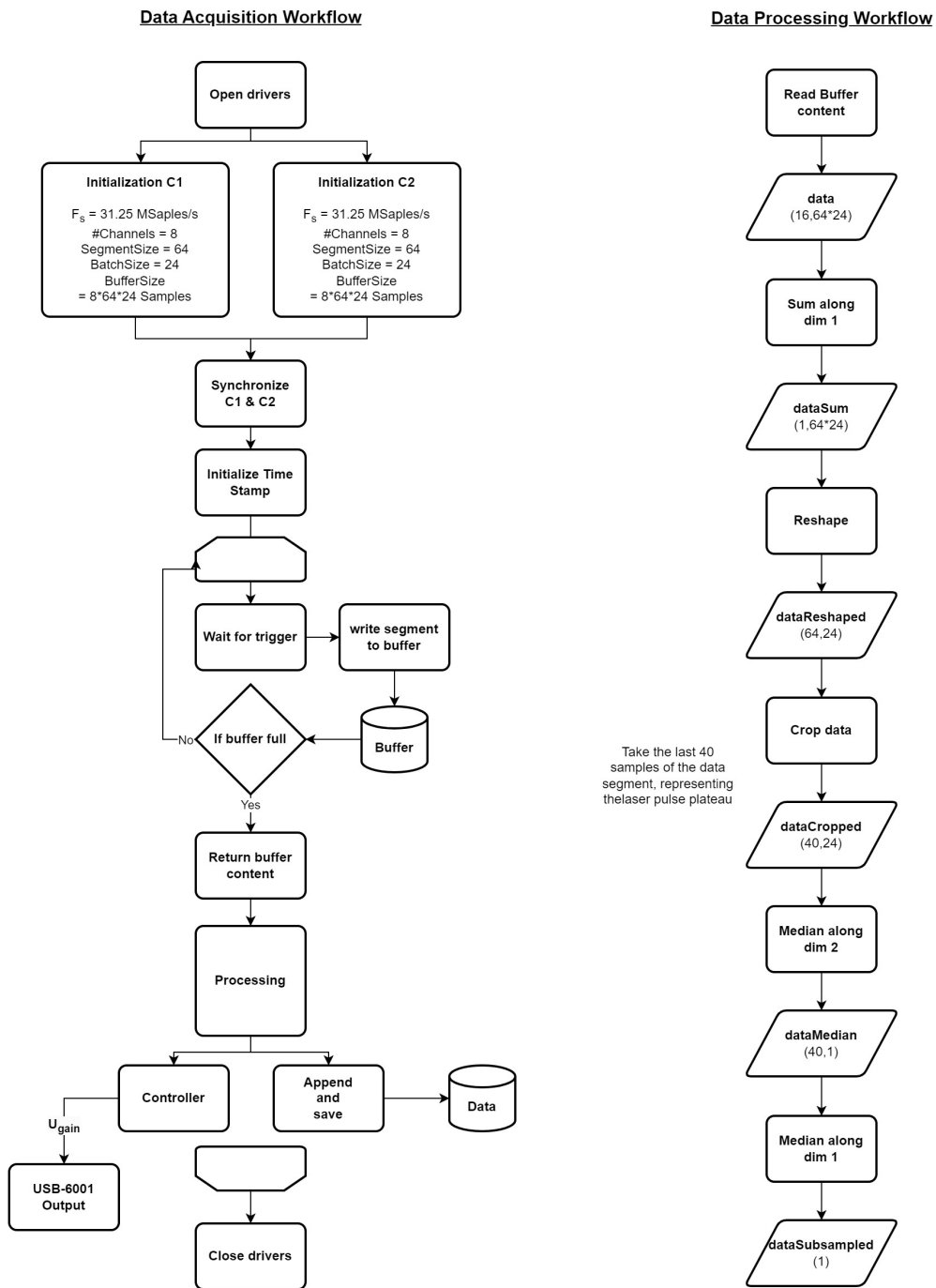


Figure 7.2: Data acquisition and processing workflow.

Tables

Scene	$\min(v_j)$	$\max(v_j)$	\bar{v}_j	$\sigma(v_j)$	$\frac{\max(v_j) - \min(v_j)}{\bar{v}_j}$	$\frac{\sigma(v_j)}{\bar{v}_j}$
1	215.94	234.69	231.26	4.07	0.0811	0.0176
2	212.34	237.59	229.50	7.73	0.1100	0.0337
3	206.93	223.20	214.97	4.53	0.0757	0.0211
4	216.30	219.43	218.03	0.77	0.0144	0.0035
5	212.46	217.45	214.73	1.37	0.0233	0.0064
6	237.58	242.81	240.55	1.34	0.0217	0.0056
7	233.13	242.64	238.35	1.59	0.0399	0.0067
8	219.75	229.22	225.90	2.37	0.0419	0.0105
9	208.10	212.77	210.99	1.07	0.0221	0.0051
10	223.41	227.63	225.45	1.11	0.0187	0.0049
11	234.50	241.30	237.70	1.66	0.0286	0.0070
12	233.32	242.61	237.50	3.04	0.0391	0.0128
13	229.80	231.59	230.92	0.35	0.0077	0.0015
14	231.16	243.53	237.69	3.91	0.0521	0.0164
15	228.46	236.69	232.96	2.26	0.0353	0.0097
16	223.51	226.16	224.48	0.76	0.0118	0.0034
17	253.53	259.82	257.33	1.77	0.0244	0.0069
18	221.26	239.96	233.36	4.08	0.0801	0.0175
19	237.01	239.23	238.29	0.46	0.0093	0.0019
20	236.49	243.44	238.72	1.41	0.0291	0.0059
21	219.04	225.23	222.80	1.61	0.0278	0.0072
22	222.36	227.01	224.95	1.11	0.0207	0.0050
23	229.56	238.82	232.96	1.89	0.0397	0.0081
24	214.00	223.14	217.88	2.57	0.0420	0.0118
25	239.26	247.26	242.08	1.92	0.0330	0.0079
26	202.44	208.50	205.17	1.44	0.0295	0.0070
27	246.16	252.23	249.84	1.20	0.0243	0.0048
28	191.80	200.63	196.62	2.25	0.0449	0.0114
29	245.52	256.69	248.63	2.58	0.0449	0.0104
30	231.24	240.23	236.07	2.19	0.0381	0.0093
31	237.04	241.64	239.71	1.12	0.0192	0.0047
32	210.27	236.47	233.40	1.60	0.1123	0.0069
33	224.11	273.41	240.65	2.97	0.2048	0.0123
34	208.95	246.27	228.00	2.54	0.1637	0.0111
35	229.30	238.55	233.46	2.48	0.0397	0.0106
36	232.14	242.03	237.19	2.22	0.0417	0.0094
37	234.70	240.22	237.09	1.20	0.0233	0.0050
38	219.56	224.79	221.90	1.23	0.0236	0.0055
39	235.09	247.27	240.97	3.56	0.0505	0.0148

40	240.99	252.59	246.54	2.49	0.0471	0.0101
41	217.73	228.47	221.83	2.00	0.0484	0.0090
42	218.23	228.07	224.58	2.32	0.0438	0.0103
43	216.83	222.05	219.48	1.50	0.0238	0.0069
44	217.33	221.73	219.60	0.94	0.0201	0.0043
45	220.89	232.38	225.84	2.44	0.0509	0.0108
46	247.55	251.81	250.05	0.91	0.0170	0.0036
47	222.31	231.13	226.10	2.55	0.0390	0.0113
48	219.19	231.97	224.85	2.29	0.0568	0.0102
49	214.38	219.19	217.22	1.32	0.0221	0.0061
50	247.23	252.00	249.97	1.28	0.0191	0.0051
51	247.10	254.78	250.50	2.12	0.0307	0.0084
52	227.33	233.75	230.61	1.81	0.0278	0.0079
53	246.47	260.66	254.56	3.01	0.0558	0.0118
54	219.77	225.91	222.93	1.23	0.0276	0.0055
55	219.31	225.89	222.69	1.79	0.0295	0.0080
56	256.23	265.74	261.08	2.05	0.0364	0.0079
57	218.98	227.11	223.16	1.91	0.0364	0.0086
58	257.53	269.20	262.67	2.34	0.0444	0.0089
59	219.09	221.73	220.32	0.68	0.0120	0.0031
60	209.69	216.60	211.71	1.26	0.0327	0.0060
61	209.92	215.31	212.75	1.13	0.0253	0.0053
62	198.88	204.04	201.63	1.32	0.0256	0.0065
63	195.13	201.81	197.94	1.26	0.0337	0.0064
64	237.58	252.84	246.03	3.87	0.0621	0.0157
65	197.39	203.00	199.71	1.46	0.0281	0.0073
66	193.94	199.54	196.80	1.16	0.0285	0.0059
67	236.64	246.77	242.10	2.09	0.0418	0.0086
68	244.11	254.56	248.90	1.97	0.0420	0.0079

$\min(v)$	$\max(v)$	\bar{v}	$\bar{\sigma}(v_j)$	$\frac{\max(v)-\min(v)}{\bar{v}}$	$\frac{\bar{\sigma}(v_j)}{\bar{v}}$
191.80	273.41	230.00	2.00	0.2048	0.0087
$\min(\bar{v}_j)$	$\max(\bar{v}_j)$	\bar{v}	$\sigma(\bar{v}_j)$	$\frac{\max(\bar{v}_j)-\min(\bar{v}_j)}{\bar{v}}$	$\frac{\sigma(\bar{v}_j)}{\bar{v}}$
196.62	262.67	230.00	15.39	0.2872	0.0669

Table 7.2: Statistics of flight velocities of the HALO aircraft for the scenes j .